Università degli Studi di Salerno

Department of Chemistry and Biology "Adolfo Zambelli"

PhD in Chemistry – XXXIII Course
Dottorati innovativi con caratterizzazione industriale PON "Ricerca e Innovazione" 2014- 2020 PhD

Thesis on

Combined adsorption and solar driven photocatalysis processes for the removal of persistent contaminants from water by highly porous nanocomposite aerogels

Academic tutor:
Dr. Maurizio Carotenuto

Ph.D. Student:
Wanda Navarra

Serial number:
8800100044

Ph.D.coordinator:
Prof. Claudio Pellecchia

Academic year 2020/2021

Index

List of abbreviations

AA-EQS: the average annual value

AOPs: advanced oxidation processes

ATZ: atrazine

BET: Brunauer–Emmett–Teller

CB: conduction band

CECs: contaminants of emerging concern

DEA: deethylatrazine

DIA: deisopropylatrazine

EBT: eriochrome black T-dye

EQS: nvironmental Quality Standards

EU: European community

HA: hydroxy atrazine

HP-A: highly porous aerogels

HP-NcA: highly porous nanocomposite aerogel

HP-NcAs: highly porous nanocomposite aerogels

MAC-EQS: maximum allowable concentration

MB: methylene blue

NdT: N-doped TiO_2

OH•: hydroxyl radicals

THI: thiacloprid

TNT: non-woven material

TTIP: titanium tetraisopropoxide

PCE: tetrachloroethylene

PP: polypropylene

PSs: priority substances

PVA: polyvinyl alcohol

PANI: polyaniline

PVP: polyvinylpyrrolidone

sPS: syndyotactic polystyrene

S-A: semiconductor A

S-B: semiconductor B

S-CNT: semiconductor-carbon nanotube

S-M: semiconductor-metal

S-M-S: multicomponent heterojunctions

S-S: semiconductor-semiconductor

SSA: specific surface area

TiO_2: titanium dioxide

UV: ultraviolet light

UV-A: ultraviolet light at 365 nm

VB: valence band

Vis or VIS: visible light

VOCs: volatile organic compounds

WAXD: wide angle X-ray diffraction

WFD: water frame directive

WWTPs: wastewater treatment plants

XRD: X-ray diffraction patterns

Abstract

Water is a very important resource for human and ecosystem. However, in recent years the presence of pollutants, such as pharmaceuticals, cosmetics, personal cares, dyes, and pesticides deriving from industrial, agricultural, and human practices is object of growing concern as these substances persist in the environment and are not removed by wastewater treatment plants (WWTPs). In fact, the latter are among the main sources of such pollution since they are not designed to remove persistent organic contaminants that are eventually discharged into receiving water bodies.

Thus, many substances, their metabolites and/or transformation products once in the environment, can propagate through different environmental compartments or can accumulate in plants and others organism posing a risk to the environment and human health, as the ecotoxicological effects of the presence of these molecules in the environment are often unknown.

Advanced oxidation processed (AOPs) are the most promising techniques that could solve this problem. In fact, during AOPs processes are generate hydroxyl radicals (OH•) highly reactive and capable of oxidising these contaminants. Among all these processes, heterogeneous photocatalysis has been widely investigated for this purpose due to its ability to mineralize many organic compounds using the solar light as light source.

The photocatalysts is generally dispersed in a slurry reactor as suspended powder resulting in disadvantages, such as the necessity to separate

particles from the treated water, the damage of the recirculation pumps used for the process and toxicity problems related either to the release of the metal in solution or to the generation of by-products or intermediates that are more toxic than the starting materials.

So, a possible solution could be to fix the photocatalyst into highly porous nanocomposite aerogels (HP-NcAs) developing a sustainable and low environmental impact technology for the degradation of organic pollutants using UV, VIS and solar light. The HP-NcAs are easy-to-handle, highly efficient composite materials to be used as an alternative to conventional catalysts in solar driven-photocatalysis with the benefit of maximising the specific photo-activatable surface area compared with other media (ceramics, films and sponge) and preventing the nanoparticles aggregation in aqueous matrix. Therefore, in this work, aerogel/photocatalyst composite systems based on syndiotactic polystyrene (sPS) and semiconductors such as N-TiO_2 (NdT), ZnO, ZnO/NdT and Fe^0-ZnS were prepared and tested in the degradation processes of model pollutants, such as atrazine (ATZ), thiacloprid (THI) and tetrachloroethylene (PCE) under UV, Visible and solar irradiation. In addition, ecotoxicological experiments were carried out to evaluate the adverse toxicity effects of materials and solutions generated by the degradation process.

Introduction

Water is a very important resource for both humans and ecosystems. The continuous water demand for domestic, agricultural, and industrial uses as a result of demographic growth, intensive urbanization, and expansion of human activities could lead, in the next decades, to the worsening of the water crisis already existing in some regions of the planet [1–3]. The problem, associated with uneven distribution of the water resources and climate change, will be more felt in those countries with a rapid economic developing such as Brazil, Russia, India, China, and South Africa (usually named as BRICS).

According to United Nations reports, about 1.2 billion people live in areas susceptible to water scarcity and 1.8 billion people will face the same problem starting from 2025 [4]. Wastewater reuse, in particular for irrigation or industrial purposes, could be a good choice to face the problem with lower environmental impact and costs than other sources of water supply such as water transfer and desalination [5,6]. In fact, the European Parliament's Regulation 2020/741 has recently established minimum requirements for water quality to ensure that it is safe when used for agricultural irrigation, prescribing a high protection of the environment, human and animal health [7]. Besides, this practice can also promote the circular economy by recovering nutrients, such as nitrogen, phosphorus, and potassium, from the reclaimed water and applying them

to crops, by means of fertigation techniques, reducing the need for supplemental applications of mineral fertiliser.

Although wastewater reuse could solve the problem of water scarcity, it can generate public health problems when the treatments are not adequate. The global socioeconomic development generates many substances which can be released into the environment threating the human health and environment. It has been estimated that the chemical industry currently produces more than 70000 different chemical products every year and only the micro-pollutants, such as pharmaceuticals, cosmetics, personal cares, dyes, and pesticides, amounts to approximately 500 million tons/year [8].

In the last decade, wastewater treatment plants (WWTPs) have been identified as a major point source of this kind of pollution [9] because they are not designed to remove bio-recalcitrant contaminants and micropollutants making urban WWTs an hot spots of contamination. Thus, many compounds, their metabolites and/or transformation products are detected in surface waters posing a serious risk for both environment and human health [10].

Once into the environment, they can propagate through different environmental compartments or can accumulate in plants and others organism [11], according to: a) the properties of the molecules (chemical structure, acidity constant, octanol-water partition coefficient, etc.) and b)

the characteristics of the surrounding environment, that govern some different processes such as sorption, volatilization, dispersion, oxidation, isomerisation, photodegradation and biodegradation [12].

The ecotoxicological adverse effects related to the release of such substances are another aspect to be considered. The knowledge of their impact on the environment and the long-term effects of exposure to a mixture of pollutants are often unknown (HELCOM 2003).

Thus, to minimize the discharge of micro-pollutants into receiving water bodies and improve the applicability and efficiency of the conventional wastewater treatments, new technologies have been developed.

Among them, Advanced Oxidation Processes (AOPs), based on the formation of a powerful oxidizing agent, such as hydroxyl radicals ($OH^{\bullet}$), are taking hold, as they are very efficient in the degradation and sometimes mineralization a large amount of bio-recalcitrant contaminants [13–15].

Heterogeneous photocatalysis using semiconductors in powder form is the most widely studied. However, the use of powder photocatalysts suffer of some drawbacks such as expensive post-treatment filtration processes for the recovery, aggregation of photocatalytic particles especially at higher concentrations and ecotoxicological adverse effects related to photocatalyst release into the water. To overcome these problems, the photocatalysts could be fixed in different materials such as glass, activated

carbon, clay, ceramics and different kind of polymers. Highly porous aerogels (HP-A) could be a valid alternative to these matrices thanks to their high stability, high specific surface area, open pores with high interconnectivity for mass transport, appropriate surfaces for photocatalyst anchorage and high manageability and modelling.

Dispersion of photocatalytic nanoparticles inside the HP-A has the advantage of preserving the initial particle size (no aggregation of the nanoparticles), thus maximising the specific photo-activatable surface area, where the production of the radicals takes place, favouring the kinetics removal of the contaminants. The use of highly porous nanocomposite aerogels (HP-NcA) in photocatalytic processes could be able to avoid expansive cost of separation processes, reducing the risks of contamination. The homogeneous dispersion of the photocatalysts in the entire three-dimensional structure of the aerogels can magnify the contact area among nanoparticles and media.

The goal of this PhD thesis is to develop a sustainable technology for the treatment of water and wastewaters, based on highly porous aerogels (syndiotactic polystyrene, sPS) filled with different photocatalysts (N-doped TiO_2, ZnO/N-doped TiO_2 and Fe^0/ZnS) employed in processes driven by UV, Vis and solar light. The non-ionic organic compounds atrazine (ATZ), thiacloprid (THI) and tetrachloroethylene (PCE) were chosen as contaminant target to test these composite materials. They are

suitable candidates being easily adsorbed into the apolar sPS matrix and with a compatible size to enter in the nanoporous cavities of sPS crystalline phase.

The research activity, outlined in Figure 1, started with the preparation of photocatalysts (suitably designed to work under UV, Vis and solar irradiation): The optimized photocatalysts were dispersed within sPS-based polymer aerogels to produce HP-NcAs, which are tested in photocatalytic experiments using different light sources. Moreover, the ecotoxicological compatibility of the catalytic materials and solutions resulting from the photocatalytic processes were assessed with the aim of testing the best materials in a suitably designed pilot-scale reactor.

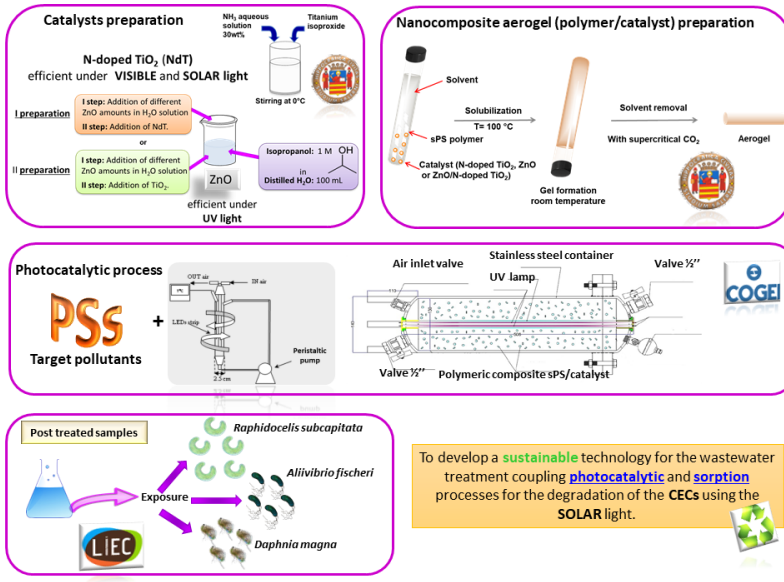

Figure 1. Schematic overview of the experimental activity.

1 Issue

1.1 Priority substances and compounds of emerging concern in EU legislation

Nowadays, a huge number of organic compounds, metal, and metal organic compounds are used in different activities, from medicine to chemical industry, from agriculture to human practices. At the end of their life, they arrive into the environment by urban and agricultural run-off, industrial and domestic wastewater treatment plant effluents [16,17], where they are often found in the aquatic environment such as rivers, lake, oceans and also drinking water. Due to their high persistency, they can bioaccumulate even if their concentrations are to µg/L or ng/L, with consequent problems for both human health and environment.

The European Community has issued regulations to protect water from pollution and to manage water sources. However, only those substances that are commonly found in the environment at a significant concentration levels and posing a threat to the environment and/or human health, are covered by legal norms (compounds regulated by law). According to Art. 16 of Directive 2000/60/EC (Water Frame Directive, WFD), a list of the priority substances (PSs), that is, all the chemicals whose presence in the environment poses a risk to the aquatic environment, was drawn up. The Directive goal is to decrease the natural substances to the background levels and the man-made synthetic pollutants close to zero. In order to

achieve a good ecological and chemical status of water, two Environmental Quality Standards (EQS), the average annual value (AA-EQS) and the maximum allowable concentration (MAC-EQS), acquired from chronic and acute toxicity data, respectively, were indicated.

With the Decision 2455/2001/EC, a first list of 33 PSs was compiled, but only with the Directive 2008/105/EC [18], a daughter directive of the WFD, the EQS for all 33 PSs and 8 other pollutants was established. With the Directive 2013/39/UE, the PSs list was extended to 45 priority substances of which 41 organic compounds and 4 metals (cadmium, lead, mercury, and nickel) and 8 other substances with EQS for a total of 49 organic pollutants and 4 metals (the complete list is reported in Annex A) [19].

Despite the high attention paid by European Community to water pollution, only a small number of compounds is covered by the legal regulations and systematically monitored (Figure 2), many others are outside of any control.

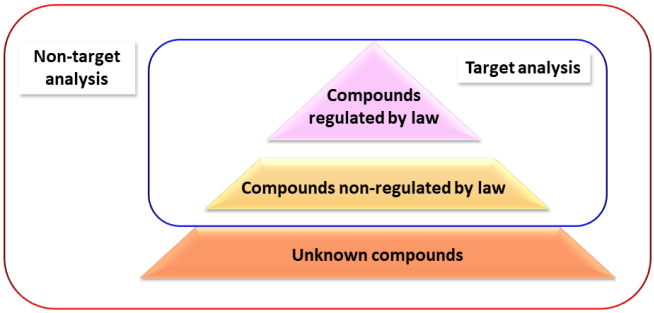

Figure 2. Types of compounds found in the aquatic environment.

Although the number of potential contaminants is essentially infinite, a number of them (chemicals that were not previously detected with a negative effect on the environment) have been referred as Compounds of Emerging Concern (CECs) [20]. A watch list of these contaminants was proposed in the Decision 2015/495/EU, where 10 chemicals or groups of substances (Table 1) were identified to collect data at EU level [21].

Table 1. Watch list of substances for Union-wide monitoring as set out in Article 8b of Directive 2008/105/EC.

Name of substance/group of substances	CAS number[1]	EU number ([2])	Maximum acceptable method detection limit (ng/L)
17-Alpha-ethinylestradiol (EE2)	57-63-6	200-342-2	0.035
17-Beta-estradiol (E2), Estrone (E1)	50-28-2, 53-16-7	200-023-8	0.4
Diclofenac	15307-86-5	239-348-5	10
2,6-Ditert-butyl-4-methylphenol	128-37-0	204-881-4	3160
2-Ethylhexyl 4-methoxycinnamate	5466-77-3	226-775-7	6000
Macrolide antibiotics([6])			90
Methiocarb	2032-65-7	217-991-2	10
Neonicotinoids ([7])			9
Oxadiazon	19666-30-9	243-215-7	88
Tri-allate	2303-17-5	218-962-7	670

([1]) Chemical Abstracts Service.

[(2)] European Union number — not available for all substances.

([3]) To ensure comparability of results from different Member States, all substances shall be monitored in whole water samples.

([6]) Erythromycin (CAS number 114-07-8, EU number 204-040-1), Clarithromycin (CAS number 81103-11-9), Azithromycin (CAS number 83905-01-5, EU number 617-500-5).

([7]) Imidacloprid (CAS 105827-78-9/138261-41-3, EU 428-040-8), Thiacloprid (CAS 111988-49-9), Thiamethoxam (CAS number 153719-23-4, EU 428-650-4), Clothianidin (CAS 210880-92-5, EU number 433-460-1), Acetamiprid (CAS 135410-20-7/160430-64-8).

1.2 Advanced oxidation processes (AOPs)

The AOPs are based on hydroxyl radical ($OH^{\bullet}$) production, a highly reactive free radical (E_0 = 2.33 V) and electrophile that can react with organic substances in different ways:

a) Radical addition (reaction 1).

b) Hydrogen abstraction (reaction 2).

c) Electron transfer (reaction 3) [22].

$$R + OH^{\bullet} \longrightarrow ROH \qquad (1)$$

$$R + OH^{\bullet} \longrightarrow R^{\bullet} + H_2O \qquad (2)$$

$$R_n + OH^{\bullet} \longrightarrow R_{n-1} + OH^{-} \qquad (3)$$

They can degrade a wide range of organic pollutants in simpler molecules with reaction rate constant of 109 L/mol s, 75 times faster than conventional oxidant such as H_2O_2 or $KMnO_4$ [23].

There are some benefits to improve the WWTPs with AOPs methods, for example photocatalysis:

- ✓ possible total mineralization of organic contaminants to CO_2, H_2O (Figure 3), and inorganic ions.
- ✓ prevention of chemical or biological sludge production.
- ✓ non-selectivity.

Figure 3. Organic pollutants degradation in presence of hydroxyl radicals.

There are many different pathways for $OH^{\bullet}$ generation (Figure 4) in AOPs; photocatalysis is the most typical [23–34].

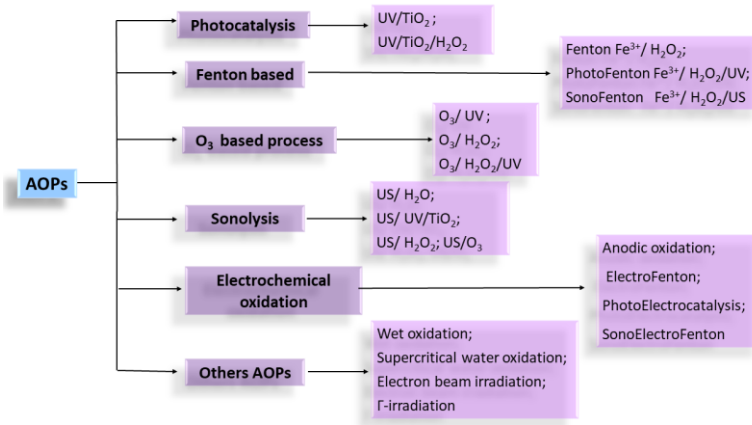

Figure 4. Advanced oxidation processes (AOPs)

1.2.1 Photocatalysis

In AOPs, a photocatalytic process combines the electromagnetic radiation to powerful oxidants such as H_2O_2 and O_3 and catalysts based on iron (homogeneous photocatalysis) or semiconductor photocatalysts as TiO_2, ZnO, etc (heterogeneous photocatalysis).

In recent years, the use of heterogeneous photocatalysis for the treatment of a broad spectrum of contaminants, like dyes, pesticides, pharmaceuticals, personal care products and endocrine disrupting

compounds has increased rapidly [35]. In fact, in the last 30 years, the number of papers, having photocatalysis for wastewater treatment as keyword has steadily increased reaching more than 650 papers published only in the 2020 (Figure 5).

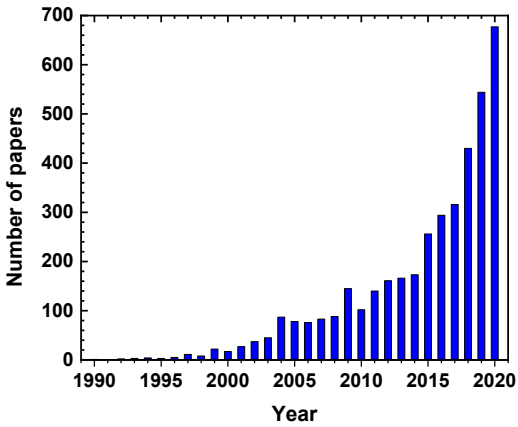

Figure 5. Number of papers on photocatalysis by year (1989-2020).[36]

Heterogeneous photocatalysis was developed after the 1970s, when Fuiishima and Honda showed the photoelectrochemical decomposition of water using a photoexcited TiO_2 semiconductor (Fujishima et al. 1972). This pioneering work, where TiO_2 was used for the oxidation of cyanide ions in aqueous solution, paved the way for environmental applications [38–41].

In heterogeneous photocatalytic processes, when a semiconductor is irradiated by an appropriate photon energy (hv) higher than or equal to the

bandgap energy (E_g), electrons are excited and pass from the valence band (VB) to the conduction band (CB) creating a hole-electron pair (h^+-e^-) (Equation 5). The holes generated in the valence bond have a strong oxidation capacity and react with water to produce hydroxyl radicals (Equation 6), while electrons (strong reduction capacity) interact with dissolved oxygen and generate the superoxide radicals (Equation 7).

$$\text{Photocatalyst} + h\nu \longrightarrow e^- + h^+ \quad \textbf{(5)}$$

$$h^+ + H_2O \longrightarrow OH^\bullet + H^+ \quad \textbf{(6)}$$

$$e^- + O_2 \longrightarrow O_2^{\bullet -} \quad \textbf{(7)}$$

$$h^+ + RX_{ad} \longrightarrow TiO_2 + RX_{ad}^{\bullet +} \quad \textbf{(8)}$$

Organic contaminants can undergo oxidative reactions with the hydroxyl radical generated from the hole and they go through reductive reaction with electrons (Figure 6) [42].

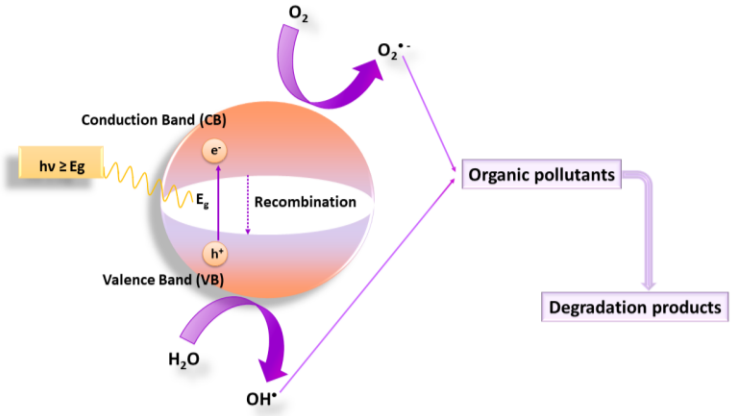

Figure 6. Photocatalytic mechanism for pollutants degradation.

An ideal catalyst should be chemically and photochemically stable, economical, and easily available and have good properties such as light absorption, good combination of their electronic structure and easy to prepare [25,43,44].

Thanks to their good features such as efficiency in the photocatalytic process, the most widely applied semiconductors in AOPs are nanoparticles of TiO_2, ZnO, SnO_2, WO_3, Fe_2O_3 and CdS.

Titanium dioxide (TiO_2) has been the most widely used semiconductor in photocatalytic applications. It could be considered an ideal photocatalyst thanks to its high stability in a wide pH range (from 1 to 14), very simple production and low-cost [25,45]. It can occur in nature in two different polymorphic forms: anatase and rutile. The crystalline structures of the two forms are reported in Figure 7. Both lattices are tetragonal, with cell

distances of $a = b = 4.49$ Å, $c = 3.01$ Å and $a = b = 3.77$ Å, $c = 9.56$ Å for rutile and anatase, respectively.

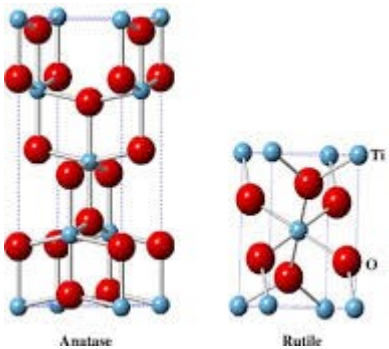

Figure 7. TiO_2 polymorphic crystalline form: anatase and rutile.

The VB energy level is the same for the two polymorphic forms and is equal to 2.64 V at natural pH (Sakthivel et al. 2003), while the conduction band changes for each configuration so the optical absorption depends on the different electron transition process. Thus, the E_g for anatase and rutile are about 3.2, and 3.0 eV, respectively (Di Paola et al. 2013; Luttrell et al. 2014).

Anatase is a metastable TiO_2 polymorphic form with atom defection (normally oxygen vacancies are present) and at high temperatures (600 – 800 °C) can be transformed into rutile [49,50], the most thermodynamically stable structure. However, anatase is the form with the highest photocatalytic activity [48].

Zinc oxide (ZnO) is also widely used in photocatalytic applications. There are three different crystalline structure for ZnO: cubic rocksalt, zinc blende, and wurzite (Figure 8). The thermodynamically stable form under normal condition is the hexagonal wurtzite with cell distances a = 3.25 Å and c = 5.2 Å.

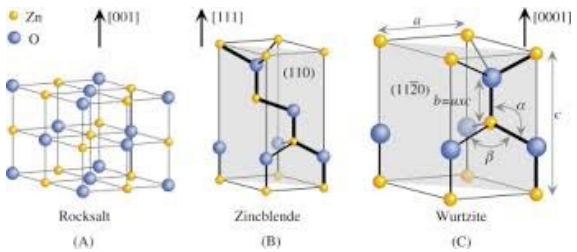

Figure 8. Crystalline ZnO polymorphic forms: rocksalt, zinc blend, and wurzite.

Its behaviour is comparable to TiO_2, with a similar bandgap energy and photooxidation pathway. Although, ZnO has an electronic mobility two orders of magnitude higher than that TiO_2, the latter is still the preferred because ZnO could give photo-corrosion under certain pH conditions and release highly toxic Zn ions.

Unfortunately, the field of application of these two semiconductors is limited because they are active only in the UV range of the electromagnetic spectrum and they have a fast recombination of the electron-hole pair generated [51].

In photocatalysis, the design of catalysts that exert their activity in a wide range of wavelengths, and exploit sunlight can also make this technology sustainable. In fact, due to energy shortage and environmental pollution, sunlight-based photocatalysis has recently become a promising strategy to solve the problems (Liu et al. 2020). To enhance photocatalysts performance, improving their activity under visible and solar light irradiation, preventing charges recombination and decreasing the electrical costs of the process due to the use of lamps, different strategies have been employed to achieve the purpose, introducing (doping) into the crystalline structure of the semiconductor some metal cations (Cr^{3+}, Cu^{2+}, Ni^{3+}, Fe^{3+}, Co^{2+}, etc.) or non-metal anions [53–56] (N, S, P, B, etc.) or building composite materials (heterojuncted semiconductors).

1.2.1.1 Doped-TiO_2

The TiO_2 doping with nitrogen is one of the most widely used procedure to improve the photocatalytic properties of the semiconductor. These procedures increase the photocatalytic activity generating new midgap states, as observed in Figure 9 for the N-doped TiO_2 [57].

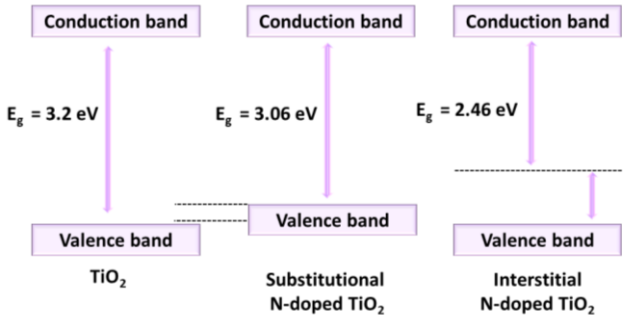

Figure 9. Band structure of undoped TiO_2 and N-doped TiO_2.

Studies have shown that N-doped TiO_2 is able to absorb visible light and have a better photocatalytic performance among the other dopants.

Different methods can be used to prepare N-doped TiO_2:

- **Sol-gel method**. Titanium isopropoxide, used as precursor of TiO_2, is dissolved in an alcohol solution to which nitrogen (usually NH_3, urea or NH_4Cl) is added. During the precipitation, nitrogen is included into the TiO_2 lattice [58–61].
- **Annealing method**. TiO_2 is annealed in at high temperature (500 – 700 °C) with and inert gas flow containing a donor of nitrogen atoms [62].
- **Electrochemical doping**. Doping occurs using a solution containing triethylamine or urea under constant potential [55,63].

- **Hydrothermal method**. Reagents mixture is added to a Teflon-lined stainless autoclave and hydrothermally treated at high temperature (120 – 160 °C) [64,65].
- **Doping using plasma**. Titanium isopropoxide, water vapor and N_2 gas are mixed and delivered in a pyrex plasma reactor at 400 °C [66].

1.2.1.2 Semiconductor heterojunction

Recently, new photocatalysts based on coupling different semiconductors (heterojunctions) are prepared to enhance their photocatalytic performances such as light adsorption extensions to higher wavelength regions, higher electron-hole (e^-–h^+) pairs separation. (Sacco et al. 2020; Kumar et al. 2020)

Wang et al. (Wang et al. 2014) evidenced four different classes of heterojunction photocatalysts (Figure 10):

1. **Semiconductor – Semiconductor (S-S)** (Figure 10a): electrons generated by excitation can transfer from CB of one semiconductor to CB of the other semiconductor.
2. **Semiconductor – Carbon NanoTube (S-CNT)** (Figure 10b): heterojunction with carbon-based materials allows increasing the specific surface area, shifting the light absorption to the visible region, and enhancing electron mobility. A photon excites an electron from the

VB to the CB of the semiconductor and the photogenerated electrons are transferred to the CNTs while the holes remain on the semiconductor to take part in redox reactions.

3. **Semiconductor – Metal (S-M)** (Figure 10c). The charge density is redistributed when they are irradiated. Electrons move from one material to another at the interface.
4. **Multicomponent heterojunction** (Figure 10d) (S-M-S). The photons hit both S-A and S-B producing photogenerated holes and electrons in their VB and CB, respectively. The electrons in the CB of S-A flow easily into the metal (electron transfer I: S-A – M). As result, more holes, with strong oxidation power in the VB of S-A, escape pair recombination and are available to oxidise pollutants or OH. At the same time, the holes in the VB of S-B pass easily into the metal (electron transfer II: M – S-B), because the energy level of the metal is above the VB of S-B.

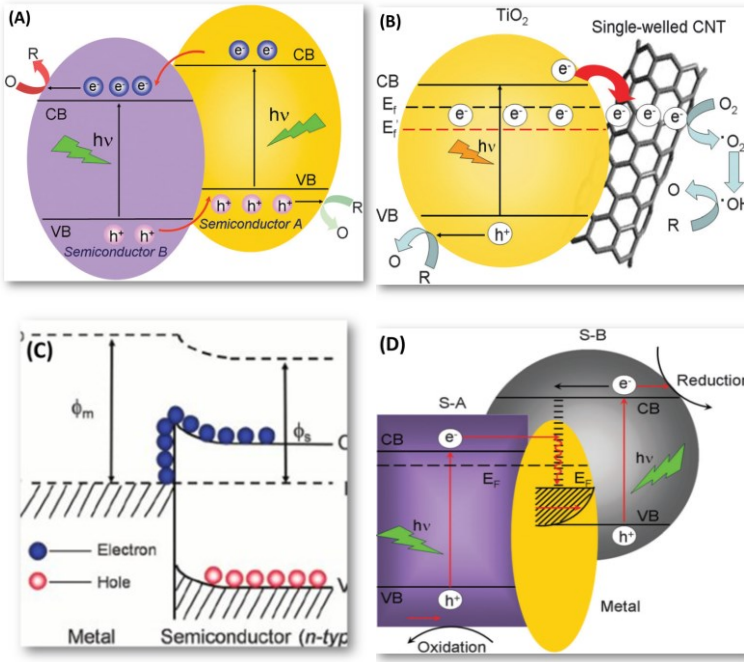

Figure 10. Schematic electron transfer for different heterojunctions: (A) S-S heterojunction; (B) S-C heterojunction; (C) S-M heterojunction; (D) multicomponent heterojunction.

An example of S-S heterojunction is reported in Figure 11. When the semiconductors are in contact, they establish a p-n junction. The light irradiation in the junction drives electrons and holes in opposite directions due to an intrinsic electrical potential. The electrons are shifted to semiconductor CB with lower potential (n-type semiconductor) and the holes to the VB of semiconductor with higher one (p-type semiconductor)

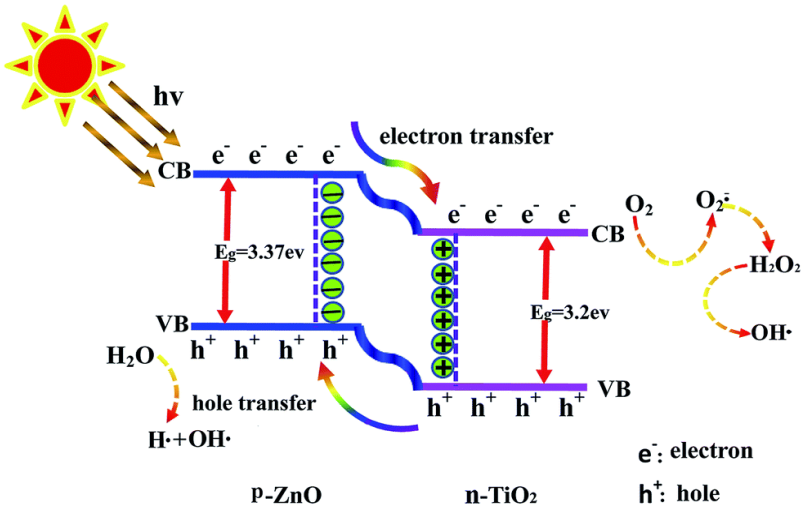

Figure 11. Schematic diagram showing the energy band structure and electron–hole pair separation in the p–n heterojunction.

Instead, the generated electrons migrate from the VB of the first semiconductor to the second one, which possesses a lower VB potential to occupy the generated holes, inducing an excess of positive charge in the VB of the first semiconductor. As result, the number of available charges increases, allowing a higher rate of generation of reactive oxidant species (ROS) that can oxidise pollutants [67].

Recently, several TiO_2-based heterojunction systems, such as ZnO/TiO_2, WO_3/TiO_2, Bi_2WO_6/TiO_2, SnO_2/TiO_2 have been studied [67].

The synthetized Bi_2WO_6/TiO_2 heterojunction displayed a photocatalytic activity 8 times higher than neat Bi_2WO_6 for acetaldehyde (CH_3CHO) degradation in CO_2 atmosphere under visible light irradiation. Studies [68] conducted on the photocatalytic degradation of Rhodamine B with the

same heterojunction have shown that after 30 minutes the substance is completely degraded, while using only the two single catalysts (Bi_2WO_6 and TiO_2) the degradation was about 20%.

Likewise, SnO_2/TiO_2 heterostructured photocatalyst has been tested for the degradation of Rhodamine B showing photocatalytic activity 2.5 times higher than that TiO_2 alone leading to a complete degradation after 60 minutes (Wang et al. 2014).

Among all TiO_2-based heterojunction composites, the photocatalytic activity of bicomponent ZnO/TiO_2 have been studied proving to be a good candidate for environmental applications thanks to their good photocatalytic properties. For example, Wang et al. reported a degradation of methyl orange (MO) of 93.3% after 5 h with TiO_2/ZnO heterojunction in contrast to 2.2% degradation in photolysis [70].

Despite the promising photocatalytic properties of heterojunction-based systems, some issues (i.e., high charge recombination rate of metal oxides, low wavelength absorption range, UV light use) are to be solved [71]. In paragraph 1.2.1.1 it has been highlighted that TiO_2 doping with nitrogen generates a semiconductor able to better absorb visible light, generating semiconductors with higher photocatalytic properties. It has been also shown that the photocatalytic activity of TiO_2 is dependent on the crystalline phase [72]. In fact, TiO_2 N-doping can hinder phase

transformation from anatase to rutile that causes photocatalytic activity loss [73,74].

1.2.1.3 Zero valent iron catalysts Fe^0/ZnS

In addition to these materials, in the last years several others nanoparticles (i.e., zeolites, metal oxides, carbon materials and metals) have been proposed as the more efficient, and environmental friendly technology for photocatalytic applications (Stefaniuk et al. 2016; Dong et al. 2016; Shah et al. 2019).

Among them, an interesting and promising metal nanoparticle is the nano zerovalent iron (Fe^0) [76,78]. Thanks to its large surface area and high reactivity, it is able to remove different water pollutants.

The degradation mechanism occurs on the surface of metal iron [79]. It reacts with the contaminant losing electrons and oxidizing to Fe^{2+}/Fe^{3+}, worsening the reactivity. To improve the performance of Fe^0, some authors have proposed to couple the iron with suitable semiconductors (i.e., TiO_2, ZnO, ZnS, etc.) in order to exploit their photocatalytic effect and induce, in the presence of external light source, the formation of photogenerated electrons able to reduce the Fe^{2+}/Fe^{3+} to Fe^0.

The choice of a suitable semiconductor is related to the values of E_{VB} and E_{CB}. Sacco et al. used ZnS as the semiconducting material to couple with Fe^0. The effectiveness of regeneration and reusability of catalytic system

(Fe^0/ZnS) was tested in the removal of an azo-dye (Eriochrome black T-dye, EBT) and a chlorinated organic compound (tetrachloroetylene, PCE) from aqueous solutions under UV light irradiation (Sacco et al. 2021). It is worthwhile to note that PCE is poorly degraded by hydroxyl radicals generating during irradiation. For this reason, Fe^0/ZnS photocatalyst was studied for its photodegradation. In Figure 12 are reported the EBT degradation results of Fe^0/ZnS under UV light irradiation and in dark conditions.

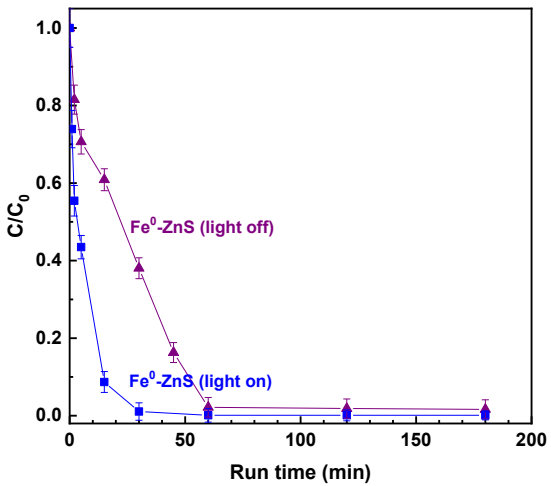

Figure 12. Comparison of EBT degradation efficiencies using Fe^0/ZnS in dark conditions (light off) and in presence of UV light (light on) (Sacco et al. 2021).

The Fe^0/ZnS heterojunction presented a very fast EBT degradation (greater than 99% after 30 min) under UV light respect to 60% after the same time, during an experiment without irradiation.

To evaluate the recycling efficiency of Fe^0/ZnS heterojunction, the EBT degradation were carried out using the composite for six successive cycles without any regeneration step without and under UV irradiation (Figure 13).

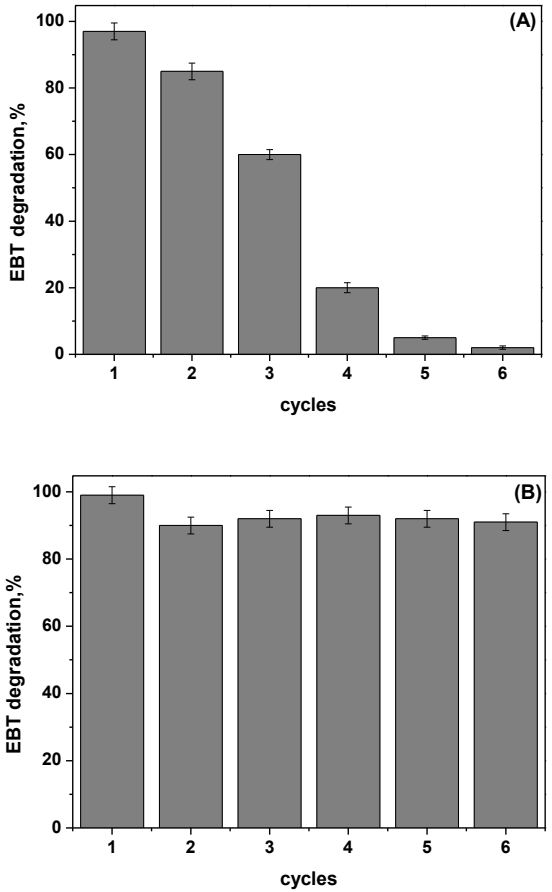

Figure 13. Reuse cycles of Fe^0-ZnS without (A) and with UV irradiation (B). The EBT degradation % was evaluated after 60 min of treatment time (Sacco et al. 2021).

After six successive cycles, the EBT percentage degradation decreased to a value of 2% in absence of UV irradiation (Figure 13a), confirming the progressive oxidation of Fe^0 to Fe^{2+} with a subsequent deactivation of the catalyst. When the catalyst was irradiated by UV light, the efficiency of the catalyst remained unchanged with a 90% of EBT degradation after six cycles (Figure 13b).

1.2.2 Conventional supporting materials for powder catalysts

Although heterogeneous photocatalysis has been widely used for the degradation of contaminants, one of the biggest issue is the necessity to recover the catalyst from treated water to avoid the possible release of nanoparticles into the aquatic environment with consequent genotoxicity and cytotoxicity problems to aquatic organisms [81].

A way to make heterogeneous photocatalysis an eco-friendly process could be to immobilize the powder photocatalysts on different supporting materials for an easy recover of the nanoparticles. In Table 2 are reported advantages and disadvantages of slurry-type and immobilized photoreactors.

Table 2. Some advantages and disadvantages of slurry-type and immobilized photoreactors.

Slurry type photoreactors	Immobilized photoreactors
Advantages • Uniform distribution of catalysts. • Higher ratio of illuminated photocatalytic surface area to reactor volume. • Since the catalyst in reactor is continuously added and removed, the catalyst fouling effects are largely minimised. • Better mixing of particle in the form of suspension. • Decrease in pressure drop through the reactor. • Almost no mass transfer limitations.	***Advantages*** • Can provide continuous operation of the reactor. • Improvement in the removal of organic material from aqueous phase while using immobilising agents with adsorptive properties. • Separation of the catalyst from the final treated effluent stream is extremely easy.
Disadvantages • Requires tedious and expensive post-treatment filtration processes for the recovery of photocatalyst from the treated wastewater effluent streams. • At higher catalyst loading, suspended catalysts tend to cause scattering of light, thereby reducing the rate of photocatalytic reactions. • Aggregation of catalytic particles especially at higher concentrations. • Ecotoxicological problems related to catalyst release into the environment.	***Disadvantages*** • Possible catalyst deactivation and catalyst washout. • Lower catalyst accessibility to photons. • Significant external mass transfer limitations at low flow rates of the pollutant to be treated. This is because of an increase in diffusion path length of the reactant from the bulk to the catalyst surface. • With an increase in catalyst film thickness, internal mass transfer may play dominant role by limiting the utilisation of the supported photocatalyst.

A good supporting material for the photocatalysts in AOP applications should be optically transparent and able to permanently immobilize the nanoparticles. Besides, it should have a good chemical and mechanical stability with a possible capacity of contaminants adsorption.

The most commonly used supporting materials are:

1. **glass**, in different physical forms (plates, beads, etc.) on which the photocatalyst is permanent fixed.
2. **activated carbon** (carbon nanotube or graphene oxide) supports.
3. **clay** or **ceramics**, normally used as layers.
4. **polymeric films** (polyethylene, polystyrene, polyvinyl chloride, expanded polystyrene, polyaniline, poly methyl methacrylate) [35].

Polymer media are attractive because they are inexpensive, easily available, and chemically inert with good mechanical properties and durability. However, as shown in Table 2, also this solution has some drawbacks: in fact, the anchorage of the catalyst to the support can generate a possible decrease of the photocatalytic activity due to a reduction of available surface of the photocatalyst.

1.2.3 Porous supporting materials

Using porous materials as support matrix could overcome the problem related to the use of classic supports as anchoring generally leads to the reduction of the available photocatalytic area and consequently of activity. In fact, thanks to their ability to preconcentrate contaminants absorbed in the porous structure, they can contribute to the enhancement of photodegradation [82]. Additionally, porous sites can trap reaction

intermediates or by-products with an improvement of the degradation process.

The design and construction of micro- and/or nanoporous architectures have been studied for a long time. Among all structures, porous polymers represent an attractive class of materials, as they possess both the properties of porous supports and polymeric materials. It is possible to design materials with high surface areas and well-defined porosity, and because they are polymer-based they are easy to process, and can be easily produced in polymer or thin film forms [83]. Among them, aerogels, a class of solid materials, consisting of a three-dimensional porous linkage with networking of micro and mesoporous, are very interesting and promising support materials. They were developed by Kistler [84] using supercritical drying in the first years of the 1930s leading to the development of aerogels based on organic, inorganic or even hybrid compounds [85]. With this process, the structure of the gel is kept intact by the solvent removal [86].

The sol-gel method is used for aerogel preparation. The steps of sol-gel procedure to obtain aerogel composite filled with the photocatalysts are shown in Figure 14.

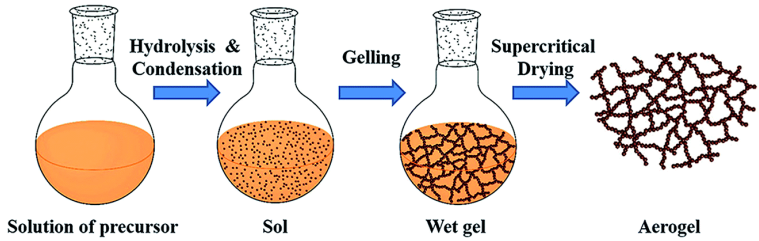

Figure 14. Different routes of aerogel and aerogel composite preparation.[87]

Step 1: A solution of molecular precursors is transformed into a colloidal suspension (sol). To obtain a composite catalyst/precursor aerogel, a multicomponent sol would be prepared by adding the photocatalytic particles to the precursor in the step 1 [85].

Step 2: Adding a chemical crosslinker or changing the physical conditions of the reaction (e.g., pH or temperature), the sol is transformed in a gel.

Step 3: After gelation, the aerogel is formed by a drying step.

Other interesting characteristics of aerogels are the lightness and hydrophobicity, which make these materials able to float on water promoting an easy recover after each treatment cycle [88–90].

Nowadays, the more used classes of aerogel for photocatalytic application in water treatment are:

- **SiO_2 – based aerogels**. Promising aerogel supports thanks to their good mechanical properties and easy synthetic routes by sol-gel method. For example, silica-titania photocatalysts aerogel have been used for degradation of different organic pollutants such as cyanide

[91], p-chlorophenol, p-nitrophenol and 4-hydroxybenzoic acid [92,93] and Rhodamine-B [94]. However, the low transfer of the photogenerated charges due to the inert SiO_2 is a great disadvantage.

- **Carbon-based aerogels**. Attracting for their high specific surface area, excellent electron mobility and flexible mechanical properties. These materials have been extensively studied for dyes degradation (Fan et al. 2016; Cai et al. 2015; Liu et al. 2015) in wastewaters. However, the black colour of the aerogel makes them opaque in the visible region. Furthermore, the energetic consuming synthesis via hydrothermal method and their high fragility does not allow large-scale production.
- **Polymeric aerogels**. Different polymeric aerogel, such as syndiotactic polystyrene (sPS) [98–100], polyvinylpyrrolidone (PVP) [101], polyvinyl alcohol (PVA) [102,103] and polyaniline (PANI)[104] have been investigated for photocatalytic application for water remediation due to their good mechanical and chemical stability, easily and low-cost synthesis. Photocatalyst can be appropriately included in the three-dimensional structure of the aerogel during polymerization or gelling process forming composite aerogels with high mechanical properties. In Table 3, other aerogels composite material filled with photocatalysts used for water pollutions degradation are reported.

Table 3. Aerogels photocatalysts for water pollutants degradation [85].

Aerogel photocatalysts	Synthesis	Properties/remarks
BiOBr/reduced graphene oxide (RGO) composite	A one-pot hydrothermal method using L-lysine as a reducing agent and the cross-linker was applied to prepare three-dimensional RGO-based porous network with simultaneous growing BiOBr nanoparticles in its network.	• Excellent dye degradation performance BiOBr under visible light due to charge separation effect of RGO • High surface area with spongy nature • High stability and recyclability from aqueous solutions
Titania–silica microspheres (TSAMs)	A one-pot sol–gel processes in water in oil microemulsion system followed by an ambient pressure drying approach were employed to prepare aerogel microspheres.	• TSAMs contained mean diameters of about 100 μm, a specific surface area of 415 $m^2 g^{-1}$. • A better photocatalytic activity and recyclability than P25 TiO_2 for degradation of MB was achieved.
Nanocrystalline TiO_2	An epoxide mediated sol–gel synthesis followed by super and subcritical dryings with calcination process at 400–700 °C	• Nanocrystalline TiO_2 aerogels calcined at 650 °C has shown a superior photodegradation ability for aqueous phenol. • The photocatalytic activity was correlated with nanocrystalline phase and crystalline sizes.
Binary titania–silica (TiO_2–SiO_2)	A one pot sol–gel reaction by using $TiOCl_2$ and sodium silicate as precursors	• Aerogel has hydrophobic properties. • Increasing the calcination temperature up to 400 °C increased the surface area. • Photodegradation ability of aerogels toward (MB) were correlated with their morphostructural and hydrophobic properties as well as calcination temperature.
Nanoglued binary titania–silica (TiO_2–SiO_2)	A preformed titania with an anatase phase was immobilized on a 3D mesoporous network of silica obtained from sol–gel.	• Aerogels contained a high-surface-area with a Ti^{4+} valency. • The photogenerated hydroxyl radicals ($OH_•$) in the solution were responsible for the oxidation of MB. • The photocatalytic reaction has followed a pseudo first-order Langmuir–Hinshelwood (L–H) kinetic model.

Aerogel photocatalysts	Synthesis	Properties/remarks
$CeVO_4$/graphene composite	Aerogels were prepared by an electrostatic-driven self-assembly method.	• $CeVO_4$ particles were anchored uniformly on the flexible graphene sheets. • The light absorption capability of composite improved with an effective charge transfer from $CeVO_4$ particles to graphene which led to increasing in the photodegradation ability of composites toward MB. • The chemical structure of composites was stable during several cyclic reactions.
Cu_2O/RGO composite	Aerogels were synthesized through a facile one-pot hydrothermal method using glucose as a reducing agent and cross-linker.	• Aerogels were employed for aqueous methyl orange photodegradation. • Enhanced light absorption capability as a result of improved charge separation ability of composite by RGO was achieved. • Easy recycling due to the aerogel's light weight and hydrophobicity was obtained.
SiO_2–SnO_2 composite	Tine oxide was deposited on preformed silica gel through a wet deposition approach.	• Crystallinity and grain size of SnO_2 increased with thermal treatment at >500 °C that caused an improved photocatalytic activity. • Aerogel exhibited rich photoluminesce effects as a result of defects especially for those related to the oxygen-deficient sites. • Aerogel composite has a proven photodegradation performance for decomposition of MB.
N-doped TiO_2 syndiotactic polystyrene nanocomposite (Nt-sPS)	The N-doped-TiO_2 obtained by a nitration process during hydrolysis of titanium alkoxide and then deposited on the syndiotactic polystyrene network.	• The syndiotactic polystyrene support offers a high surface area, low density, and monolithic to the composites. • Photocatalytic activity toward MB under visible light was achieved. • A better photocatalytic activity and recovering ability were achieved in compared to the N-doped-TiO_2 in powdered forms.
TiO_2-Ca alginate polymer fibers composite	The composite was obtained by dispersion of TiO_2 in the hollow alginate fiber matrix through a chemical vapor deposition method.	• High porosity and surface area were achieved for composite compared to their non-porous fiber counterparts • The photodegradation toward MO for composite was much higher (three-fold enhancement) than that of non-porous fiber counterparts as well as TiO_2

Aerogel photocatalysts	Synthesis	Properties/remarks
		powder. • The method of composite development is easily upscalable.

1.2.3.1 High-porous nanocomposites aereogels

Recently, aerogels based on thermoplastic polymer with nanoporous crystalline phase such as syndiotactic polystyrene (sPS) have become very appealing. The presence of a nanoporous crystalline form makes aerogels capable of absorbing organic contaminants from air and water even if they are present at trace level [105,106,106,107], for this reason they are used for different applications such as molecular separation [108], sensors [109–112] and catalysis [113].

sPS has a three dimensional connectivity (3D) given by intermolecular physical bonding with crystalline juncture developed when gelation starts and can constitute thermo-reversible gels with guest molecules of low-molecular mass, like tetrahydrofuran [114], benzene [115], toluene [116], chloroform [115], chlorobenzene, etc. The aerogel is formed after the substitution of solvent molecules with gas ones after supercritical drying. Its structure consists in a blend of macropores with a diameter greater of 50 nm derived from fibrillar polymer architectures and micropores with

pores diameter less than 2 nm between the crystalline structure (Figure 15) [117].

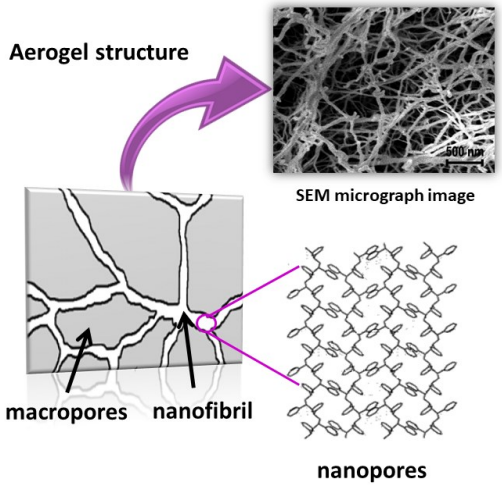

Figure 15. sPS aerogel structure.

In detail, sPS presents two different nanopores forms δ and ε. The δ form has a monoclinic modification characterized by two cavities per unit cell (Figure 16 A,A') and/or a triclinic one with one bigger cavity per unit cell (Figure 16 B,B') able to hold inside the host cavities guest molecules with dimension up to 0.25 nm [118].

While δ form have isolated cavities, the ε form is characterised by an orthorhombic unit cell with channel-shaped cavities (Figure 16 C, C') which can host longer molecules [118].

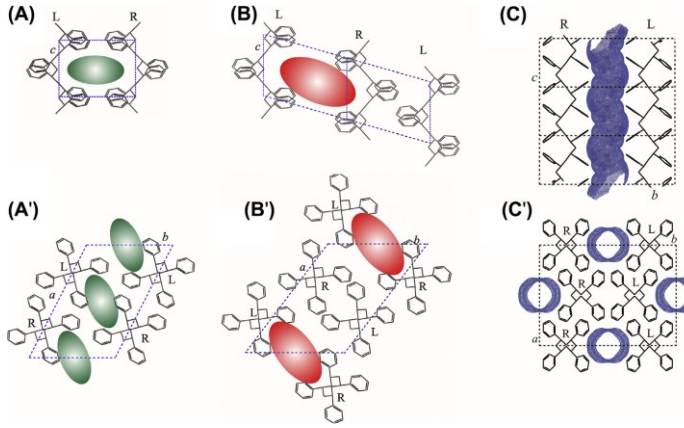

Figure 16. Lateral (A, B, C) and top (A', B', C') views of the structure of the syndiotactic polystyrene nanoporous crystalline forms: monoclinic d (A, A'), triclinic d (B, B'), and orthorhombic ε (C, C'). (Daniel et al. 2016)

A wide range of molecules (volatile organic compounds, halogenated and aromatic hydrocarbons) can be absorbed from water and air by these materials even at low concentration.

Sorption kinetics of sPS aerogel, are very fast thanks to the presence of nanopores with high sorption capacity and macropores with high diffusivities [117].

The fixing of photocatalysts nanoparticles in the sPS aerogel framework allowed the preparation of photocatalytic polymer, named Highly Porous Nanocomposite Aerogels (HP-NcAs) leading to greater efficiency thanks to both aerogel's ability to absorb pollutants and photocatalysts to degrade a large number of organic compounds.

Recent studies on the photocatalytic treatment of two organic pollutants, methylene blue (a model contaminant used for photoactivity tests) and

phenol (one of the first compound listed as PS by US Environmental Protection Agency, US EPA) with HP-NcAs based on sPS and N-doped TiO_2 (sPS/NdT) showed that this material is more efficient under visible (VIS) and UV light than neat NdT powder catalyst [98,100]. In Figure 17, a comparison of the photocatalytic activity of this HP-NcAs with neat NdT powder is shown.

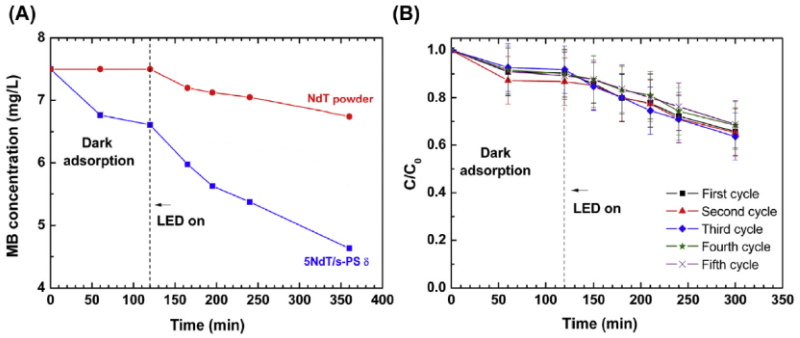

Figure 17. (A) Methylene blue (MB) concentration in aqueous solutions treated with HP-NcA sPS/NdT, and NdT powder. Initial concentration MB = 7.5 mg/L; NdT dosage = 0.13 g/L. (B) MB removal performances obtained with sPS/NdT after 5 recycling experiments. No regeneration step of the aerogel was performed at the end of each cycles.

The composite is effective in MB (initial concentration: 7.5 mg/L) aqueous solution removal, leading to a photocatalytic activity higher than NdT powder (Figure 17A). No loss of efficiency was observed after five successive cycles without regeneration step in the same experimental conditions (Figure 17B) showing that aerogel absorption capacity remains unchanged after each irradiation run and no nanoparticles from the aerogel is released.

Studies conducted by Daniel et al. [119] investigating the photocatalytic activities of two different HP-NcAs (sPS/NdT and sPS/ZnO) towards phenol degradation have shown the usefulness of using such systems in photocatalysis processes.

In Figure 18, A and C the photocatalytic activities towards phenol (initial concentration: 50 mg/L) degradation of 10NdT/sPS (the number indicate the %w/w of photocatalyst in the composite) and 2ZnO/sPS HP-NcAs aerogels with sPS in δ and γ (aerogel without a porous phase) form compared with the bare photocatalysts NdT or ZnO are reported.

In dark conditions (when the phenol solution was not irradiated by UV light), a sorption of 10% of pollutant was observed for all the samples except the γ-sPS/NdT HP-NcA (sorption ~ 1%). A sorption of 5% was observed for the ZnO powder and δ-sPS/ZnO HP-NcA, but no sorption was reported for γ-sPS/ZnO HP-NcA.

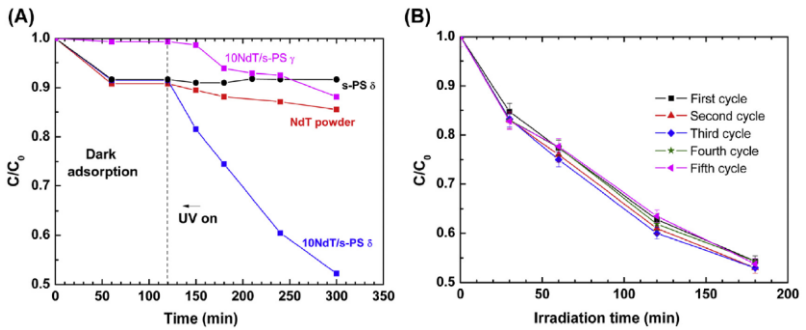

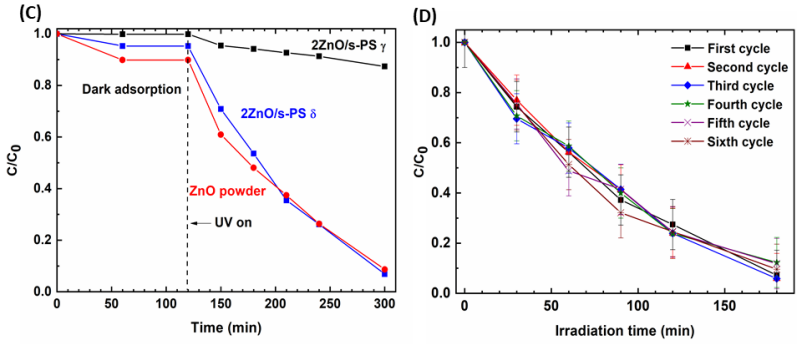

Figure 18. Phenol degradation: (A) Phenol solution treated with HP-NcAs 10NdT/s-PS δ, 10NdT/s-PS γ a, s-PS δ aerogel, and NdT powder. Initial phenol concentration = 50 ppm; NdT dosage = 0.4 g/L, (B) Successive phenol removal cycles obtained with 10NdT/s-PS δ HP-NcA without any regeneration at the end of each cycle. (C) Phenol solution treated with 2ZnO/s-PS δ HP-NcA, 2ZnO/s-PS γ aerogels, and ZnO powder. Initial phenol concentration = 50 ppm**;** ZnO dosage = 0.03 g/L **(**D) Successive phenol removal with δ-sPS/2ZnO HP-Nc aerogel without any regeneration at the end of each cycle.

During the UV irradiation time, no additional decrease in phenol concentration is observed for pure s-PS δ aerogel. For 10NdT/s-PS γ aerogel, neat NdT and 10NdT/s-PS δ HP-Nc aerogel, the phenol degradation after 180 min was 10%, 15% and 48%, respectively (Figure 18A).

The photocatalytic activity for 2ZnO/s-PS δ HP-NcA was higher than that for 2ZnO/s-PS γ aerogels (Figure 18C), indicating that the polymer matrix acts not only as a support in the process but also as a pre-concentrator.

It was also observed (Figure 18B and D) that the photocatalytic activity for the two δ HP-NcAs were very stable. In fact, after 5 successive photocatalytic cycles without performing any regeneration step, the catalytic activity remains unchanged.

In addition, experiments at different pH values showed the aerogel matrix capability to protect the ZnO from dissolution.

Studies conducted by Nakaoki et al. have also shown that the δ-empty sPS form is selective towards molecules with certain shapes of solvent molecules. The study conducted by incorporating a series of alcohols into the cavity showed that as the molar volume of the solvent molecules increased, the diffusion of the molecules into the δ-void sPS decreased. In fact, only alcohols ranging from methanol to n-hexanol were incorporated into the structure, whereas those with longer chains were not, most likely due to their molecular size and conformation [120].

1.3 Ecotoxicological assessment

Nowadays, analytical methods are increasingly accurate and sensitive to recognise and quantify the substances present in the environment, but often no indication of the biological effects on the ecosystem are known. Thus, ecotoxicity assays are very important especially when AOPs are used.because the formation of by-products or intermediates can result in a residual or even increased toxicity [121,122].

In a risk assessment, the contaminant toxicity, both individually and in mixtures, should not be underestimated. Therefore, information to be

included in regulatory frameworks could be provided using rapid and simple methods to assess the toxicity of these matrices.

Several methods to assess the intrinsic toxicity of chemicals and their ecological impact on some receptors at different trophic scale (plant, fungi and algae; invertebrates; fish; amphibians; birds and mammals) have been developed.

Water pollution assessment with toxicity assays started in 1940 in the United States. Since then, a large number of toxicity assays to evaluate the negative impacts generated by contamination on human and environment have been developed according to the ecosystem under consideration and the end-use of the water using different biological tools.

Ecotoxicity tests can be categorized according to [123]:

1. Design (fields, laboratory, modelling)
2. Biological organization level (population, community, ecosystem)
3. Exposure period (acute, sub-chronic, chronic)
4. Endpoint (type of measured biological response)

In order to have an ecotoxicological analysis with a scientific relevance, it is appropriate to use a minimum of three different test species belonging to different taxonomic groups to span a wide range of sensitivities, considering for example bacteria, invertebrates, plants (algae), and vertebrates [124].

Bioluminescent bacteria (*Aliivibrio fischeri*), microalgae (*Raphidocelis subcapitata*) and small planktonic crustaceans (*Daphnia magna*) are the most common species used for water and wastewater toxicity assessment, including both acute and chronic exposure periods for different endpoints. The tests with these crustaceans are advantageous, due to the high sensitivity of the species to toxic substances and the short reproductive cycle of the organisms [125].

1.3.1 Invertebrate

Daphnia magna is the commonly used invertebrate for identify water and wastewater effluents toxicity. Acute (USEPA, 2002; ISO, 1996a) and chronic tests are mentioned. In an acute bioassay, living daphnids are exposed to the target contaminants and after an incubation time of 24 and 48 hours counting. In a chronic test the organisms are exposed for 21 days. these tests are advantageous, due to the high sensitivity to toxic substances and the short reproductive cycle of the organisms [125].

1.3.2 Algae

Bioassays based on algae have been developed (EN ISO 8692, EN ISO 10253, or EN ISO 10710) thanks their ubiquity and short life cycle. The algae are exposed to the pollutants, and after 3 days algal number are

counting, and toxicity evaluate growth rate inhibition by carrying out a toxicity assessment using the algal growth rate [125].

1.3.3 Microbial bioassays

For a test with micro-organisms, the most used organisms are bioluminescent bacteria, *Aliivibrio fischeri,* the standardized test follow ISO 1998. During the test luminescence change is measured when the bacterium is exposed to toxic substances [125].

2 Materials and methods

2.1 Chemicals and reagents

The syndiotactic polystyrene (sPS) used for aerogels preparation was manufactured by Idemitsu Kosan Co., Ltd. under the trademark XAREC© 90ZC. The polymer was highly stereoregular with a content of syndiotactic triads over 98% (^{13}C nuclear magnetic resonance data) as stated in the technical specifications provided by the manufacturer.

Atrazine (ATZ, CAS number 1912-24-9), Thiacloprid (THI, CAS number 111988-49-9) analytical standard with purity equal to or greater than 98%, ZnO (99% pure) and titanium tetraisopropoxide (TTIP, purity of 99.5%) were purchased by Sigma-Aldrich.

Non-woven material (TNT) and biaxially oriented polypropylene (PP) films corona pre-treated were provided by Maca S.r.l.[1]

H_2O (CAS number: 7732-18-5) and acetonitrile (CAS number: 75-05-8) (LC-MS grade, purity equal to 99.95%) used as eluents for HPLC analysis, were purchased from Carlo Erba.

Tetrachloroethylene (PCE) with purity equal to 99.9%.was purchased from Romil.

A PCE standard (1000 mg/L or ppm with purity of 99.9%) in methanol was supplied by the company CPAchem.

Water used to prepare solution was MillQ water.

Ammonia solution 30% supplied by Carlo Erba.

2.2 Target pollutants

To test the samples in photocatalytic processes, target contaminants such as ATZ (priority substance, PS), THI (contaminant of emerging interest, CEC) and PCE (volatile organic compound, VOC) were chosen. The latter are suitable candidates to promote sorption into the sPS polymer matrix (non-polar) and furthermore their size is more compatible for the nanoporous cavities of the sPS being non-ionic organic compounds.

2.2.1 Atrazine

ATZ, molecular structure depicted in Figure 19, is an herbicide belonging to s-triazine family, extensively used for broad-leaf and grassy weed in corn, sugarcane, sorghum, rangeland, macadamia orchards, pineapple, turf grass sod, asparagus, forestry grasslands, grass crops, and roses, registered for the first time in 1958.

[1] Corona treated surface is specifically designed to provide excellent adhesion of ink and lamination and non-treated heat seal surface having good sealing characteristics in order to increase the hydrophilicity of the material.

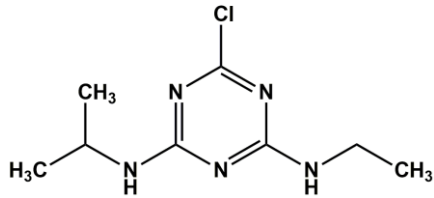

Figure 19. Atrazine molecular structure.

ATZ is a synthetic molecule that appears as a white powder, odorless, very stable, not quite volatile, reactive, or flammable and has a water solubility about 33 mg/L at a temperature of 25 °C.

It has high persistency in soils, long half-life (from 60 to >100 days), high contamination potential and harmful effects of both surface and groundwater. Due to these characteristics, it was classified by the European Community among the PSs [126] and after 12-year of monitoring its use was banned in 2003 by EU [127].

The transformation pathway of atrazine via biotic or abiotic reaction/pathway is an indicator of its persistency and transportation through environment.

Persistency of pollutants is related to the metabolic action of the native microorganism because they are the first natural source implied in contaminants degradation for the preservation of environment.

Many bacteria can degrade atrazine such as *Arthrobacter* sp., *Chelatobacter heintzii*, *Rhodococcus* sp., *Pseudomonas aeruginosa*, etc. [128].

Rhodococcus strain TE1 can decompose atrazine under aerobic conditions, to give deethylatrazine (DEA) and deisopropylatrazine (DIA) (Figure 20).

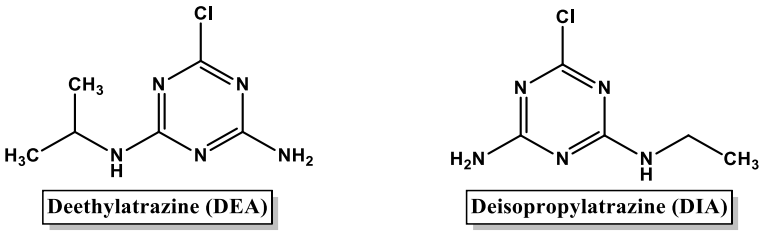

Figure 20. Deethylatrazine (DEA) and Deisopropylatrazine (DIA) molecular structure.

ATZ mineralization pathway is shown in Figure 20. The degradation starts from hydrolytic dechlorination by the action of atrazine chlorohydrolase (atzA or trzN gene product) to give hydroxyatrazine (HA). atzB and atzC catalyze HA conversion to produce two different aminohydrolases (Figure 21, upper degradation pathway).

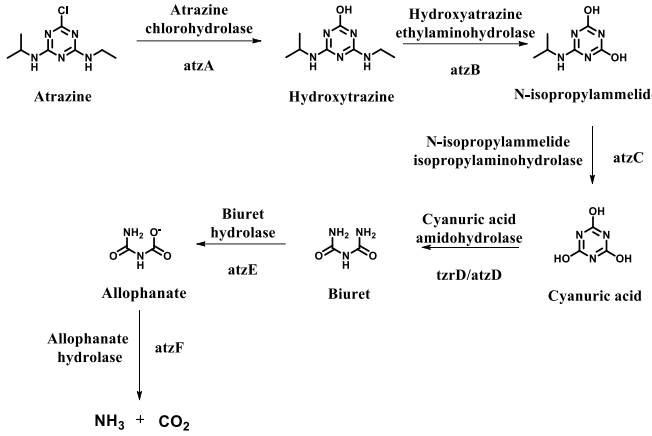

Figure 21. Atrazine biodegration pathway illustrating the genes catalysing the hydrolytic reactions.

The subsequent degradation of cyanuric acid generates, after a series of hydrolytic reactions, carbon dioxide [128,129].

Muñoz et al. [130] investigated the photocatalytic ATZ degradation after 40 h of treatment. The first steps of degradation involve the removal of the alkyl side chains or the replacement of the chlorine atom by a hydroxyl group. The degradation proceeds until cyanuric acid is formed (Figure 22).

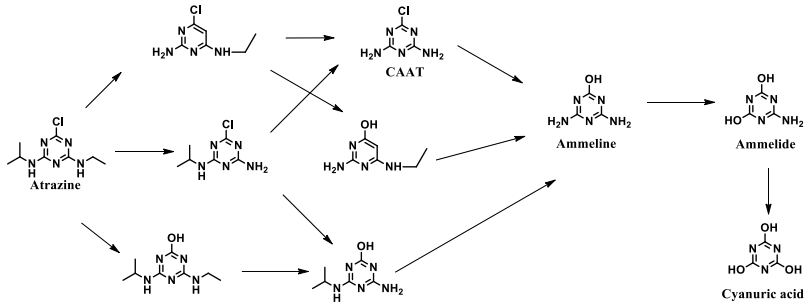

Figure 22. Proposed photodegradation pathway for ATZ.

2.2.2 Thiacloprid

Thiacloprid, molecular structure depicted in Figure 23, is an insecticide, belonging to the second-generation neonicotinoid pesticide, introduced by Bayer Crop Science with the name Calipsol [131,132].

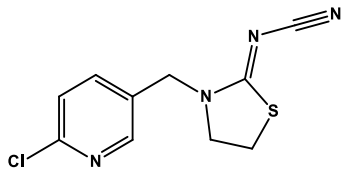

Figure 23. Thiacloprid molecular structure.

Thiacloprid is a yellowish crystalline powder, odourless, with a water solubility of 184 – 186 mg/L at 20 °C. This contaminant has a half-life of over one year in anaerobic aquatic conditions and 10 – 63 days in aerobic aquatic conditions. It is detected in rivers and lakes because of its

persistency, water solubility and mobility. Thiacloprid is released into the environment following its use on soils or in crop fields. Its mechanism of action is similar to other neonicotinoids and involves disruption of the insect nervous system by stimulating nicotinic acetylcholine receptors [98,133]. Thiacloprid has been detected in surface water at concentrations of 0.02 – 4.50 µg/L [134–136]. Few studies exist on the bio degradation of thiacloprid. Some studies reported that thiacloprid can be degraded by the bacterial strain *Stenotrophomonas maltophilia* [137] or pure bacterial culture of *Variovorax boronicumulans* [138].

Thiacloprid biodegradation pathway can proceed via hydroxylation reaction to give 4-hydroxy thiacloprid (THI-I). Successively, THI is at the same time oxidised and decyanated under alkaline conditions to produce 4-ketone thiacloprid imine (via 1, figure 24). Another degradation pathway can proceed by hydrolysis of the *N*-cyanoimino group to form an *N*-carbamoylimino group thiacloprid amide (via 2, Figure 24) [139].

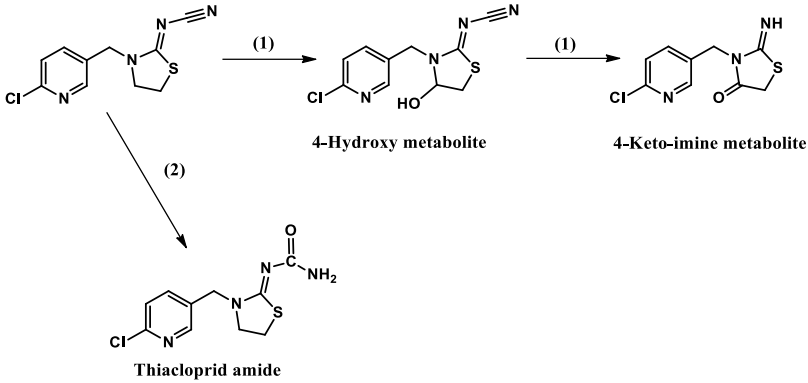

Figure 24. Metabolic pathways for bacterial biodegradation of the neonicotinoid pesticides thiacloprid.

2.2.3 Tetrachloroethylene

Tetrachloroethylene, also known as perchloroethylene (PCE), whose molecular structure is depicted in Figure 25, is an organochloride belonging to the family of volatile organic compounds (VOCs) used for dry cleaning of fabrics and metal-degreasing operations.

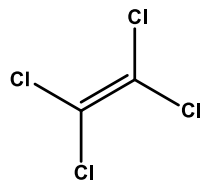

Figure 25. PCE molecular structure.

At room temperature it is a colourless liquid, volatile and non-flammable, that decomposes easily at higher temperatures.

The inertness of tetrachloroethylene also enables it to undergo reduction reactions under normal conditions and oxidation reactions by photochemical effect, especially at high temperatures, with the consequent loss of a chlorine atom and the formation of trichloroethylene.

It is also poorly soluble in water (206 mg/L) at 25°C while it is miscible with most organic solvents. It is considered a probable carcinogenic compound by the International Agency for Research on Cancer. PCE is classified as a USEPA priority toxic pollutant and is toxic to humans, animals and aquatic life with a biodegradation rate from months to years [140].

2.3 Preparation of photocatalysts

2.3.1 NdT nanopowder

N-doped TiO_2 photocatalysts were prepared by the sol-gel method using ammonia as a nitrogen source and titanium tetraisopropoxide (TTIP), according to the procedure developed by Sacco et al. [141]. Ammonia aqueous solution (100 mL) was added drop wise to 25 mL of TTIP at 0 °C under stirring. The reaction involved the formation of a white precipitate that was washed with MilliQ water and centrifuged. Finally, the obtained

precipitate was calcined at 450 °C for 30 min to get an optimized photocatalysts active under visible irradiation named NdT.

2.3.2 xZnO/NdT heterojunction

The preparation of ZnO/NdT heterojunction could be interesting because both semiconductors have interesting properties. In fact, NdT exerts its photocatalytic activity under sunlight irradiation, while ZnO shows higher photocatalytic activity than TiO_2 in the oxidation of organic compounds under UV irradiation [142]. For this reason, catalysts-based heterojunctions xZnO/NdT have been prepared and tested in atrazine photodegradation under UV-A, Vis and sunlight irradiation, to exploit the good photocatalytic properties of both NdT and ZnO semiconductors maximizing, in this way, the photocatalytic efficiency of catalyst.

The ZnO/NdT catalysts were prepared by appropriately mixing two single semiconductors, commercial zinc oxide (ZnO) and NdT as described in 2.3.1. The following steps to prepare S-S heterojunction photocatalysts with different composition have been taken: 1) the appropriate weighed amounts of ZnO and NdT were added to an aqueous solution (100 mL) of 1M isopropanol. In table 4 are reported the weight of two semiconductors used to prepare S-S heterojunction material.

Table 4. ZnO and NdT amounts used for xZnO/NdT photocatalysts.

ID	m_{ZnO} (g)	m_{NdT} (g)
50ZnO/NdT	0.5	0.5
30ZnO/NdT	0.3	0.7
15ZnO/NdT	0.15	0.85
2.5ZnO/NdT	0.025	0.975

The samples were left stirring at 80 °C until the solvent had evaporated completely and the straw-yellow precipitates, which became softer as the amount of ZnO increased, were recovered.

2.3.3 Fe^0/ZnS powder photocatalyst

Fe^0 and Fe^0/ZnS were synthetized according to Yan et al. [143]. $FeSO_4$ (4 g) were added to 100 mL of water and stirred for 10 min. A gaseous He flow (flow rate: 30 NL/h) was bubbled inside the system to remove dissolved oxygen from the aqueous phase. Afterward, an excess of reducing agent (30 % w/w $NaBH_4$) was added. The right amount of $NaBH_4$ was evaluated considering the stoichiometric ratio pointed out in equation 10.

$$Fe^{2+} + BH_4^- + 2\ H_2O = Fe^0 + BO_2^- + 2H^+ + 3H_2 \qquad (10)$$

The suspension was left under stirring in the presence of He flow for 1 h, washed with MilliQ water for three times and finally dried overnight at room temperature. The procedure to prepare Fe^0/ZnS was the same as that just illustrated except that 1 g of ZnS was added to the initial solution of $FeSO_4$.

2.3.4 Pure sPS and HP-NcAs preparation

Pure polystyrene syndiotactic in δ form (sPS) aerogels were prepared by sol-gel method according to the procedure of Daniel et al. [118]. Different sPS amounts (0.608, 1.568, 2.82, 7.45 g) were added to 20 mL of chloroform ($CHCl_3$) in hermetically sealed test tubes. The mixture was heated at 100 °C to dissolve completely the polymer and obtain a transparent and homogeneous solution. Cooling the samples at room temperature, a gelation occurs. The gels were dried with supercritical CO_2 using a SFX200 supercritical carbon dioxide extractor (ISCO Inc.) under the following conditions: T = 40 °C, P = 200 bar, extraction time =4 h. Four different sPS polymers at different weight ratios solvent/polymers (98/2, 95/5, 90/10 and 80/20), named 2sPS, 5sPS, 10sPS and 20sPS, were obtained, in order to choose the best polymer matrix for the preparation of HP-NcAs systems that would give the best absorption of atrazine.

For the preparation of the different HP-NcAs (nanocomposite aerogel/photocatalyst), the procedure shown in Figure 26 was followed.

The preparation of the sPS/NdT sample is given as an example. The sPS pellets and NdT photocatalyst (sPS/NdT weight ratio 90/10, optimised weight/ratio in the studies mentioned in the state of art) were dispersed in $CHCl_3$ inside hermetically sealed test tubes and heated at 100 °C until complete polymer solubilization. The tubes were subsequently cooled to room temperature to form a gel. The gels were dried with supercritical CO_2 using the same condition described above to obtain the HP-NcAs.

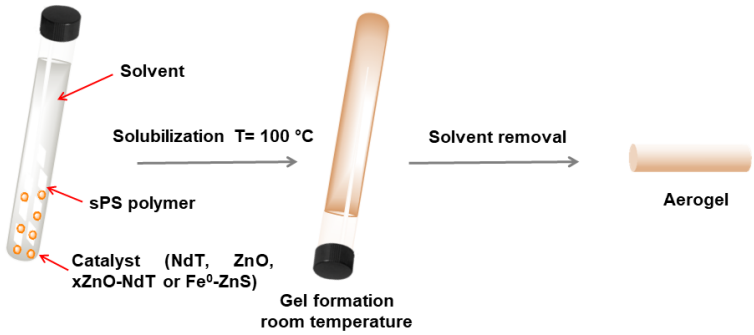

Figure 26.Schematic overview of the preparation procedure of HP-NcA sPS/NdT.

In each individual HP-NcAs preparation, both the weight ratios sPS/solvent and sPS/photocatalyst were varied. The various ratios used for the preparations are shown in Table 5.

All aerogel samples used for the photodegradation tests had a cylindrical shape, with a diameter of 5.6 mm and a length of c.a. 3 cm.

Table 5. sPS/solvent and sPS/photocatalysts weight ratios for HPNcAs preparation.

Samples	sPS/solvent (w/w)	sPS/catalysts (w/w)
2sPS	2/98	-
5sPS	5/95	-
10sPS	10/90	-
20sPS	20/80	-
5sPS/NdT	5/95	90/10
10sPS/NdT	10/90	90/10
5sPS/ZnO	5/95	98/2
sPS/[2.5ZnO/NdT]	5/95	95/5
sPS/[30ZnO/NdT]	5/95	95/5
sPS/[Fe0/ZnS]	10/90	97/3

2.3.5 Polymeric film coating with S-S heterojunction photocatalyst

Transparent TNT and PP films were used for the immobilization of S-S heterojunction ZnO/NdT photocatalyst.

Five hundred milligrams of 30ZnO/NdT photocatalyst were dispersed in 100 mL of pure ethanol. The suspension was vigorously stirred for 20 minutes. TNT and PP films (dimensions: 7.5 cm × 2.4 cm, thickness: 0.01

mm) were then dipped in the suspension for 5 min (TNT/30Zn-NdT and PP/30ZnO-NdTfilms) and dried at room temperature for 24 h (Figure 27).

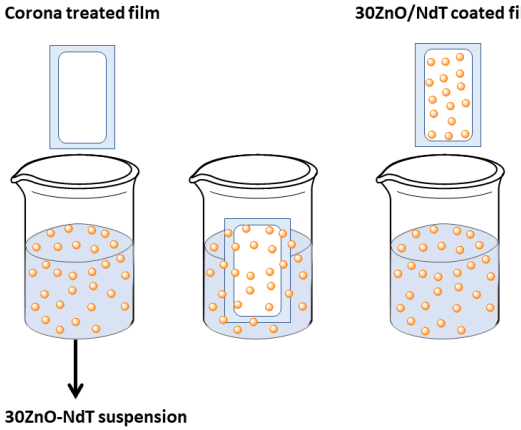

Figure 27. Schematic representation of coating process.

2.4 Samples characterization

2.4.1 Wide angle X-ray diffraction

Wide angle X-ray diffraction (WAXD) is a non-destructive method used for the structural characterization of the crystalline materials.

To verify the structure and actual formation of the synthesised composites, WAXD analyses were performed with an automatic Bruker D8 Advance diffractometer using reflection geometry and Nickel filtered Cu-Kα radiation. The intensities of WAXD patterns were not corrected for polarization and Lorentz factors, to allow easier comparison with most

literature data. The acquisition interval ranging was between 2θ = 5° and 90°, scanning with a step size of 0.0303° and an acquisition time of 0.200 s per point.

2.4.2 Specific surface area

The specific surface area of a photocatalytic system could be a useful parameter for improving photocatalytic performances, since a greater surface area means an increase in the number of active sites accessible in the photoreactor [144].

The specific surface area (SSA) of the samples, evaluated by the Brunauer–Emmett–Teller (BET) method, was obtained by dynamic N_2 adsorption measurements at − 196 °C using a Nova Quantachrome 4200e. The samples were pre-treated at 150 °C for 30 min in He flow.

2.4.2.1 Powder photocatalysts

For the samples xZnO/NdT and xZnO/TiO_2 the surface area was also evaluated. For the ZnO and NdT samples SSA were 6 and 68 m^2/g, respectively. In the xZnO/NdT series, surface areas decrease from 48.5 m^2/g to 35 m^2/g when increasing the content of ZnO from 0.039 g up to 1 g. A similar behaviour was observed for the xZnO/TiO_2 samples (Table 6). The specific surface area decreased with increasing zinc amount of in the composite, reaching values of 36, 28, 26 m^2/g for 15ZnO/TiO_2, 30ZnO/TiO_2 and 50ZnO/TiO_2 respectively. These values are lower than for TiO_2 which has a surface area value of 44 m^2/g most likely due to a greater surface coverage by ZnO particles [145].

Table 6. Summary of characterization results of xZnO/NdT and xZnO/TiO_2 photocatalysts.

Samples	SSA (m2/g)	Band gap (eV)	Crystallite size (nm)	
			NdT	ZnO
NdT	29 68[a]	2.5	16	-
ZnO	6	3.3	-	38.3
xZnO/NdT series				
2.5ZnO/NdT	48.5		-	-
15ZnO/NdT	45.4	-	20	51.3
30ZnO/NdT	35.2	-	21.5	61.1
50ZnO/NdT	36	-	25.7	63.7
TiO_2	44	3.3	17	
xZnO/TiO_2 series				
15ZnO/ TiO_2	36	-	26.6	50.8
30ZnO/ TiO_2	28	-	26.3	50.8
50ZnO/ TiO2	26	-	26.3	50.9
Fe/ZnS				
			Fe	**ZnS**
Fe^0	38		12[b]	-
ZnS	14		-	25[c]
[a] **Fe^0-ZnS**	44		12	25

a NdT treated in isopropanol solution 1 M.

b evaluated by using the FWHM of (110) reflection

c evaluated by using the FWHM of (111) reflection

The characterization results, such as SSA and crystalline size of the Fe^0-ZnS catalysts and sPS/[Fe^0/ZnS] are summarized in Table 6 and compared with the neat powder ZnS and Fe^0.

The SSA of Fe^0-ZnS sample is equal to 44 m^2/g, an increase of its value was observed with respect of bare ZnS (14 m^2/g). This increase of the SSA value could be attributed to the presence of the inter-penetrated zero valent iron network. However, further studies should be carried out to verify this hypothesis.

2.4.2.2 HP-NcAs photocatalytic systems

The values of SSA and porosity of pure sPS aerogels and HP-NcAs are reported in Table 7.

The total porosity of these samples (including macroporosity, mesoporosity and microporosity) can be estimated from the volume-to-mass ratio of the aerogel. Thus, the percentage porosity (%P) of aerogel samples can be expressed as:

$$\%P = 100\,x\,(1 - \frac{\rho_{app}}{\rho_{aerogel}})\quad (1)$$

ρ_{app} is the apparent density obtained from the mass/volume ratio of aerogel samples and $\rho_{aerogel}$ the density of polymer matrix (sPS δ-form) equal to 1.02 g/cm^3 that considers both the sPS amorphous and the nanoporous crystalline phase obtained from X-ray diffraction spectra [118].

For the pure sPS aerogels, a decrease in the SSA value is observed as the aerogel porosity reduces. However, the SSA for sPS aerogels is very high due to the presence of the nanoporous crystalline phase of the polymer [98].

The HP-NcAs 5sPS/NdT and 10sPS/NdT the samples have a surface area of 351 and 300 m^2/g respectively, showing the same behaviour as pure sPS aerogels due to the different porosity (Table 7).

The two samples sPS/ZnO and sPS/[Fe^0/ZnS] present substantially very similar surface areas to 5sPS/NdT with the same porosity.

Table 7. Polymeric sPS aerogels and HP-NcA characteristics: Surface Area (SSA), porosity (P), apparent density (ρ_{app}) and atrazine sorption.

Samples	**SSA** **(m^2/g)**	**P** **(%)**	**ρ_{app}** **(g/cm^3)**	**Atrazine sorption @ 180 min** **(%)**
2sPS	408	98	0.02	32
5sPS	400	90	0.11	26
10sPS	280	84	0.17	23
20sPS	242	70	0.32	21
NdT	30	-	-	-
5sPS/NdT	351	90	0.11	-
10sPS/NdT	300	83	0.17	-
5sPS/ZnO	353	90	0.11	-
sPS/[2.5ZnO/NdT]	278	90	0.11	-
sPS/[30ZnO/NdT]	271	90	0.11	-
sPS/[Fe^0/ZnS]	329	90	0.17	-

2.4.3 UV-Vis diffusive reflectance

UV-Vis Diffusive Reflectance Spectroscopy (UV–Vis DRS) is used to measure the light absorption properties. UV-Vis DRS spectra were obtained using a Perkin-Elmer spectrophotometer Lambda 35 with an 88-sample positioning holder.

In Figure 28 are reported the UV-Vis Diffusive Reflectance (UV-Vis DRS) spectra. As we can see, increasing the amount of ZnO inside the heterojunction changes the ability of the photocatalyst to absorb visible light. In fact, with 2.5% of ZnO a behaviour similar to NdT is observed, while with 30% and 50% the ability to absorb visible light decreases. This may be due to the different characteristics of the catalysts. While NdT absorbs and exerts its photocatalytic action in the visible (area of the spectrum ranging from 400 to 800 nm), ZnO is active in the UV region.

The UV-Vis DR spectra of xZnO/TiO_2 (Figure 28B) present the main absorption edge in the UV region (390 - 400 nm).

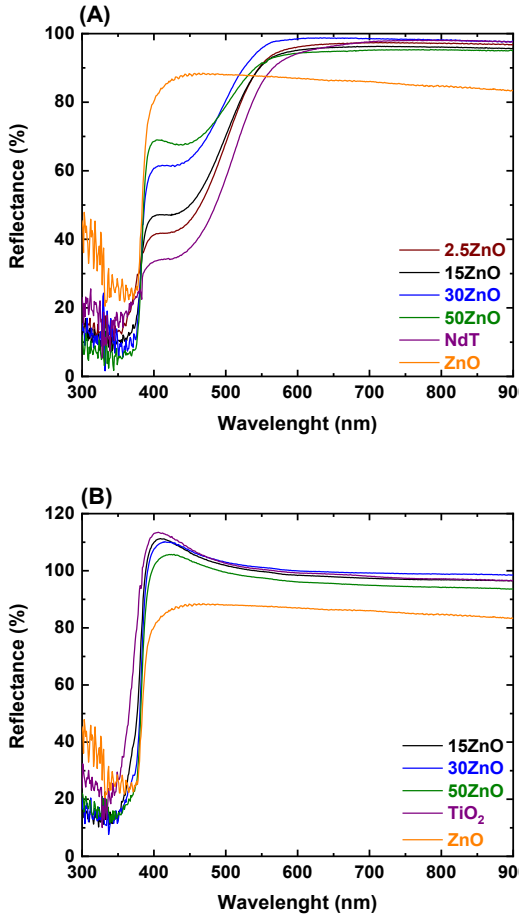

Figure 28. UV–vis diffuse reflectance spectra of xZnO/NdT (A) and xZnO/TiO_2 samples (B).

The UV-Vis DRS of the syndiotactic polystyrene used as matrix is also reported. As it can be seen in Figure 29 in the region between 300 and 600 nm (wavelength able to activate the photocatalysts), the reflectance of sPS is of 100%. This means that the polymer does not absorb electromagnetic

radiation, as it is also reported in the literature [146,147], making it a good support for photocatalytic applications as photocatalysts are activated in that wavelength range.

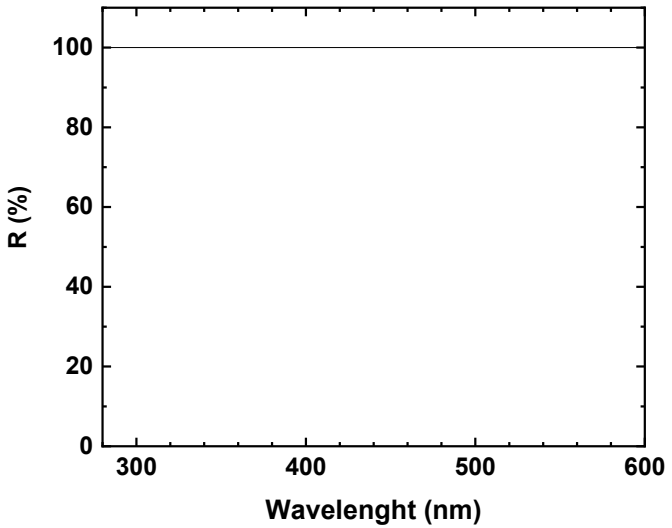

Figure 29. UV–vis diffuse reflectance spectra of sPS polymer matrix.

2.4.4 Photocatalytic reactor for atrazine degradation

The reactor used for the all the tests was a pyrex cylindric photoreactor equipped with an air distributor device (Q_{air} = 150 cm^3/min at room temperature and atmospheric pressure). Solutions were continuously mixed using an external recirculation system operated by a peristaltic pump (Watson – Marlow). According to the designed experiment, the reactor was irradiated by an UV-A LED strip (emission: 365 nm; irradiance 9 W/m^2), a Vis LED strip (emission range: 400–800 nm; irradiance 16 W/m^2) that were wrapped around the external surface of the reactor (Figure 30).

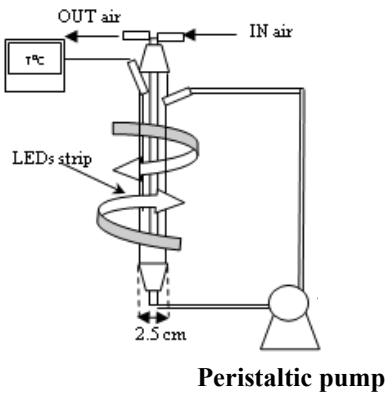

Figure 30. Schematic configuration of the photocatalytic reactor employed for each test.

For the sorption experiment in the pure sPS matrix, 75 mL of ATZ aqueous solution at an initial concentration of 0.1 mg/L were added to the reactor in figure 36 and recirculated for 60 min in absence of illumination and 180 min under irradiation. A few aliquots (2 mL) of solution were collected at different time (10, 20, 30, 60, 120 and 180 min) and assayed for ATZ concentration using HPLC.

For the tests driven by natural sunlight (average irradiance in the range 300 – 600 nm = 37 W/m^2; average irradiance at 365 nm = 1.5 W/m^2) the system was placed outside (Figure 31).

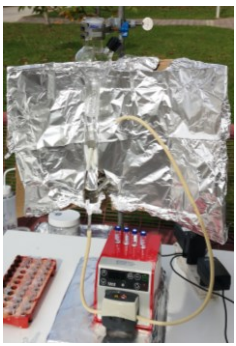

Figure 31. Experimental apparatus used for each photocatalytic test driven by solar light.

All the photocatalytic tests were performed using 75 mL of atrazine aqueous solution (initial concentration 0.1 mg/L) and 300 mg of HP-NcAs composite aerogels.

During each experiment, the system was kept in the dark for 60 min to reach the sorption equilibrium of contaminant inside aerogels and then irradiated for 180 min.

For the photocatalytic experiment under sunlight irradiation the data are reported as a function of the cumulative energy (Q_{light}) per unit of treated volume estimated in the wavelength range 300–600 nm.

$$Q_{light}\left(\frac{kJ}{L}\right) = \sum_{n} light_{n-1}\left(\frac{W}{m^2}\right) \cdot \frac{A_r(m^2)}{V_{total}(L)} \cdot \frac{\Delta t_{n-1(s)}}{1000} \qquad (11)$$

where V_{total} is the total volume treated (L) and A_r is the illuminated reactor surface area (m^2).

2.4.5 Batch and Pilot-scale reactor

The photocatalytic tests with sPS/[Fe^0/ZnS] were performed using a batch reactor device consisting of:

1. a pyrex glass reaction cylinder with a capacity of 280 mL, fitted with a silicone cap with a hole for sampling (Figure 32A).
2. A Heidolph MR 3001 K magnetic stirrer and Teflon-coated magnetic stirring rod to keep the solution in constant agitation, in order to avoid the formation of concentration gradients.
3. UV-A LED strips.

4. A refrigeration system wrapped around the cylinder consisting of a flexible rubber tube through which cold water circulates.

The pilot plant scale reactor used for the experiments is schematized in Figure 32B. It consists of a stainless-steel body with UV-A lamps inside with emission at 365 nm and nominal power of 0.40 W/m^2.

The peristaltic pump and the tank are connected by suitable hoses, with internal and external diameters of 3.6 and 6.4 mm, respectively. Due to the small size of the tube, it was distinguished a real flow rates (measuring the volume dispensed in 1 minute) and nominal flow rates (flow rates read on the pump display) (Table 8).

Table 8. Evaluation of real flow rate.

Nominal flow rate (L/min)	**Real flow rate (mL/min)**
0.3	(40 ± 1)
0.5	(65 ± 1)
1.0	(130 ± 5)
1.5	(210 ± 9)
2.0	(300 ± 4)
3.3	(420 ± 6)

The photocatalytic ATZ and THI degradations experiments were performed using 20 L of aqueous solution (initial concentration 0.1 mg/L), 500 mg of sPS/NdT or sPS/[30ZnO/NdT] composite aerogels and a recirculation flow rate of 2L/min.

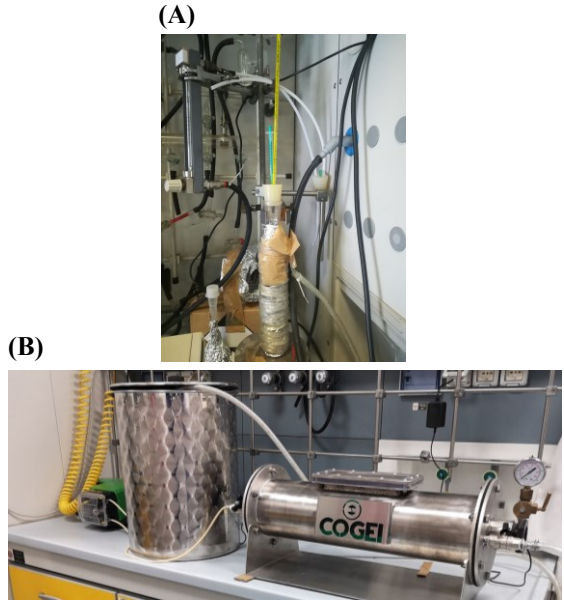

Figure 32. System configuration of the reactor used for PCE photocatalytic degradation: (A) batch reactor; (B) pilot-scale reactor.

2.4.5.1 PCE degradation

All the experimental tests were carried out with the system shown in Figure 38B. A preliminary test was carried out to assess the stability of the system and to test for leaks. A PCE synthetic solution (5 mg/L) was recirculated in the system.

For the photocatalytic tests, a synthetic tetrachloroethylene (PCE) solution with an initial concentration of 500 µg/L were used for the tests and the nominal flow rates of the recirculation pump were varied (1 L/min, 1.5

L/min and 2 L/min) to assess the influence of the latter on the degradation kinetics of PCE.

All tests lasted a total of 80 hours, during which time 1 mL of the treated solution was diluted to a volume of 10 mL in a volumetric flask and then analysed by gas chromatograph.

2.4.6 Analytical determination

2.4.6.1 ATZ and THI determination

HPLC UltiMate 3000 Thermo Scientific system equipped with DAD detector, binary pump, column thermostat and automatic sample injector with 100 µL loop) was used for analysis of atrazine and thiacloprid at 25 °C using a C18 reversed-phase column (Luna 5u, 150 mm × 4.6 mm i.d., pore size 5µm, Phenomenex).

The mobile phase consisted of an acetonitrile/water mixture (70/30 v/v). The flow rate 1 mL/min, injection volume and detection wavelength were, 80 µL and 223 nm for atrazine and 40 µL and 242 nm for thiacloprid, respectively.

Figures 33 and 34 shown the calibration curve and chromatograms of the samples analysed ATZ and THI respectively. The concentrations of ATZ and THI were obtained by interpolation with the least squares with R^2

equal to 0.998 and 0.993. (For ATZ: slope= 12.5 ± 0.4 and intercept= 0.31 ± 0.22; THI: slope= 3.1±0.18 and intercept= 0.11 ± 0.10)

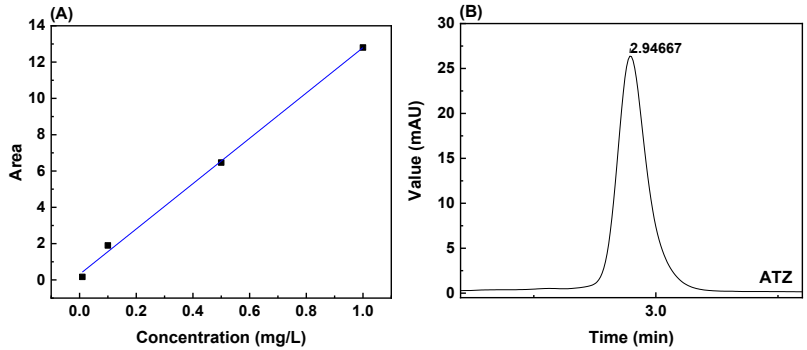

Figure 33. (A) Calibration curve of ATZ in concentration range 1-0.01 mg/L: (B) ATZ chromatogram at concentration of 0.1 mg/L. Retention time: 2.94 min

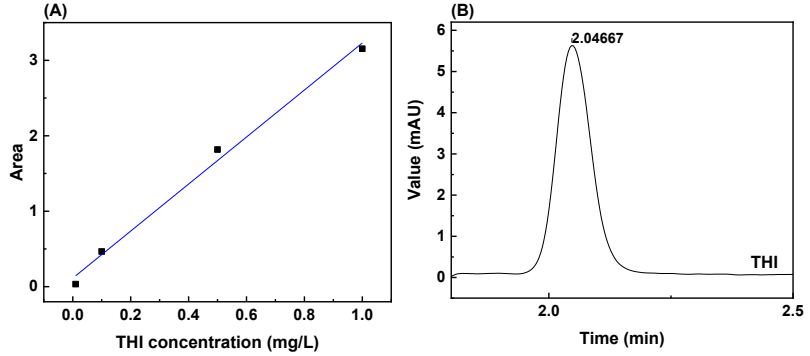

Figure 34. (A) Calibration curve of THI in concentration range 1-0.01 mg/L; (B) THI chromatogram at concentration of 0.1 mg/L. Retention time: 2.04 min

2.4.6.2 PCE determination

Data analysis is carried out using an Agilent 7820A gas-chromatograph equipped with a static headspace (Agilent 7697A), an Agilent HP-5 column (30mx320µmx0.25µm) whose range of use is 60 – 325 °C.

In 20 mL vials, containing 3g of NaCl, 10 mL of the solutions to be analysed, previously diluted by a 1/10 ratio, were introduced into volumetric flasks.

The vials were sealed and vigorously shaken to allow the salt to dissolve.

The samples were then placed in the vial tray where they were automatically moved individually to a thermostatic chamber at a temperature of 80 °C (Oven temperature), where they remained for 20 min (Equilibration time). After this time, the headspace of the vial is pressurised and the sample in gas phase injected into the gas chromatograph whose conditions of use are as follows:

The gas-chromatographic conditions used were as follows:

- Injector temperature: 250°C.
- Temperature programmed: 40°C for 2 minutes, temperature increase of 5°C/min up to 80°C.
- Splitting ratio: 5:1.
- Carrier gas: Helium.
- Detector type: ECD.

- Detector temperature: 350°C.

The external standardisation method was used determined the concentration of PCE in the samples (Figure 35). The calibration curve was obtained plotting the detector response (area of the peak on the chromatogram) vs. PCE standards of known concentration (1, 5, 10, 30 and 50 µg/L). PCE standard solutions were prepared by single dilution of the commercial standard at certified concentration of 1000 mg/L. Sample concentrations were obtained by interpolation with a least squares line (R^2 = 0.999, slope = 1035 ± 24 and intercept = 1311 ± 685).

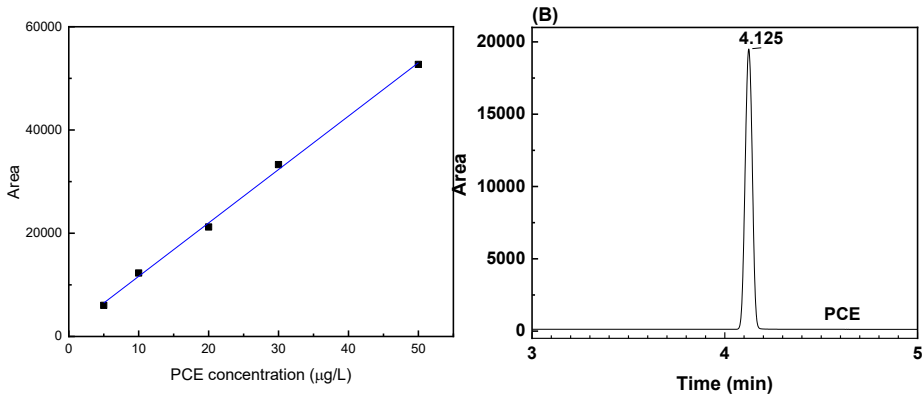

Figure 35. Calibration curve of tetrachloroethylene (PCE) in concentration range 1-50 µg/L. R^2 equal to 0.999. (slope= 1034.5±24 and intercept= 1310.9 ± 685)

2.4.7 Ecotoxicological assays and data analysis

Chronic growth inhibition tests were carried out with the green alga *Raphidocelis subcapitata* according to the ISO 8692 procedure (ISO, 2012a) (Figure 36). Effects on algal growth were assessed by reduction in the number of cells.

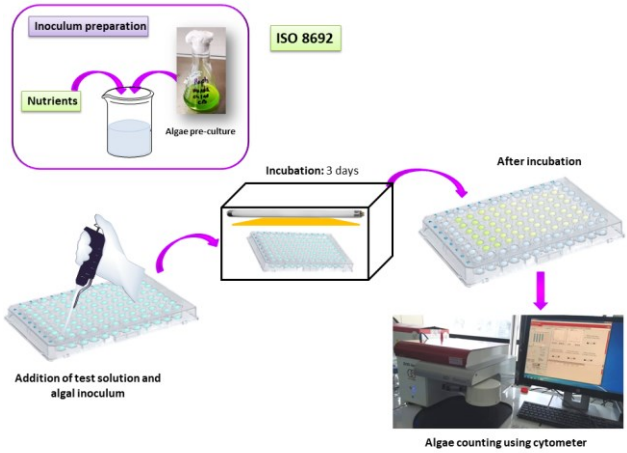

Figure 36. Scheme of toxicity test with *R.subcapitata* according to the ISO 8692 norm.

The sensitivity of the *R. subcapitata* strain to pure ATZ and $ZnSO_4$ (chosen as a reference toxicant) was checked by exposing algae to seven and nine serial dilutions of an $ZnSO_4$ and ATZ, respectively. Serial dilutions were prepared from the corresponding stock solutions following a geometric progression with a factor of two (concentration range for $ZnSO_4$: 7 – 105 µg/L; concentration range for ATZ 3.9 – 250 µg/L, nominal concentrations for ATZ and $ZnSO_4$).

After testing the pure substances, the treated solutions coming from the

photocatalytic tests in presence of UV and Vis light with the different materials (sPS/NdT, sPS/ZnO and xZnO/NdT) were tested for their ecotoxicity.

Each microplate contained a negative control column, in which the algal inoculum in ISO medium was added to millQ water, and a positive control, in which the algal inoculum in ISO medium was added to an ATZ solution of 0.1 mg/L; i.e., the concentration of ATZ used in photocatalytic tests. The other colonies received undiluted effluent solutions to which the algal inoculum in ISO medium was subsequently added.

Effects on algal growth after 72 h (6 replications per sample) were assessed by reduction in the number of cells by cell using a BD Accuri C6 flow cytometer and percentage growth inhibition calculated with respect to negative controls.

Although ATZ is an herbicide and in tests with pure substances showed effects only with microalgae, selected effluents from UV-A and Vis treatments were also tested with the bacterium *Aliivribrio fischeri* and the freshwater crustacean *Daphnia magna* using the corresponding standardised procedures ISO, 2007; ISO 2012b, respectively, as UV-A or Vis treatments may generate degradation products with potential toxic effects on organisms other than the primary producers.

Experiments with *A. fischeri* and *D. magna* were still conducted. In fact, during a photocatalysis process it is possible that the degradation products

formed are more toxic than ATZ, leading to increased ecotoxicity of treated samples toward the test organisms.

In acute bioassay for *Daphnia magna*, living daphnids (Daphnia juveniles aged ≤ 24h) are exposed to the target contaminants and after an incubation time of 24 and 48 hours at room temperature assessing the survival of control organisms. In a chronic test the organisms are exposed for 21 days. The use of microalgae *R. Subcapitata* (ISO 8692) in biological assays is related to their ubiquity and short life cycle. The algae are exposed to the pollutants, and after 3 days, algal numbers are counted to assess the inhibition of the algal growth rate caused by the pollutant or the effluent [125].

The standardized test with a marine gram-negative bacterium *A. Fischeri* follows ISO 1998. Bacteria are exposed to the test samples for a period of 30 minutes and luminescence inhibition (i.e., inhibition of light emission) is measured against a negative control. As luminescence directly proportional to metabolic activity, when bacteria are exposed to certain toxic compounds, the bioluminescence produced by the colony decreases due to the inhibition of enzymatic activity.

For microalgae and bacterium the median inhibition concentration (IC_{50}) (i.e., bacteria and microalgae) and for crustaceans the effect concentration (EC_{50}) and the limit values 95% of confidence for the pure substances were estimated using the REGTOX Excel macro.[148]

The ecotoxic effect was expressed as percentage inhibition or effect compared with a negative control and was determined for algae, bacteria and daphnids exposed to both treated and untreated effluents. Ecotoxicity data data were checked for normality (Shapiro-Wilk test) and homoschedasticity of variance (F test). According to the results, parametric (one-way analysis of variance) or non-parametric (Kruskal-Wallis test) (i.e., if at least one test failed) methods were used to analyse data, also using a Tukey's *post-hoc* pairwise comparison.

Additional experiment was carried out to assess whether ecotoxic effects could result following metal release from NdT and xZnO/NdT catalysts (Table 12). Powder catalysts (30 mg) were added to 75 mL of millQ H_2O and stirred for 180 min. After 180 min the solution was filtered and tested for ecotoxicity.

3 Results and discussion

3.1.1 Characterization

3.1.1.1 Powder photocatalysts

X-ray diffraction patterns (XRD) of xZnO/NdT and xZnO/TiO_2 heterojunction, are shown in Figure 37.

The samples present XRD patterns of both NdT at 2θ = 25.3°and 48° typical of TiO_2 [141] anatase phase and ZnO at 2θ = 31.9°, 34.5° and 36.3° typical of ZnO wurtzite phase [149]. As we can see in Figure 37, as the percentage amount of ZnO increases the intensity of the peaks related to zinc oxide increase.

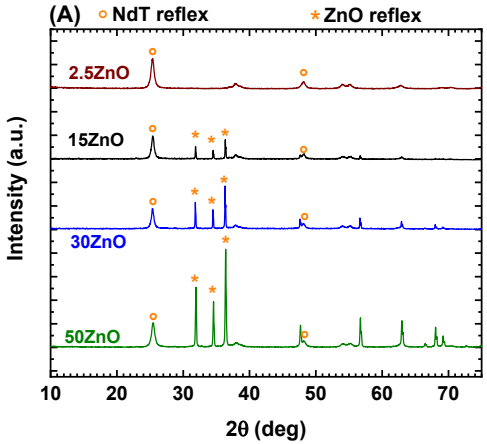

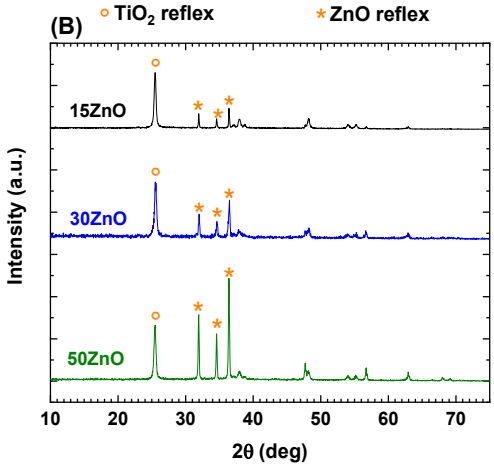

Figure 37. X-ray diffraction patterns of powder catalysts xZnO/TiO_2 (A) and of powder catalysts xZnO/NdT (B).

X-ray diffraction patterns (XRD) of the Fe^0/ZnS composite are reported in Figure 38. The Fe^0 achieved by chemical reduction of Fe^{2+} in liquid phase, displays a pattern at $2\theta = 45°$ c.a. corresponding to the (110) reflection of α-Fe body-centered cubic crystal lattice [150].

The Fe^0/ZnS composite presents the diffraction peaks of ZnS [151] at 2θ = 28.6, 33.2, 47.6 and 56.5° and an additional one at $2\theta = 45°$.

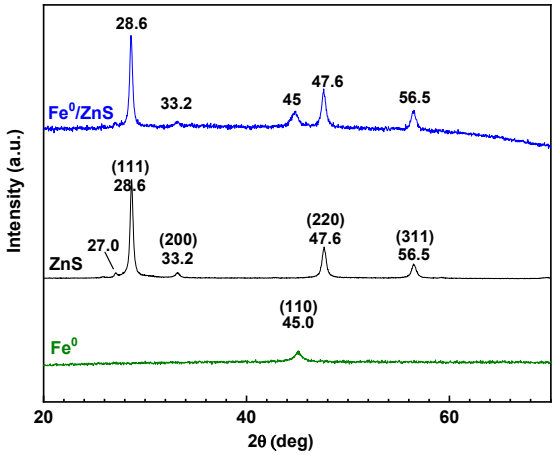

Figure 38. X-ray diffraction patterns of Fe^0, ZnS, and Fe^0/ZnS.

3.1.1.2 HP-NcAs photocatalytic systems

XRD patterns of sPS aerogels (inset) display reflection angles at 2θ = 8.3°, 13.7°, 16.7°, 20.7° and 23.6°, typical of sPS crystalline nanoporous δ-phase [152]. Nanocomposite aerogel 5sPS/NdT and NdT powder samples shows the typical diffraction patterns of the sPS nanoporous δ form in the range of 2θ between 8 to 23° (Figure 39). Instead, in the interval of 2θ higher than 23° the diffraction reflexes typical of the NdT in anatase phase are observed (Sacco et al. 2012).

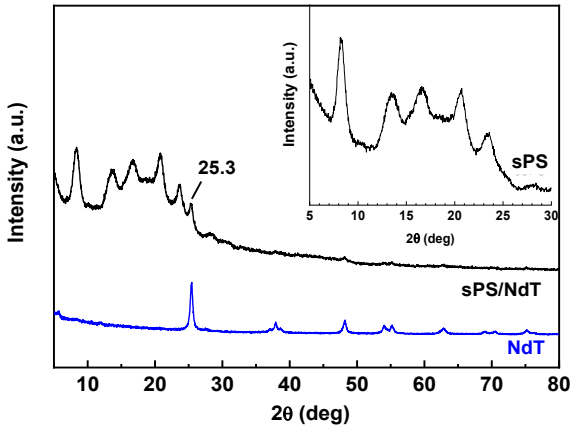

Figure 39. X-ray diffraction patterns: sPS/NdT aerogel, NdT powder and 5sPS aerogel (inset in the graph); a.u. = Arbitrary Unit.

XRD patterns of sPS/ZnO aerogels (Figure 40) display reflection angles at 2θ = 8.3°, 13.7°, 16.7°, 20.7° and 23.6°, typical of sPS crystalline nanoporous δ-phase.[152] Composite aerogel 5sPS/ZnO and 10sPS/ZnO shows the typical diffraction patterns of the sPS nanoporous δ form in the range of 2θ between 8 to 23° (Figure 39) and the principal reflexes of ZnO powder at 2θ = 31.9°, 34.6° and 36.6° typical of the ZnO powder in wurtzite phase.

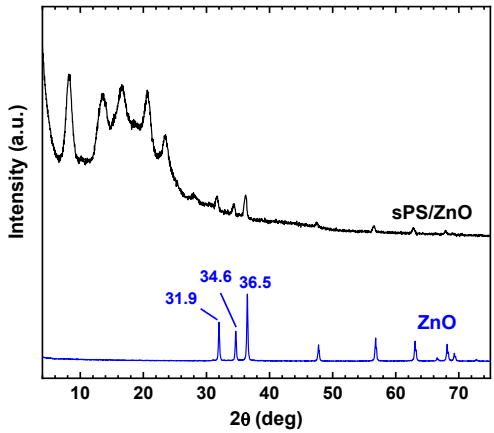

Figure 40. X-ray diffraction patterns: sPS/ZnO aerogel and ZnO powder; a.u. = Arbitrary Unit.

X-ray diffraction patterns of nanocomposite aerogels sPS/[xZnO/NdT] showed in Figure 41. The XRD patterns of the samples sPS/[2.5ZnO/NdT] and sPS/[30ZnO/NdT] evidenced the composite formation. The graph displayed reflection angles of the sPS aerogel in δ form (2θ in the range 8.3 ° - 23.6 °) and the XRD patterns of both NdT (2θ = 25.3 ° and 48 and ZnO (2θ = 31.9°, 34.6° and 36.6°).

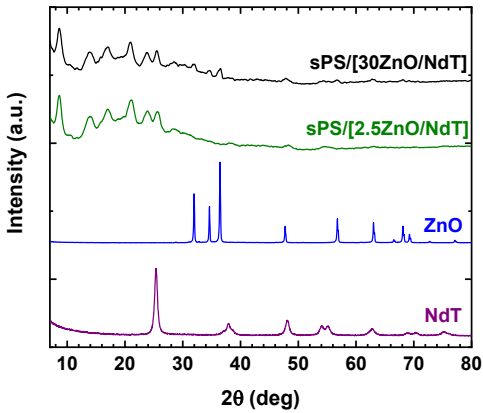

Figure 41. X-ray diffraction patterns of sPS/[xZnO/NdT]; a.u. = Arbitrary Unit.

In Figure 42 are shown the X-ray diffraction patterns of TNT/[30ZnO/NdT] sample presents XRD patterns in 2θ range 20°-30° of the TNT material and NdT at 2θ=25.3°and 48° typical of anatase phase of the TiO_2[98] and ZnO (principal reflexes 2θ= 31.9, 34.5, 36.3°) typical of ZnO wurtzite phase [149].

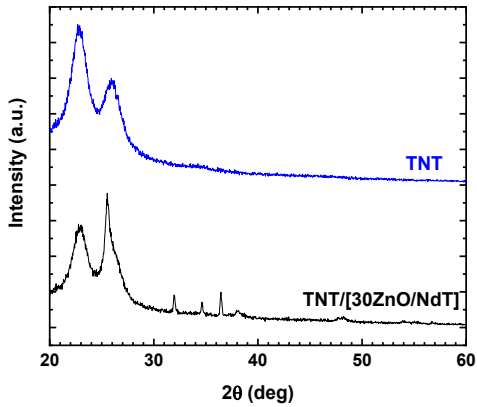

Figure 42. X-ray diffraction patterns of TNT/[30ZnO/NdT] films.

X-ray diffraction patterns (XRD) of the samples sPS/[Fe^0/ZnS] compared with the powder catalysts Fe^0/ZnS are shown in Figure 43.

The Fe^0/ZnS powder sample, presented the XRD diffraction peaks characteristic of Fe^0 alone (2θ = 44.7°) and those related to ZnS (2θ = 28.6°, 47.7°, 56.6°). From the spectrum of the sPS/[Fe^0/ZnS] aerogel, it is possible to recognise the characteristic peaks of sPS aerogel in δ phase [153] (2θ = 8.46°, 13.71°, 16.84°, 20.79°, 23.58°) and the most intense relative peaks for ZnS (2θ = 28.6°, 47.7°, 56.6°). The peak at 2θ = 44.7° for Fe^0 cannot be detected due to the low weight percentage of the catalyst (Fe^0/ZnS) of only 3% in the composite sPS/[Fe^0/ZnS].

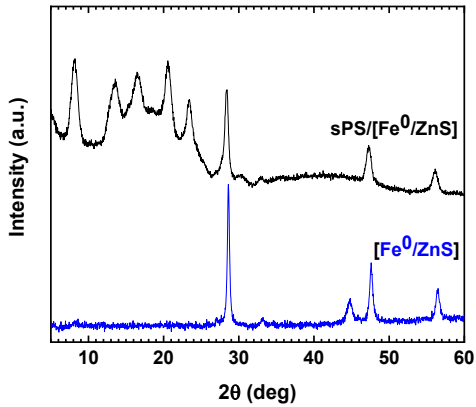

Figure 43. X-ray diffraction patterns of Fe^0-ZnS and sPS/[Fe^0/ZnS] samples.

3.2 Atrazine sorption in sPS aerogel matrix

The best sPS polymer porosity with a maximum of ATZ sorption was determined with a set of experiments where the photocatalytic cylindric reactor (see Figure 29) was filled with pure sPS aerogel with different porosity. The sorption kinetics are shown in Figure 44.

The data show that sorption of ATZ molecules in the cavity of sPS aerogel increase with porosity according to previous studies where sPS aerogel sorption capacity was determined with different organic substances, e.g. 1,2-dichloethane (DCE) for which a sorption capacity of 7 g_{DCE}/100 g_{sPS} was measured after 240 min for an aerogel with a porosity of 85% [154].

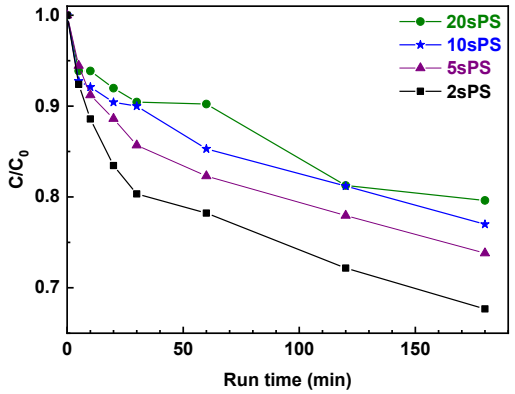

Figure 44. ATZ sorption kinetics for the pure sPS aerogels at different porosity (2sPS, 5sPS, 10sPS and 20sPS). Atrazine initial concentration: 0.1 mg/L.

After 180 min, the ATZ amount absorbed was 32 and 26%, for 2sPS and 5sPS respectively, higher than the sorption of 10sPS and 20sPS samples that have a sorption of 23 and 21%, respectively (Figure 44).

Although the amounts of atrazine absorbed in 2sPS is higher than the other, the 5sPS and 10sPS aerogel were chosen to prepare the HP-NcA, because of the difficulty to fill the photocatalytic reactor when the 2sPS aerogel is used. In fact, as 2sPS aerogel is less dense than 5sPS, a much larger volume of aerogel should have been added in order to keep the amount of aerogel constant (300 mg).

An uptake experiment was also performed for thiacloprid with the pure 5sPS aerogel (Figure 45).

The graph reported the results of THI uptake after 180 min. From the chart, it is possible to observe that the polymer has a capacity to absorb THI, reaching an absorption of 36% after 180 min.

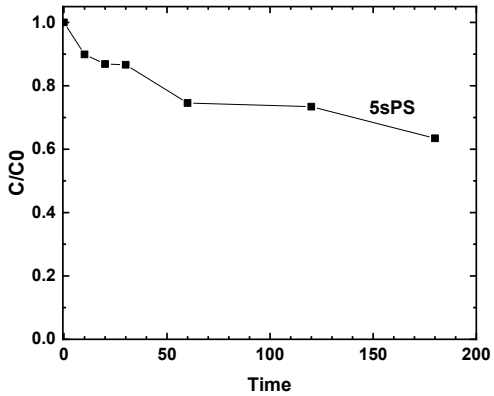

Figure 45. THI sorption kinetics for the pure 5sPS aerogels.THI initial concentration: 0.1 mg/L.

3.3 Activity tests under UV-A and Vis light with HP-NcAs sPS/NdT and sPS/ZnO

Photolytic tests with different LED sources and natural sunlight were performed to verify the stability of ATZ under the irradiation conditions chosen for the photocatalytic tests.

The processes led to 13% and 10% of ATZ degradation after 180 min, using UV-A and VIS irradiation, respectively; while, in the experiment driven by sunlight, ATZ degradation after the same irradiation time was

only 4% (Figure 46). These results confirm ATZ persistency and suggest using stronger reaction conditions to achieve a faster ATZ degradation rate.

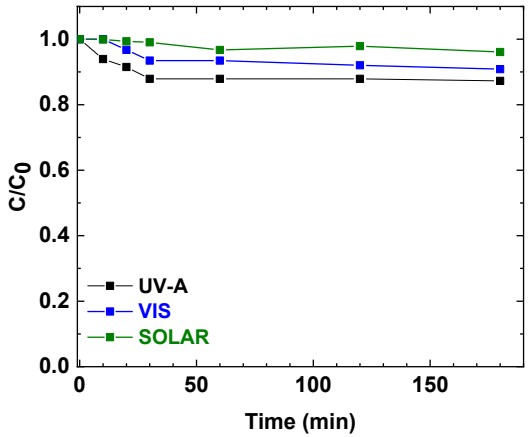

Figure 46. Experiments of photolysis driven by UV-A, Vis LEDs and natural sunlight.

Two HP-NcAs with different porosity (5sPS/NdT and 10sPS/NdT) and the NdT powder were tested in experiments with UV-A light to evaluate their photocatalytic activity towards ATZ. The tests were performed with a dark period of 60 min, during which the adsorption of ATZ in the absence of irradiation was evaluated, followed by a period of 180 min of UV-A irradiation. The results are shown in Figure 47.

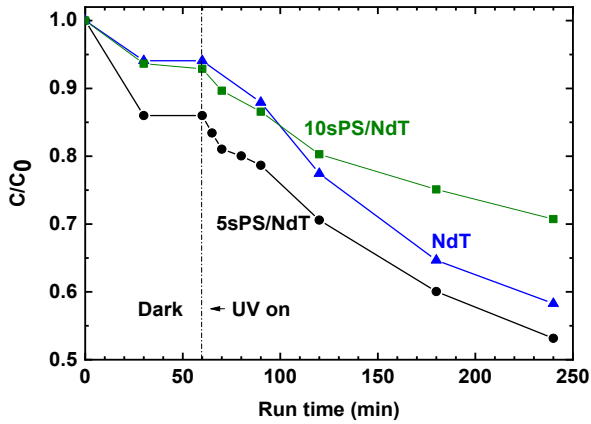

Figure 47. Photocatalytic atrazine degradation with 5sPS/NdT and 10sPS/NdT HP-NcAs, and NdT powder driven by UV-A light. Atrazine initial concentration is 0.1 mg/L.

Different behaviours could be observed. In the dark period, the ATZ removal reached 6% for both the NdT and 10sPS/NdT powders and 13% for 5sPS/NdT aerogel composite. After 180 min of UV-A irradiation, the 5sPS/NdT sample had a higher photocatalytic activity (47%) than both 10sPS/NdT (28%) and NdT powder (41%).

The comparison between the efficiencies of 5sPS/NdT HP-NcA and NdT powder under different irradiation light (UV-A and VIS) are shown in Figure 48. In both experiments, the photocatalytic activity of 5sPS/NdT is higher than NdT catalyst reaching 47% and 25% for 5sPS/NdT composite aerogel (UV-A and VIS, respectively) and 42% and 13% for the NdT (UV-A and VIS, respectively).

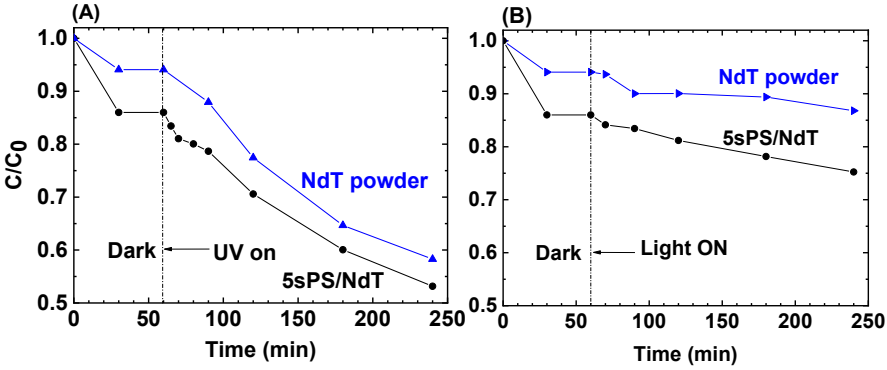

Figure 48. Photocatalytic atrazine degradation with 5sPS/NdT nanocomposite aerogel, and NdT powder: a) UV-A photocatalytic process; b) Vis photocatalytic process. Atrazine initial concentration: 0.1 mg/L.

Despite the similar degradation kinetics similar, 5sPS/NdT HP-NcA is more active than the Nc thanks to its higher sorption towards atrazine molecule.

It has been reported in previous studies that photoactivity is dependent on particle size, i.e. the size of the NdT aggregates in solution formed by the mechanical mixing of the powder [141,155].

Vaiano et al. have in fact shown that dispersion of the catalyst in the polymer matrix can avoid the particle aggregation that normally occurs when powdered catalyst is used, so that smaller particle size remain present in the polymer matrix [100].

The target initial concentration is another parameter to consider during a photocatalytic process. It is known that an increase in initial concentration can lead to a decrease in photocatalytic activity. In fact, as the number of

target molecules increases for a constant the amount of Nc, the generated oxidizing species become insufficient to degrade the target [156]. Thus, it is necessary to assess the influence of the initial atrazine concentration on the degradation kinetics.

Furthermore, the by-products generated during the process can compete with atrazine molecules to occupy the active sites of the catalyst, with a consequent loss of efficiency [157].

The kinetics curves of photocatalytic ATZ degradation driven by UV-A light at different contaminant concentrations (0.1, 1 and 10 mg/L) are reported in Figure 49 for 5sPS/NdT aerogel composite.

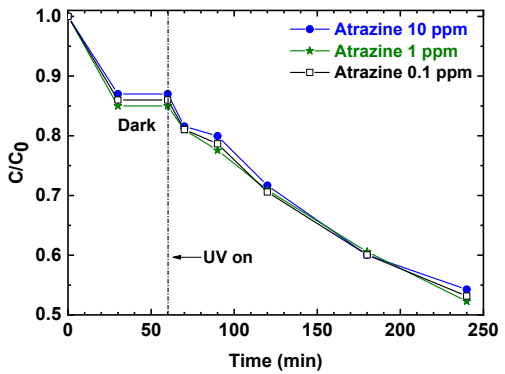

Figure 49. Photocatalytic tests with the aerogel 5sPS/NdT with atrazine solution at different concentration: 0.1 mg/L, 1 mg/L, 10 mg/L.

We can see that atrazine degradation was independent from initial concentration, reaching the same value of 48% after 180 min of photocatalysis.

The presence of the aerogel support probably increases the efficiency and selectivity of the process by preventing the intermediates generated under irradiation from binding to the active sites of the catalyst, thus avoiding their deactivation.

Another test was conducted with the HP-NcA sPS/ZnO. The activity curve is shown in Figure 50. After 60 min in absence of illumination, the same behaviour was observed with atrazine removal reaching 6% for 5sPS/ZnO aerogel composites. The photocatalytic activity of HP-NcAs towards atrazine degradation is very low, leading to a removal 32% after 180 min of irradiation. Instead, the Nc powder reached a 99% of atrazine degradation.

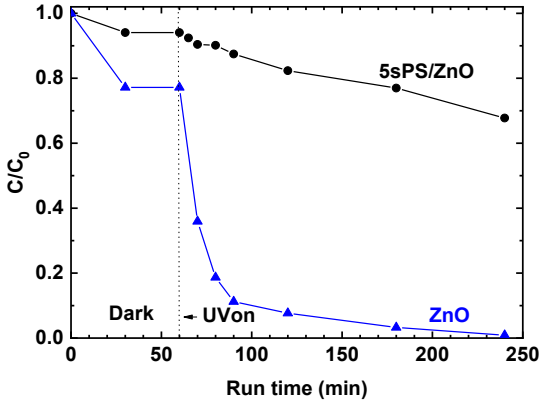

Figure 50. Photocatalytic process under UV irradiation of composites sPS/ZnO samples as a function of time (min).

3.4 Activity tests under UV-A, Vis and solar light of xZnO/NdT and xZnO-TiO_2 photocatalysts

Photocatalytic atrazine degradation under UV-A irradiation was investigated using all the heterojunction prepared in the present study (see section 2.3.2). In Figure 51A, the experimental results evidenced that 30ZnO/NdT and 50ZnO/NdT have higher photoactivity compared with bare NdT (7%) and ZnO (86%), leading to complete atrazine degradation after 30 min of irradiation. On the other hand, by reducing the ZnO amount in the composite from 50 to 15 wt% and 2.5% (15ZnO/NdT and 2.5ZnO/NdT), a lower photocatalytic activity (66% and 19%, respectively), was observed.

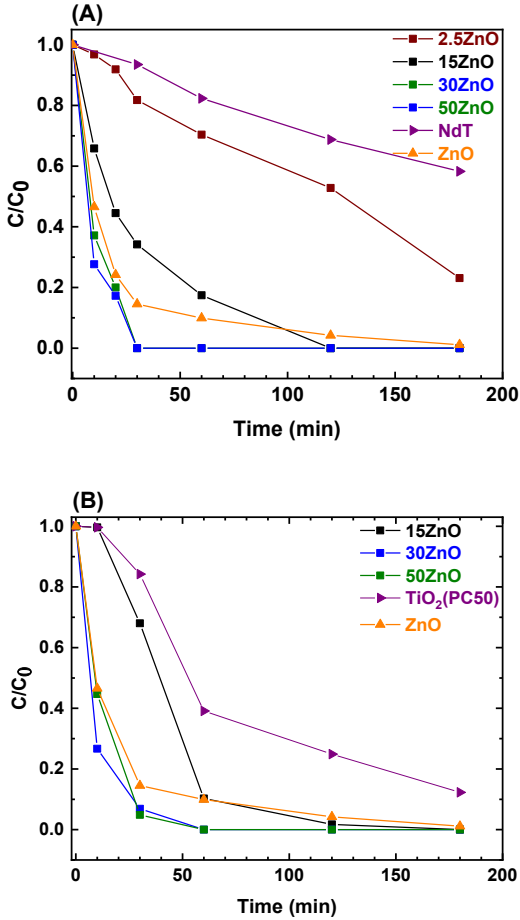

Figure 51. Photocatalytic process driven by UV-A light of A) xZnO/NdT and B) xZnO/TiO_2 samples as a function of UV irradiation time.

Similar results were observed for xZnO/TiO_2 samples (Figure 52B). The behaviour of atrazine relative concentration showed that the xZnO/TiO_2 samples were more active than bare TiO_2 (16%) and ZnO (86%), leading to 94 and 96% of atrazine degradation for 30ZnO/TiO_2 and 50ZnO/TiO_2,

respectively, whereas it was 32% for 15ZnO/NdT, after 30 min of UV-A irradiation.

In Figure 52, the photocatalytic results under VIS irradiation for xZnO/NdT and xZnO/TiO_2 heterojunctions are reported. All the photocatalysts showed a lower photocatalytic activity towards atrazine degradation compared with processes carried out under UV-A irradiation. Only the 15ZnO/NdT heterojunction evidenced a higher performance, degrading 24% after 180 min of VIS irradiation. However, it must be considered that bare NdT was less active than 15ZnO/NdT (Figure 52A).

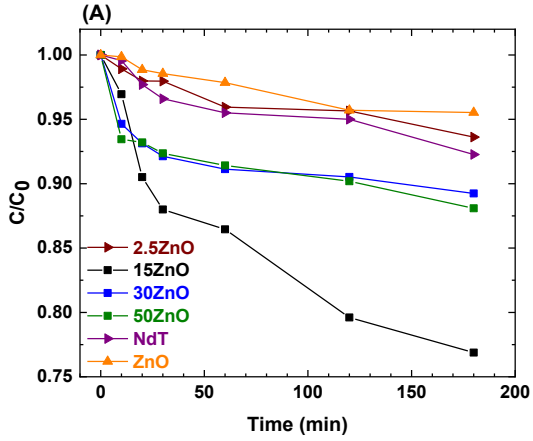

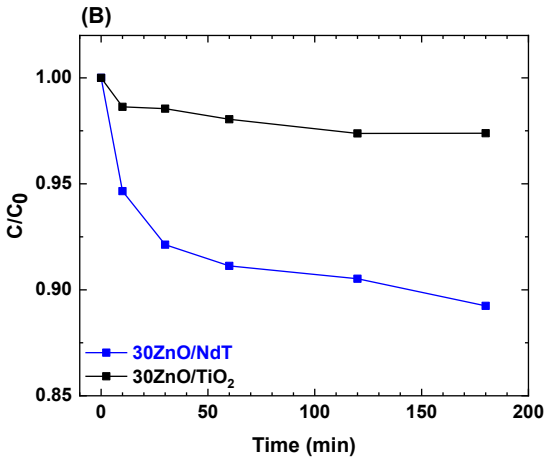

Figure 52. Photocatalytic process driven by visible light of (A) xZnO/NdT samples and (B) comparison between 30ZnO/NdT and 30ZnO/TiO_2 as a function of irradiation time.

In Figure 51B was reported a comparison of the photocatalytic activity of the samples 30ZnO/NdT and 30ZnO/TiO_2 under Vis irradiation.

From the degradation curves, it was observed that the 30ZnO/NdT composite had a higher photocatalytic activity than the 30ZnO/TiO_2. Indeed, after 180 minutes of irradiation, a degradation of 11% was achieved for the former sample compared to only 3% for the composite containing TiO_2. This behaviour is probably due to the presence of NdT, which is able to work better in the visible range.

In the introduction, it was pointed out that the construction of S-S heterojuncted composites could improve photocatalytic performances and also shift the mechanism of action to sunlight-driven processes. For this

reason, the heterojunction photocatalyst 30ZnO/NdT, which exhibits the best photocatalytic activity in processes performed under UV irradiation, was tested in a photocatalytic process driven by natural sunlight. The composite xZnO/NdT showed good photocatalytic activity towards ATZ using solar radiation (Figure 53).

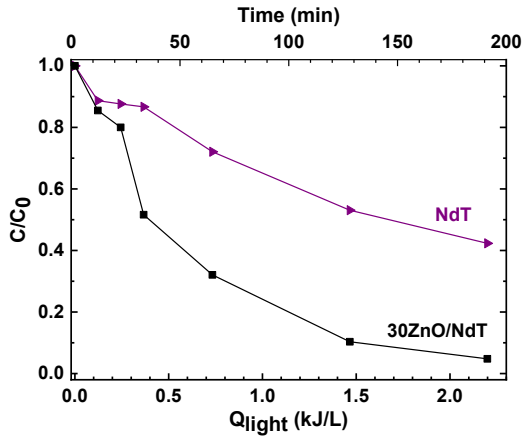

Figure 53. Photocatalytic process driven by natural sunlight of 30ZnO/NdT.

Indeed after 180 minutes of irradiation 96% of the contaminant is degraded unlike bare NdT, which achieved only 58% degradation.

Previously, an improvement in the process under UV had already been observed. The latest result therefore shows that the use of ZnO and NdT for the formation of heterojuncted photocatalysts is a good choice, as the composites showed better performance than individual semiconductors under UV and were also photocatalytically active under solar irradiation.

3.4.1 UV-A, Vis and solar photocatalytic activity with sPS/xZnO-NdT aerogels

Two xZnO/NdT heterojuncted photocatalysts, precisely 30ZnO/NdT and 2.5ZnO-NdT, were dispersed within the sPS matrix to form novel sPS/xZnO-NdT systems. The composites were tested in photocatalytic ATZ degradation under UV and Vis irradiation and the activity compared with the aerogels sPS/NdT and sPS/ZnO previously discussed. Photocatalytic ATZ degradation under UV irradiation is reported in Figure 54. To evaluate ATZ atrazine sorption in absence of irradiation, the tests were carried out in the dark for the first 60 min and irradiated afterwards. Atrazine removal reached 23%, 18%, 14% and 6%, respectively for the composites sPS/[30ZnO/NdT], sPS/[2.5ZnO/NdT], sPS/NdT and sPS/ZnO after 60 min of dark. The photocatalytic results evidenced that the composite sPS/[30ZnO/NdT] had higher photocatalytic activity compared with the other aerogels. Indeed, after 180 min of irradiation 77% of ATZ is degraded, unlike the aerogels sPS/[2.5ZnO/NdT], sPS/NdT and sPS/ZnO with a lower photocatalytic activity.

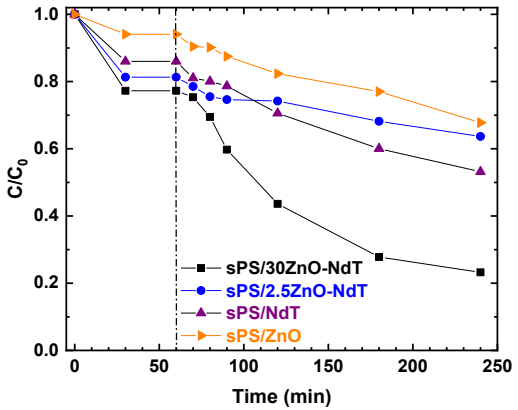

Figure 54. Photocatalytic process under UV irradiation of composites sPS/xZnO-NdT, sPS/NdT and sPS/ZnO samples as a function of run time (min).

On the other hand, for the photocatalytic process under VIS irradiation (Figure 55), the composites sPS/[30ZnO/NdT], sPS/[2.5ZnO/NdT] and sPS/NdT exhibit the same behaviour of the UV one during the dark period, but lower photocatalytic activities during the irradiation period leading to 26%, 28% and 25% atrazine degradation, respectively.

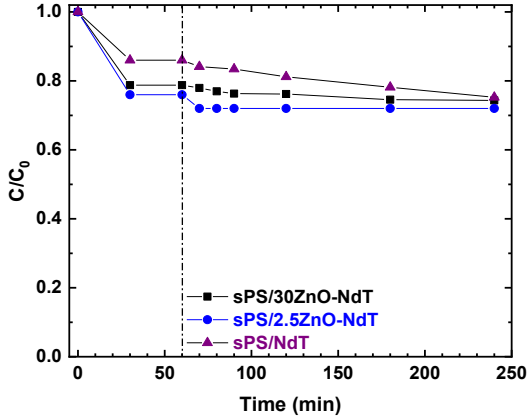

Figure 55. Photocatalytic process under Vis irradiation of composites sPS-xZnO/NdT and sPS-NdT samples as a function of run time (min).

The result obtained reproduced exactly the performances of powder catalysts. The samples sPS/[2.5ZnO/NdT], sPS/[30ZnO/NdT] and sPS/NdT were also tested in photocatalytic ATZ degradation driven by natural sunlight (Figure 56). The results are reported as a function of cumulative energy (Q_{light}) per liter of treated water, calculated according to the Equation 1 (parapraph 2.2.4). From the activity curves of the three different aerogels, it was observed that they were not very efficient towards atrazine degradation. In fact, after 180 min of irradiation only 14%, 11% and 10% of atrazine was degraded.

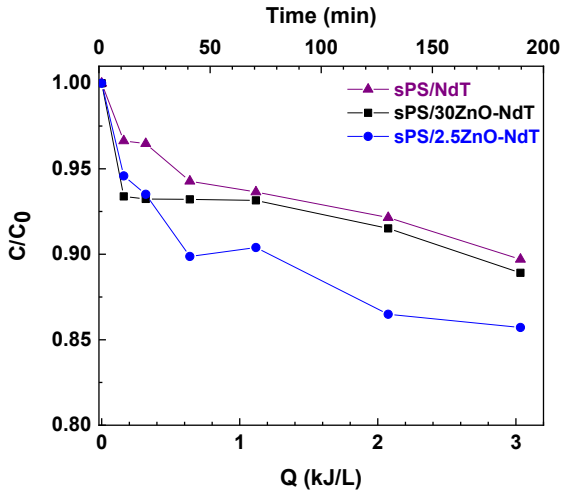

Figure 56. Photocatalytic tests driven by natural sunlight of nanocomposite aerogels as a function of cumulative energy (Q_{light}) per liter of treated water (bottom axe) calculated in the wavelength range 300-600 nm and irradiation time in minutes (min)

Adishkumar et al. evaluated the influence of radiation intensity on photocatalytic activity for phenol degradation in one of their work. They showed that as the intensity of radiation (W/m^2) diminished the percentage of phenol degradation decreased. Higher light intensity could generate the hydroxyl radicals faster, leading to higher phenol degradation (Adishkumar et al. 2014).

The radiation intensity in UV region emission 365 nm was measured and compared with the intensity of UV-A LEDs emitting at the same wavelength. In the case of sunlight, the radiation intensity is 1.5 W/m^2, i.e. about 1/4 that of the UV-A LEDs equal to 9 W/m^2. Most likely the

intensity of solar radiation in the emission region of 365 nm is not powerful enough to quickly generate hydroxyl radicals and efficiently irradiate the entire photocatalytic system, decreasing the number of active sites of the composite aerogels.

3.4.2 Solar photocatalytic activity with TNT and PP films

The 30ZnO/NdT photocatalyst was immobilized on commercial TNT and PP TNT/[30ZnO/NdT] and PP/30ZnO-NdT films were prepared as described in paragraph 2.3.5 and tested in the solar treatment (Figure 57). The graph shows a comparison of the degradation processes of the composite materials, viz. sPS/[30ZnO/NdT] aerogel, TNT/[30ZnO/NdT] and PP/[30ZnO/NdT] films. The results evidenced that the photocatalytic activity of the polymeric films is higher than sPS/[30ZnO/NdT] aerogel leading to atrazine degradation of 74% and 40% for TNT/[30ZnO/NdT] and PP/30ZnO-NdT samples, respectively.

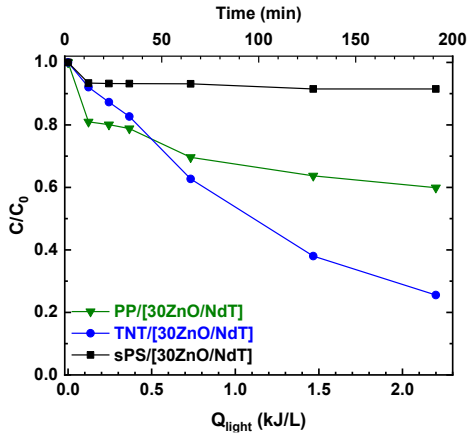

Figure 57. Photocatalytic process driven by natural sunlight: compare of PP/[30ZnO/NdT], TNT/[30ZnO/NdT] films and sPS/[30ZnO/NdT] aerogel as a function of cumulative energy.

The results in the case of the TNT film are interesting although the atrazine removal is lower than the powder catalyst that reached 96% of degradation. In fact, lower activity is attributable to the fixing of the catalyst on the polymer film, as it is reported in the literature that dispersion can affect the activity.

3.5 Ecotoxicity results

The sensitivity of the algal cell culture was periodically checked against the reference toxicant $ZnSO_4$ (concentration range: 7–105 µg/L) and the results shown in Table 9.

The EC_{50} determined for pure atrazine toward the green alga *R. subcapitata* (Table 9) was 40 ± 6 µg/L (n = 3), in agreement with previous literature results (23 µg/L, no confidence interval reported) [159,160]. *A. fischeri* and *D. magna* are not sensitive to 0.1 mg/L of ATZ. The EC_{50} values ATZ reported in the literature range from 35.4 to 70.0 mg/L for *A. fischeri* [161,162] and from 47.8 to 53.1 mg/L for *D. magna* [163].

Table 9. Sensitivity evaluation of the algal cell culture of the alga R. subcapitata against the reference toxicant $ZnSO_4$ and pure atrazine according to the ISO 8692 norm.

Controls	**EC_{50} (µg/L)**	**95% CI EC_{50}**	**EC_{10} (µg/L)**	**[Initial inoculum] (cell/mL)**	**Growth rate (day^{-1})**	**pH change (units)**	**Variation coefficient of growth rates**
Atrazine							
Test 1	39	32.5-44.2	8.9	16700	1.7	0.59	1.8%
Test 2	45	41.4-49.7	20.5	16560	1.5	1.1	2.4%
Test 3	38	37.1-42.1	8.9	18600	1.6	0.17	1.8%
Test 3	49	9.42-66	16	18600	1.6	0.17	1.8%
$ZnSO_4$							
Test 1	66	61.9-71.8	54	17400	1.6	-	4.2%
Test 2	28	26.9-31	8.1	16700	1.8	0.64	1.6%
Test 3	37	29.5-34.1	13.7	16200	1.6	0.17	1.8%
Test 4	16	31.9-41.7	10	18600	1.5	0.73	1.2%
Test 5	30	14.7-18.6	5.4	18900	1.6	0.87	4.4%
Test 6	31	20.6-36.4	15	17300	1.5	0.81	1.6%
Test 7	53	51-56	24	17300	1.6	0.93	0.95%

Table 10. Atrazine and $ZnSO_4$ real concentration values for *R. subcapitata* control experiments.

Test	[C1] µg/L	[C2] µg/L	[C3] µg/L	[C4] µg/L	[C5] µg/L	[C6] µg/L	[C7] µg/L	[C8] µg/L	[C9] µg/L
Atrazine									
1	0	N.D	10	32	78	170	332	640	1290
2	0	N.D	10	45	71	-	-	660	1370
$ZnSO_4$									
1	8	9	13	17	24	34	48	68	96
2	8,9	13	19	29	47	64	90	123	-
3	11	14	17	24	31	40	53	75	102

3.5.1 Samples toxicity derived from UV and Vis treatment with HP-NcA sPS/NdT

The toxicity of the samples derived after 72 h of photocatalytic treatment driven by UV-A and VIS light with the sPS/NdT aerogel was assessed.

The validity of all tests was verified according to criteria specified in the norm ISO 8692, such as growth rate: ≥ 1.4 days-1 (corresponding to an increase in cell concentration by a factor of 67 over 72), coefficient of variation of growth rate in control replicates: ≤ 5% and pH change: < 1.5 units, which are respected for all tests carried out (Table 11).

Table 11. Ecotoxicity test on *R. subcapitata* according to the European standard EN ISO 8692.

Plate number	**Controls**	[Initial inoculum] (cell/mL)	Growth rate (day^{-1})	pH change (units)	Relative standard deviation of growth rate in control wells (%)	Positive control %Inhibition
	Process driven by UV light					
1	**Test UV1**	17060	1.6	0.42	0.88%	66.5
1	**Test UV2**	17060	1.6	0.42	0.88%	66.5
1	**Test UV3**	17060	1.6	0.42	0.88%	66.5
2	**Test UV4**	19100	1.5	1	0.8%	78
3	**Test UV5**	16200	1.7	0.59	1.8 %	77
	Process driven by visible light					
1	**Test Vis1**	17060	1.5	0.66	1%	72
1	**Test Vis2**	17060	1.5	0.66	1%	72
1	**Test Vis3**	17060	1.5	0.66	1%	72
2	**Test Vis4**	19100	1.5	1	0.4%	78
3	**Test Vis5**	16200	1.5	1	0.4 %	77

The effluent obtained after 72 h of VIS treatment showed a very high level of toxicity to microalgae with a total growth inhibition (99% ±0.2%) and a clear detectable effect on the survival of *D. magna* (58%±0.2%) of mortality (Table 12).

Table 12. Atrazine treated samples (90% v/v) (whole sample exposure) considering both visible (VIS) and ultraviolet (UV) treatments after 72 h of irradiation. Data were expressed as percentage of effect (%) after incubation of 72 h for *R.subcapitata*, 24 h for *D. magna* and 30 min for *A. fischeri*.

	A. fischeri (30 min)	*R. subcapitata*	*D. magna* (24 h)
Vis	Non toxic	99.0 ± 0.2%	58.3 ± 0.2%
UV	Non toxic	6.4 ± 2.1%	Non toxic

Conversely, the effluent after 72h of UV-A treatment was non-toxic to *D. magna* and had a much lower effect (6.4%) on the growth of *R. subcapitata*. This means that UV-A photocatalytic process is more effective than the VIS one about removal of both ATZ and its degradation by-products, with reduction of effluent ecotoxicity.

In Figure 65, the toxicity trend after 0.5, 1, 3, 24 and 72 h for both VIS and UV-A treatments for the three testing species and the atrazine removal rates were reported. After 72 h UV-A treatment, the toxicity removal is clear for all sensitive testing species even though ATZ was not completely removed (up to approximately 80%). The positive controls performed during different tests with 0.1 mg/L of atrazine, always showed a 70% inhibition effect (see Table 15), confirming that the trends reflect real changes in sample ecotoxicity to *R. subcapitata* rather than shifts in algal sensitivity during different tests.

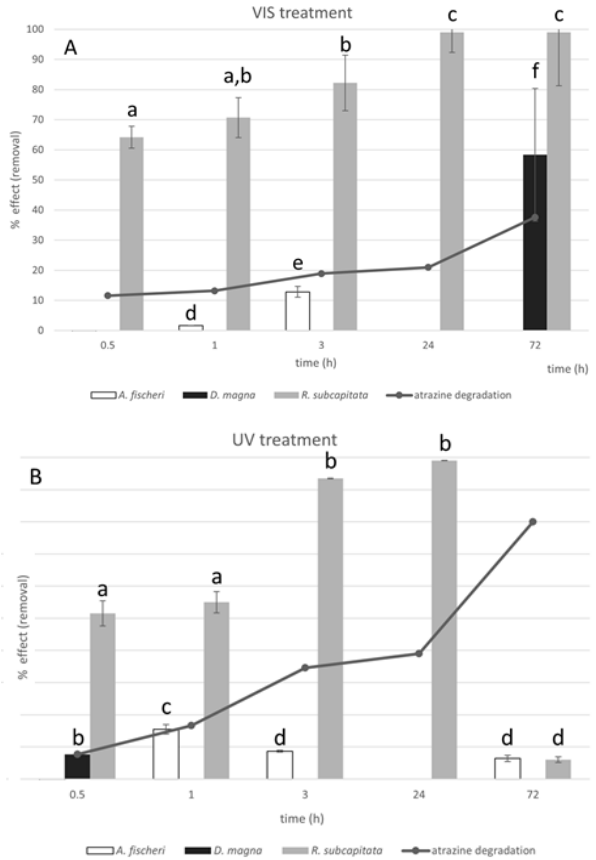

Figure 58. Effect of solutions initially amended with 100 µg/L of atrazine- after visible (Vis) (A) and ultra-violet (UV) (B) treatment towards *A. fischeri*, *D. magna* and *R. subcapitata* following atrazine removal between 0.5-72 h. Different letters (a–f) indicate statistically significant differences in sample ecotoxicity (Tukey's test, $p < 0.05$). Missing bars in the graph correspond to non-tested samples.

It is noteworthy that the ecotoxicity increased from 0.5 to 24 h for both Vis and UV-A treatments. The formation of degradation by-products more toxic than atrazine most likely contributed to the observed increase in the ecotoxicity of the effluents. In the UV-A photocatalytic process, longer reaction times (i.e., 72 h) apparently allowed for an almost complete degradation of the toxic by-products and a consequent decrease in ecotoxicity. Furthermore, effluents obtained after a VIS process were also toxic to the non-target organisms *D. magna*, despite the initial atrazine concentration being three orders of magnitude lower than acute LC50 reported in the Envirotox Database. These results confirm the need to systematically combine the development of AOPs with an ecotoxicological evaluation.

3.5.2 Samples toxicity derived from UV treatment with HP-NcA sPS/ZnO

For the samples 5sPS/ZnO were carried out photocatalytic ATZ degradation experiments under UV-A treatment at different treatments time (30, 60 and 180 min) to assess the ecotoxicity for *R. subcapitata* on the post treated samples. The results were shown in Table 13.

Table 13. Atrazine treated samples (90% v/v) (whole sample exposure) considering treatment under UV-A irradiation at different run time (30, 60 and 180 min) and in H_2O milliQ after 180 min. Data were expressed as percentage of effect (%) after incubation of 72h for *R. subcapitata*.

Sample	**Controls**	% Inhibition	%Inhibition Positive control
Treatment under UV light			
5sPS/ZnO	Test UV 30 min	77	65
5sPS/ZnO	Test UV 60 min	68	65
5sPS/ZnO	Test UV 180 min	59	65
Treatment in H_2O millQ			
5sPS/ZnO	H_2O millQ 180 min	66	65

For the different tests was observed a different percentage inhibition on total growth. In fact, after the first 30 min of UV-A irradiation, a percentage inhibition of 77% was observed. On the other hand, after 60 and 180 min of treatment the toxicity of the solution decreases reaching values of 68% and 59% respectively.

3.5.3 Samples toxicity derived from UV and Vis treatment with xZnO/NdT photocatalysts

The ecotoxicity of solutions obtained from UV-A and Vis treatment of atrazine solution with the heterojuncted photocatalysts 15ZnO/NdT and 30ZnO/NdT was also assessed. By the results shown in Table 14 the validity of the tests was confirmed.

Table 14. Ecotoxicity test on *R. subcapitata* according to the ISO 8692 norm.

Plate number	**Controls**	[Initial inoculum] (cell/mL)	Growth rate (day^{-1})	pH change (units)	Relative standard deviation of growth rate in control wells (%)	Positive control %Inhibition
	Process driven by UV light					
1	**Test UV1**	18100	1.5	1.04	1.91%	76
1	**Test UV2**	18100	1.5	0.99	0.24%	77
	Process driven by visible light					
1	**Test Vis1**	18100	1.5	1	0.46%	79
2	**Test Vis2**	18600	1.5	0.83	0.43%	79

The tests showed a very high levels of toxicity for microalgae with an almost total growth inhibition of 98% and 99% for the sample 15ZnO/NdT and 30ZnO/NdT respectively, even if in the case for the UV-

driven photocatalytic process a complete ATZ degradation was obtained after 180 min. Analysis of zinc revealed the presence of high concentrations of this element in the solutions used for ecotoxicity testing, with levels ranging from 559 µg/L for UV treatment to 4576 for photocatalysts immerged in milliQ water for 3 hours (Table 16). These Zn concentrations are very toxic to *R. subcapitata.*[164]

Table 15. Atrazine treated samples (90% v/v) (whole sample exposure) considering treatment under UV irradiation and Vis irradiation and in milliQ water after 180 min for both samples 15ZnO/NdT and 30ZnO/NdT. Data were expressed as percentage of effect (%) after incubation of 72h for *R. subcapitata.* Zn concentration in samples were determined by flame atomic absorption spectroscopy (FAAS).

Samples	**Controls**	% Iinhibition	%Inhibition Positive control	Zn^{2+} dissolved (µg/L)
Treatment under UV light				
15ZnO/NdT	Test UV	98	76	559
30ZnO/NdT	Test UV	99	77	667
Treatment under Vis light				
15ZnO/NdT	Test Vis	98	79	541
30ZnO/NdT	Test Vis	99	79	1000
Treatment in H_2O millQ				
15ZnO/NdT	Test H_2O millQ	98	82	3427
30ZnO/NdT	Test H_2O millQ	99	82	4576

In section 1.2.2, it has been pointed out the disadvantages of heterogeneous photocatalysis, in particular the possible metals release from powdered catalysts into water and wastewater and the associated environmental consequences. For this reason, the alternative could be to fix the catalyst in a matrix.

Release experiment were carried out for assess the compatibility of the powder samples xZnO/NdT (Table 15) and the HP-NcAs (Table 16).

It is well known in literature that aquatic organisms are sensitive towards Zn. Franklin et al. reported that for *R. subcapitata* the IC_{50} of algal growth rate is about 60 µg Zn/L[164].

sPS/NdT and sPS/ZnO HP-NcAs samples were also tested for metal release by placing 300 mg of sample in 75 mL of MillQ H_2O. The solution was stirred for 180 minutes and the experiment performed (Table 16).

Table 16. Toxicity release experiment of HP-NcAs 5sPS/NdT and 5sPS/ZnO samples in H_2O MilliQ. Zn concentrazion in the samples determinated by Atomic Absorption Spectroscopy (AAS).

Samples	**Controls**	% Inhibition	%Inhibition Positive control	Zn^{2+} dissolved (µg/L)
Treatment in H_2O millQ				
5sPS/NdT	Test H_2O millQ	12	70	-
5sPS/ZnO	Test H_2O millQ	30	68	50

From the results discussed above, it has been shown that the release of the metal by the catalyst in water can generate final solutions more toxic than the starting one (99%) despite there is a good degradation of the contaminants. However, by immobilising the catalyst in the aerogel, a reduction in toxicity from 99% to 30% was observed.

3.6 sPS/[Fe^0/ZnS] aerogel

It is reported in the literature that Fe^0-based compounds can degrade halogenated compounds such as PCE. More specifically, when Fe^0 is penetrated by groundwater containing halogenated compounds, an electrochemical corrosion phenomenon develops (Johnson et al. 1996). The mechanism leading to the degradation of a generic organic halide in presence of Fe^0 involves an oxidation-reduction reaction. On the metal surface (anodic portion), electrons are released, and a soluble cation (Fe^{2+}) is formed.

For this reason, a photocatalytic sPS/[Fe^0/ZnS] aerogel was prepared and tested for PCE degradation using batch and pilot-plant scale reactors.

Two tests were carried out in the batch reactor. A photolytic test (test performed by irradiating the PCE solution without the photocatalyst) to test the solution stability over time and a photocatalytic analysis to test the activity of the aerogel sPS/[Fe^0/ZnS].

The experimental results of the test performed with a solution of initial concentration of PCE 5ppm are shown in Figure 59. In the graph, it is evident that PCE degradation occurred whether irradiated by UV light alone or in the presence of light and photocatalyst. In fact, after 180 minutes a degradation of 45% and 84% was observed, respectively. It should also be noted that due to the simultaneous presence of UV radiation and the sPS/[Fe^0/ZnS] sample, a constant concentration level was not achieved over time and PCE degradation continues to progressively decrease until almost complete removal of the contaminant is achieved after 180 minutes.

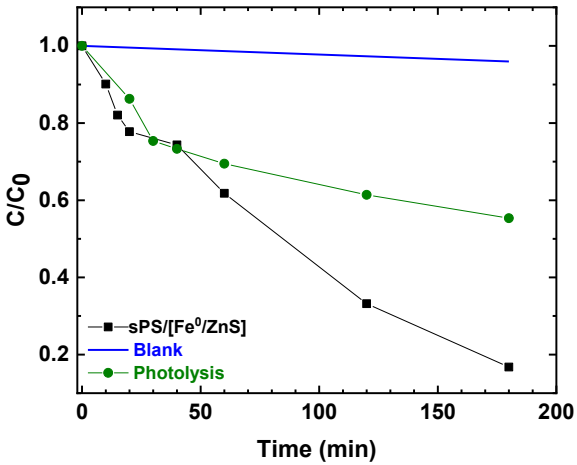

Figure 59. Photolytic and photocatalytic test with sPS/[Fe^0/ZnS] composite aerogel for PCE (initial concentration 5ppm) degradation. LEDs UV-A emission 365 nm using batch reactor.

Photocatalytic tests were then carried out with the pilot-scale reactor. Due to the high volatility of the PCE, a 12-day system stability test was carried out before the photocatalysis tests. A solution of PCE at a concentration of 5 mg/L or ppm was recirculated for 12 days at a nominal flow rate of 1L/min (Figure 60).

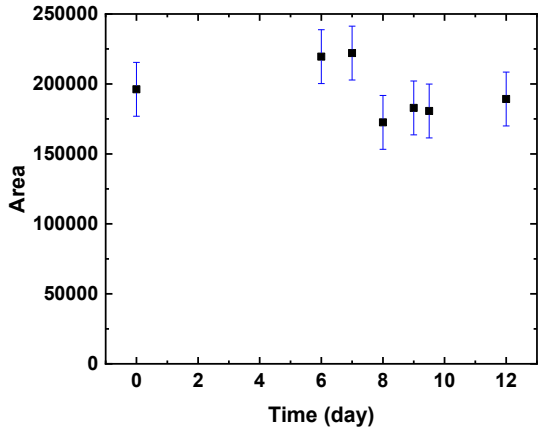

Figure 60. System stability test. PCE solution 5 mg/L recirculated in the pilot-scale reactor for 12 days.

The graph showed the area of the peak on the chromatogram as a function of the test time in days and error bars represent. Error bars in the graphs represent ± 1standard deviation (n=3). After 12 days, no loss of PCE was observed from the system, as it was not observed any substantial change in the peak area value.

Once the correct operation of the reactor was established, 9.75 g of the previously synthesised sPS/[Fe^0/ZnS] nanocomposite aerogel was added to the reactor to perform the photocatalytic tests.

After 80 hours, the kinetics of PCE degradation was not significantly affected by the recirculation flow rate and the PCE degradation rate reached 95% (Figure 61A).

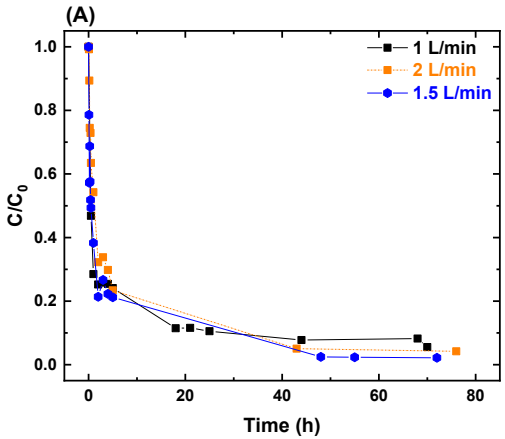

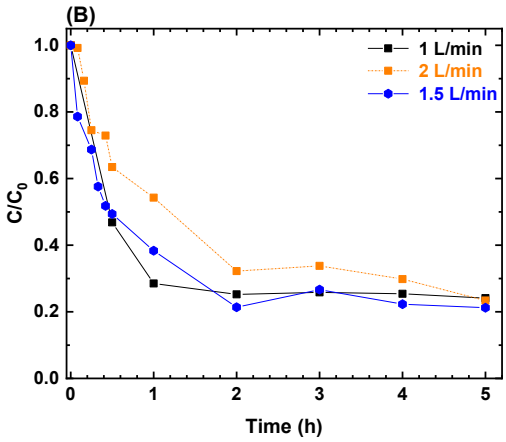

Figure 61. Photocatalytic PCE degradation with the sPS/[Fe0/ZnS] : (A) Comparison at different recirculation pump flow rate (1, 1.5 and 2 L/min nominal flow rate). (B) Photocatalytic activity of the first 5 hours of the process

Considering the kinetics of degradation in the first five hours (Figure 61B) of the process it is possible to better appreciate the result. Afterwards, a degradation of 80% was observed in all cases analysed. It can therefore be deduced that the photocatalytic activity is independent of the recirculation flow rate.

In the subsequent tests, however, the influence of the air flow rate on the kinetics was evaluated, with the recirculation rate remaining unchanged.

It is known in photocatalysis that the reaction kinetics can be influenced by the air flow, as this serves to generate the radical species that oxidise organic compounds.

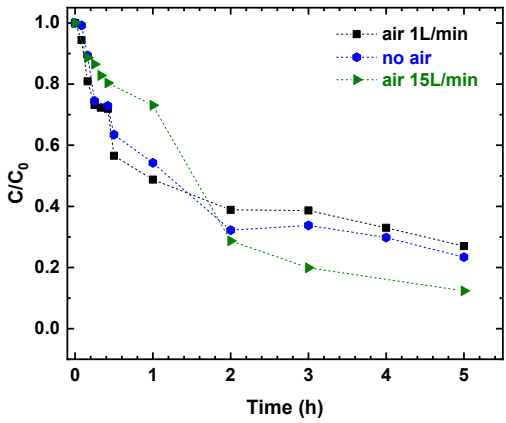

Figure 62. Photocatalytic PCE degradation with recirculation flow rate 2L/min: without air; with air 1L/min and 15 L/min air blown into the tank.

Therefore, while maintaining a nominal recirculation flow rate of 2 L/min, the air flow rate inside the reactor was varied. Two tests were performed, at an 1L/min and 15 L/min air flow rate. From the kinetic curves in Figure 62, it was observed that the test conducted without air and with an air flow rate of 1L/min were comparable, leading to approximately 70% PCE degradation after 5 hours. On the other hand, switching to an air flow rate of 15 L/min the degradation kinetics was improved. In fact, 90% of PCE was degraded after 5 hours.

However, as PCE is a very volatile compound and no substantial differences were observed, it was preferred to carry out the other tests without using air.

The influence of the initial PCE concentration on degradation kinetics was also investigated (Figure 63). Four photocatalytic tests were conducted under the same experimental conditions (recirculation flow rate of 2L/min; no blown air).

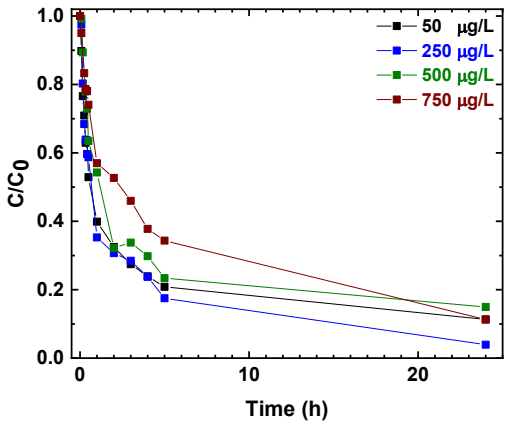

Figure 63. Photocatalytic PCE degradation with recirculation flow rate 2L/min: without air: influence of initial PCE concentration (50, 250, 500 and 750 ppb or µg/L)

From the kinetic data, it was observed that the degradation kinetics are independent of the initial PCE concentration.

Indeed, comparing the kinetic curves obtained from the photocatalytic tests at initial PCE concentrations of 50, 250, 500 and 750 microg/L or ppb, similar behaviour was observed for of 50, 250, and 500 initial concentrations after the first five hours of irradiation, leading to PCE degradation of 80%, 83% and 77%, respectively. Increasing the concentration to 750 ppb worsened the photocatalytic activity with only

55% of PCE being degraded, most likely due to the occupation by PCE molecules of the system's active sites that are therefore no longer available for the generation of hydroxyl radicals (Johnson et al.1996).

3.7 HP-NcAs aerogels photcatalytic ATZ and THI degradation with pilot-scale reactor

The aerogel composites sPS/NdT, sPS/[30ZnO/NdT] and sPS/[Fe^0/ZnS] with a 90% of porosity were tested in photocatalytic ATZ degradation processes using the pilot-scale reactor described in section 3.3.6. After the illumination time of 180 min, the samples sPS/[Fe^0/ZnS] achieved 95% of ATZ degradation and the sPS/NdTand sPS/[30ZnO/NdT] samples 94% (Figure 64).

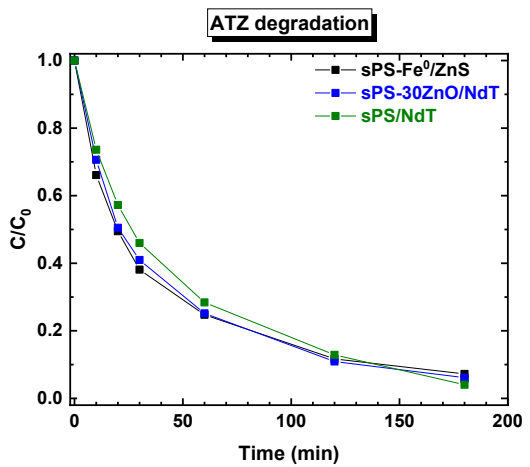

Figure 64. Atrazine degradation under UV irradiation with the composite aerogels sPS/[Fe0/ZnS], sPS/[30ZnO/NdT] and sPS/NdT using the pilot-plant scale reactor.

Using the same photocatalytic reactor, the activity towards degradation of thiacloprid, pesticide discussed in the introduction part, listed as emerging concern contaminant CEC, was also assessed (Figure 65).

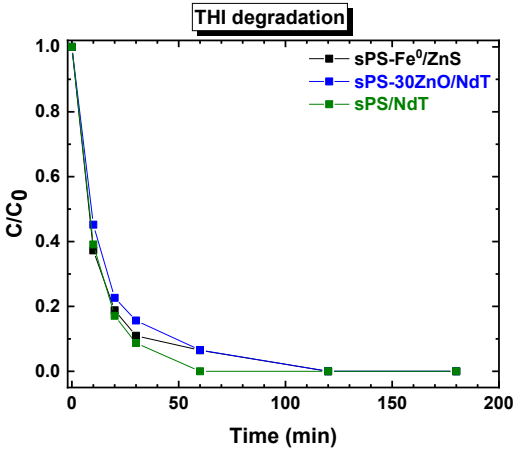

Figure 65. Thiacloprid degradation under UV irradiation with the composite aerogels sPS/[Fe^0/ZnS], sPS/[30ZnO/NdT] and sPS/NdT using the pilot-plant scale reactor.

Degradation curves showed that the photocatalytic composites were able to efficiently degrade this other contaminant as well and with fast kinetics. In fact, after 30 min of irradiation degradation reaches a percentage value of 94%, 92% and 85% respectively for the samples sPS/[Fe^0/ZnS], sPS/[30ZnO/NdT] and sPS/NdT.

The results obtained from the degradation of ATZ and THI with the pilot-scale reactor showed that the materials could be of interest for a subsequent scale-up of the process.

Conclusions

Heterojunction-based systems xZnO/NdT and ZnO/TiO_2 were prepared by simply mixing the two single catalysts in 2-propanol solution (1 M). XRD and UV-Vis DRS spectrum confirmed the effective composite formation. The samples 30ZnO/NdT and 50ZnO/NdT showed higher photocatalytic activity under UV irradiation compared with bare NdT and ZnO, leading to the complete ATZ degradation after 30 min of irradiation.

The prepared xZnO/NdT composites exhibited lower catalytic performance in ATZ degradation under visible irradiation, however for the 15ZnO/NdT sample an increase in activity is observed compared to all other samples.

The 30ZnO/NdT composite was also active in the photocatalytic process driven by natural sunlight, confirming the initial hypothesis that coupling ZnO with NdT to form heterojunction could increase the performance of the photocatalyst by shifting activity to solar as well.

According to the results discussed above, we can conclude that HP-NcAs, sPS/NdT, sPS/xZnO-NdT and sPS/[Fe^0/ZnS] constitute promising synergic systems for ATZ degradation under UV and VIS light irradiation. The existence of a relationship between percentage sorption of the contaminant and aerogel porosity in dark conditions highlights the ability

of aerogel to act not only as a support for the catalysts, but also as a pre-concentrator of the contaminant itself.

Indeed, the photocatalytic system sPS/NdT exhibited higher degradation performances than NdT powder catalyst for both UV and Vis photocatalytic process because of the aerogel's sorption properties towards atrazine.

Kinetics and ecotoxicity data underline that the photocatalytic treatment in presence of UV light is more effective than Vis one in degrading ATZ and its degradation by-products and thus better alleviates effluent ecotoxicity.

In fact, ecotoxicity studies on a battery of three biological assays on *R. subcapitata*, *A. fischeri* and *D. magna* showed that extending the process time up to 72 h for the UV process resulted in a reduction in toxicity, with only 6% inhibition for the growth of *R. subcapitata* and no lethality for *D. magna*. At the opposite, the Vis process after 72 h of treatment still resulted in 99% inhibition for algal growth and 58% mortality for the crustacean.

Compared to the other HP-NcAs, the novel sPS/[30ZnO/NdT] sample shown the best photocatalytic performance under UV irradiation for ATZ degradation. However, the reactor configuration does not make them ideal candidates when used in sunlight-driven photocatalytic does not allow good irradiation of the entire catalytic system. The polymeric films TNT/[30ZnO/NdT] and PP/[30ZnO/NdT], on the other hand, are suitable

candidates for sunlight-driven photocatalytic processes, because the sunlight is most likely able to activate all the sites of the photocatalyst dispersed on the film.

Pilot reactor tests for the degradation of synthetic solutions of ATZ and THI (20 L) were performed with HP-NcAs sPS/NdT, sPS/[30ZnO/NdT] and sPS/[Fe^0/ZnS], and these proved to be suitable candidate for the degradation of both contaminants, leading to complete degradation after 180 minutes of irradiation.

References

1. WHO | The World Health Report 2005 - Make Every Mother and Child Count Available online: https://www.who.int/whr/2005/en/ (accessed on 1 February 2021).
2. Sousa, J.C.G.; Ribeiro, A.R.; Barbosa, M.O.; Pereira, M.F.R.; Silva, A.M.T. A Review on Environmental Monitoring of Water Organic Pollutants Identified by EU Guidelines. *J. Hazard. Mater.* **2018**, *344*, 146–162, doi:10.1016/j.jhazmat.2017.09.058.
3. Gorito, A.M.; Ribeiro, A.R.; Almeida, C.M.R.; Silva, A.M.T. A Review on the Application of Constructed Wetlands for the Removal of Priority Substances and Contaminants of Emerging Concern Listed in Recently Launched EU Legislation. *Environ. Pollut.* **2017**, *227*, 428–443, doi:10.1016/j.envpol.2017.04.060.
4. International Decade for Action "Water for Life" 2005-2015. Focus Areas: Water Scarcity Available online: https://www.un.org/waterforlifedecade/scarcity.shtml (accessed on 18 February 2021).
5. Rizzo, L.; Krätke, R.; Linders, J.; Scott, M.; Vighi, M.; de Voogt, P. Proposed EU Minimum Quality Requirements for Water Reuse in Agricultural Irrigation and Aquifer Recharge: SCHEER Scientific Advice. *Curr. Opin. Environ. Sci. Health* **2018**, *2*, 7–11, doi:10.1016/j.coesh.2017.12.004.
6. Rizzo, L.; Gernjak, W.; Krzeminski, P.; Malato, S.; McArdell, C.S.; Perez, J.A.S.; Schaar, H.; Fatta-Kassinos, D. Best Available Technologies and Treatment Trains to Address Current Challenges in Urban Wastewater Reuse for Irrigation of Crops in EU Countries. *Sci. Total Environ.* **2020**, *710*, 136312, doi:10.1016/j.scitotenv.2019.136312.
7. *Regulation (EU) 2020/741 of the European Parliament and of the Council of 25 May 2020 on Minimum Requirements for Water Reuse (Text with EEA Relevance)*; 2020; Vol. 177;.
8. Thomaidis, N.S.; Asimakopoulos, A.G.; Bletsou, A.A. EMERGING CONTAMINANTS: A TUTORIAL MINI-REVIEW. *Emerg. Contam.* 8.
9. Corominas, Ll.; Foley, J.; Guest, J.S.; Hospido, A.; Larsen, H.F.; Morera, S.; Shaw, A. Life Cycle Assessment Applied to Wastewater Treatment: State of the Art. *Water Res.* **2013**, *47*, 5480–5492, doi:10.1016/j.watres.2013.06.049.
10. A, I.A.; O, A.B.; AbimbolaP, O.; A, A.-A.T.; O, D.A.; ToyinA, O. Water Pollution: Effects, Prevention, and Climatic Impact. *Water Chall. Urban. World* **2018**, doi:10.5772/intechopen.72018.
11. Rozas, O.; Vidal, C.; Baeza, C.; Jardim, W.F.; Rossner, A.;

Mansilla, H.D. Organic Micropollutants (OMPs) in Natural Waters: Oxidation by UV/H2O2 Treatment and Toxicity Assessment. *Water Res.* **2016**, *98*, 109–118, doi:10.1016/j.watres.2016.03.069.
12. Burkhardt-Holm, P. Linking Water Quality to Human Health and Environment: The Fate of Micropollutants. *Inst Water Policy Natl Univ Singap.* **2011**.
13. Dewil, R.; Mantzavinos, D.; Poulios, I.; Rodrigo, M.A. New Perspectives for Advanced Oxidation Processes. *J. Environ. Manage.* **2017**, *195*, 93–99, doi:10.1016/j.jenvman.2017.04.010.
14. Luca, A.D.; Dantas, R.F.; Simões, A.S.M.; Toscano, I. a. S.; Lofrano, G.; Cruz, A.; Esplugas, S. Atrazine Removal in Municipal Secondary Effluents by Fenton and Photo-Fenton Treatments. *Chem. Eng. Technol.* **2013**, *36*, 2155–2162, doi:https://doi.org/10.1002/ceat.201300135.
15. Comninellis, C.; Kapalka, A.; Malato, S.; Parsons, S.A.; Poulios, I.; Mantzavinos, D. Advanced Oxidation Processes for Water Treatment: Advances and Trends for R&D. *J. Chem. Technol. Biotechnol.* **2008**, *83*, 769–776, doi:10.1002/jctb.1873.
16. Fate of wastewater-derived contaminants in surface waters - ProQuest Available online: https://search.proquest.com/openview/140c389b42daf5485bd8c64d174a82ae/1?pq-origsite=gscholar&cbl=18750&diss=y (accessed on 2 February 2021).
17. Luo, Y.; Guo, W.; Ngo, H.H.; Nghiem, L.D.; Hai, F.I.; Zhang, J.; Liang, S.; Wang, X.C. A Review on the Occurrence of Micropollutants in the Aquatic Environment and Their Fate and Removal during Wastewater Treatment. *Sci. Total Environ.* **2014**, *473–474*, 619–641, doi:10.1016/j.scitotenv.2013.12.065.
18. EUR-Lex - 32008L0105 - EN - EUR-Lex Available online: https://eur-lex.europa.eu/legal-content/EN/ALL/?uri=celex%3A32008L0105 (accessed on 2 February 2021).
19. EUR-Lex - 32013L0039 - EN - EUR-Lex Available online: https://eur-lex.europa.eu/legal-content/EN/ALL/?uri=celex%3A32013L0039 (accessed on 2 February 2021).
20. Sharma, B.M.; Bečanová, J.; Scheringer, M.; Sharma, A.; Bharat, G.K.; Whitehead, P.G.; Klánová, J.; Nizzetto, L. Health and Ecological Risk Assessment of Emerging Contaminants (Pharmaceuticals, Personal Care Products, and Artificial Sweeteners) in Surface and Groundwater (Drinking Water) in the Ganges River Basin, India. *Sci. Total Environ.* **2019**, *646*, 1459–1467, doi:10.1016/j.scitotenv.2018.07.235.

21. *Commission Implementing Decision (EU) 2015/495 of 20 March 2015 Establishing a Watch List of Substances for Union-Wide Monitoring in the Field of Water Policy Pursuant to Directive 2008/105/EC of the European Parliament and of the Council (Notified under Document C(2015) 1756) Text with EEA Relevance*; 2015; Vol. 078;
22. Solarchem Environmental Systems *The UV/Oxidation Handbook.*; Solarchem Environmental Systems: Markham, Ont., Canada; Las Vegas, Nev., 1994;
23. Gogate, P.R.; Pandit, A.B. A Review of Imperative Technologies for Wastewater Treatment I: Oxidation Technologies at Ambient Conditions. *Adv. Environ. Res.* **2004**, *8*, 501–551, doi:10.1016/S1093-0191(03)00032-7.
24. Fang, G.-D.; Dionysiou, D.D.; Wang, Y.; Al-Abed, S.R.; Zhou, D.-M. Sulfate Radical-Based Degradation of Polychlorinated Biphenyls: Effects of Chloride Ion and Reaction Kinetics. *J. Hazard. Mater.* **2012**, *227–228*, 394–401, doi:10.1016/j.jhazmat.2012.05.074.
25. Hoffmann, M.R.; Martin, S.T.; Choi, Wonyong.; Bahnemann, D.W. Environmental Applications of Semiconductor Photocatalysis. *Chem. Rev.* **1995**, *95*, 69–96, doi:10.1021/cr00033a004.
26. Ikehata, K.; Gamal El-Din, M. Aqueous Pesticide Degradation by Ozonation and Ozone-Based Advanced Oxidation Processes: A Review (Part II). *Ozone Sci. Eng.* **2005**, *27*, 173–202, doi:10.1080/01919510590945732.
27. Joseph, C.G.; Li Puma, G.; Bono, A.; Krishnaiah, D. Sonophotocatalysis in Advanced Oxidation Process: A Short Review. *Ultrason. Sonochem.* **2009**, *16*, 583–589, doi:10.1016/j.ultsonch.2009.02.002.
28. Mishra, V.S.; Mahajani, V.V.; Joshi, J.B. Wet Air Oxidation. *Ind. Eng. Chem. Res.* **1995**, *34*, 2–48, doi:10.1021/ie00040a001.
29. Levec, J.; Pintar, A. Catalytic Wet-Air Oxidation Processes: A Review. *Catal. Today* **2007**, *124*, 172–184, doi:10.1016/j.cattod.2007.03.035.
30. Nidheesh, P.V.; Gandhimathi, R. Trends in Electro-Fenton Process for Water and Wastewater Treatment: An Overview. *Desalination* **2012**, *299*, 1–15, doi:10.1016/j.desal.2012.05.011.
31. Serpone, N.; Horikoshi, S.; Emeline, A.V. Microwaves in Advanced Oxidation Processes for Environmental Applications. A Brief Review. *J. Photochem. Photobiol. C Photochem. Rev.* **2010**, *11*, 114–131, doi:10.1016/j.jphotochemrev.2010.07.003.
32. Pera-Titus, M.; García-Molina, V.; Baños, M.A.; Giménez, J.; Esplugas, S. Degradation of Chlorophenols by Means of Advanced

Oxidation Processes: A General Review. *Appl. Catal. B Environ.* **2004**, *47*, 219–256, doi:10.1016/j.apcatb.2003.09.010.
33. Stasinakis, A. USE OF SELECTED ADVANCED OXIDATION PROCESSES (AOPs) FOR WASTEWATER TREATMENT - A MINI REVIEW.; 2008.
34. Govindaraj, D.; Nambi, I.; Jaganathan, S. Nanocatalysts in Fenton Based Advanced Oxidation Process for Water and Wastewater Treatment. *J. Bionanoscience* **2016**, *10*, 356-368(13), doi:10.1166/jbns.2016.1387.
35. Srikanth, B.; Goutham, R.; Badri Narayan, R.; Ramprasath, A.; Gopinath, K.P.; Sankaranarayanan, A.R. Recent Advancements in Supporting Materials for Immobilised Photocatalytic Applications in Waste Water Treatment. *J. Environ. Manage.* **2017**, *200*, 60–78, doi:10.1016/j.jenvman.2017.05.063.
36. Scopus Preview - Scopus - Welcome to Scopus Available online: https://www.scopus.com/ (accessed on 28 May 2021).
37. Fujishima, A.; Honda, K. Electrochemical Photolysis of Water at a Semiconductor Electrode. *Nature* **1972**, *238*, 37–38, doi:10.1038/238037a0.
38. Fujishima, A.; Rao, T.N.; Tryk, D.A. Titanium Dioxide Photocatalysis. *J. Photochem. Photobiol. C Photochem. Rev.* **2000**, *1*, 1–21, doi:10.1016/S1389-5567(00)00002-2.
39. Mills, A.; Le Hunte, S. An Overview of Semiconductor Photocatalysis. *J. Photochem. Photobiol. Chem.* **1997**, *108*, 1–35, doi:10.1016/S1010-6030(97)00118-4.
40. Pelaez, M.; Nolan, N.T.; Pillai, S.C.; Seery, M.K.; Falaras, P.; Kontos, A.G.; Dunlop, P.S.M.; Hamilton, J.W.J.; Byrne, J.A.; O'Shea, K.; et al. A Review on the Visible Light Active Titanium Dioxide Photocatalysts for Environmental Applications. *Appl. Catal. B Environ.* **2012**, *125*, 331–349, doi:10.1016/j.apcatb.2012.05.036.
41. Heterogeneous Photocatalytic Oxidation of Cyanide Ion in Aqueous Solutions at Titanium Dioxide Powder | Journal of the American Chemical Society Available online: https://pubs.acs.org/doi/10.1021/ja00443a081 (accessed on 18 March 2021).
42. Zaviska, F.; Drogui, P.; Mercier, G.; Blais, J.-F. Procédés d'oxydation avancée dans le traitement des eaux et des effluents industriels: Application à la dégradation des polluants réfractaires. *Rev. Sci. Eau J. Water Sci.* **2009**, *22*, 535–564, doi:10.7202/038330ar.
43. Pitre, S.P.; Yoon, T.P.; Scaiano, J.C. Titanium Dioxide Visible Light Photocatalysis: Surface Association Enables Photocatalysis with Visible Light Irradiation. *Chem. Commun.* **2017**, *53*, 4335–

4338, doi:10.1039/C7CC01952A.
44. Ansari, S.A.; Ansari, S.G.; Foaud, H.; Cho, M.H. Facile and Sustainable Synthesis of Carbon-Doped ZnO Nanostructures towards the Superior Visible Light Photocatalytic Performance. *New J. Chem.* **2017**, *41*, 9314–9320, doi:10.1039/C6NJ04070E.
45. Kabra, K.; Chaudhary, R.; Sawhney, R.L. Treatment of Hazardous Organic and Inorganic Compounds through Aqueous-Phase Photocatalysis: A Review. *Ind. Eng. Chem. Res.* **2004**, *43*, 7683–7696, doi:10.1021/ie0498551.
46. Sakthivel, S.; Kisch, H. Photocatalytic and Photoelectrochemical Properties of Nitrogen-Doped Titanium Dioxide. *ChemPhysChem* **2003**, *4*, 487–490, doi:https://doi.org/10.1002/cphc.200200554.
47. Di Paola, A.; Bellardita, M.; Palmisano, L. Brookite, the Least Known TiO2 Photocatalyst. *Catalysts* **2013**, *3*, 36–73, doi:10.3390/catal3010036.
48. Luttrell, T.; Halpegamage, S.; Tao, J.; Kramer, A.; Sutter, E.; Batzill, M. Why Is Anatase a Better Photocatalyst than Rutile? - Model Studies on Epitaxial TiO2 Films. *Sci. Rep.* **2014**, *4*, doi:10.1038/srep04043.
49. Huang, P.J.; Chang, H.; Yeh, C.T.; Tsai, C.W. Phase Transformation of TiO2 Monitored by Thermo-Raman Spectroscopy with TGA/DTA. *Thermochim. Acta* **1997**, *297*, 85–92, doi:10.1016/S0040-6031(97)00168-8.
50. Yang, S.; Quan, X.; Li, X.; Sun, C. Photoelectrocatalytic Treatment of Pentachlorophenol in Aqueous Solution Using a Rutile Nanotube-like TiO2/Ti Electrode. *Photochem. Photobiol. Sci.* **2006**, *5*, 808–814, doi:10.1039/B604077B.
51. Choi, W.; Termin, A.; Hoffmann, M.R. The Role of Metal Ion Dopants in Quantum-Sized TiO2: Correlation between Photoreactivity and Charge Carrier Recombination Dynamics. *J. Phys. Chem.* **1994**, *98*, 13669–13679, doi:10.1021/j100102a038.
52. Liu, J.; Ma, N.; Wu, W.; He, Q. Recent Progress on Photocatalytic Heterostructures with Full Solar Spectral Responses. *Chem. Eng. J.* **2020**, *393*, 124719, doi:10.1016/j.cej.2020.124719.
53. Ansari, S.A.; Khan, M.M.; Ansari, M.O.; Cho, M.H. Nitrogen-Doped Titanium Dioxide (N-Doped TiO2) for Visible Light Photocatalysis. *New J. Chem.* **2016**, *40*, 3000–3009, doi:10.1039/C5NJ03478G.
54. Multifunctional P-Doped TiO2 Films: A New Approach to Self-Cleaning, Transparent Conducting Oxide Materials | Chemistry of Materials Available online: https://pubs.acs.org/doi/10.1021/cm504734a (accessed on 18 March 2021).
55. Siuzdak, K.; Szkoda, M.; Lisowska-Oleksiak, A.; Grochowska, K.;

Karczewski, J.; Ryl, J. Thin Layer of Ordered Boron-Doped TiO2 Nanotubes Fabricated in a Novel Type of Electrolyte and Characterized by Remarkably Improved Photoactivity. *Appl. Surf. Sci.* **2015**, *357*, 942–950, doi:10.1016/j.apsusc.2015.09.130.

56. Pal, U.; Ghosh, S.; Chatterjee, D. Effect of Sacrificial Electron Donors on Hydrogen Generation over Visible Light–Irradiated Nonmetal-Doped TiO2 Photocatalysts. *Transit. Met. Chem.* **2012**, *37*, 93–96, doi:10.1007/s11243-011-9562-3.
57. Wen, C.Z.; Hu, Q.H.; Guo, Y.N.; Gong, X.Q.; Qiao, S.Z.; Yang, H.G. From Titanium Oxydifluoride (TiOF2) to Titania (TiO2): Phase Transition and Non-Metal Doping with Enhanced Photocatalytic Hydrogen (H2) Evolution Properties. *Chem. Commun.* **2011**, *47*, 6138–6140, doi:10.1039/C1CC10851D.
58. Kushwaha, R.; Chauhan, R.; Srivastava, P.; Bahadur, L. Synthesis and Characterization of Nitrogen-Doped TiO2 Samples and Their Application as Thin Film Electrodes in Dye-Sensitized Solar Cells. *J. Solid State Electrochem.* **2015**, *19*, 507–517, doi:10.1007/s10008-014-2623-8.
59. Livraghi, S.; Paganini, M.C.; Giamello, E.; Selloni, A.; Di Valentin, C.; Pacchioni, G. Origin of Photoactivity of Nitrogen-Doped Titanium Dioxide under Visible Light. *J. Am. Chem. Soc.* **2006**, *128*, 15666–15671, doi:10.1021/ja064164c.
60. Di Valentin, C.; Finazzi, E.; Pacchioni, G.; Selloni, A.; Livraghi, S.; Paganini, M.C.; Giamello, E. N-Doped TiO 2: Theory and Experiment. *Chem. Phys.* **2007**, *339*, 44–56, doi:10.1016/j.chemphys.2007.07.020.
61. Sreethawong, T. Mesoporous-Assembled Nanocrystal Photocatalysts for Degradation of Azo Dyes. In *Advances in Water Treatment and Pollution Prevention*; Sharma, S.K., Sanghi, R., Eds.; Springer Netherlands: Dordrecht, 2012; pp. 147–175 ISBN 978-94-007-4204-8.
62. Buzby, S.; Barakat, M.A.; Lin, H.; Ni, C.; Rykov, S.A.; Chen, J.G.; Ismat Shah, S. Visible Light Photocatalysis with Nitrogen-Doped Titanium Dioxide Nanoparticles Prepared by Plasma Assisted Chemical Vapor Deposition. *J. Vac. Sci. Technol. B Microelectron. Nanometer Struct. Process. Meas. Phenom.* **2006**, *24*, 1210–1214, doi:10.1116/1.2192544.
63. Carbon and Nitrogen Co-Doped TiO2 with Enhanced Visible-Light Photocatalytic Activity | Industrial & Engineering Chemistry Research Available online: https://pubs.acs.org/doi/abs/10.1021/ie061491k?src=recsys (accessed on 18 March 2021).
64. Zhao, Z.; Fan, J.; Wang, J.; Li, R. Effect of Heating Temperature on Photocatalytic Reduction of CO2 by N–TiO2 Nanotube

Catalyst. *Catal. Commun.* **2012**, *21*, 32–37, doi:10.1016/j.catcom.2012.01.022.
65. Truong, Q.D.; Le, T.H.; Liu, J.-Y.; Chung, C.-C.; Ling, Y.-C. Synthesis of TiO2 Nanoparticles Using Novel Titanium Oxalate Complex towards Visible Light-Driven Photocatalytic Reduction of CO2 to CH3OH. *Appl. Catal. Gen.* **2012**, *437–438*, 28–35, doi:10.1016/j.apcata.2012.06.009.
66. Chen, C.; Bai, H.; Chang, S.; Chang, C.; Den, W. Preparation of N-Doped TiO2 Photocatalyst by Atmospheric Pressure Plasma Process for VOCs Decomposition under UV and Visible Light Sources. *J. Nanoparticle Res.* **2007**, *9*, 365–375, doi:10.1007/s11051-006-9141-2.
67. Sacco, O.; Murcia, J.J.; Lara, A.E.; Hernández-Laverde, M.; Rojas, H.; Navío, J.A.; Hidalgo, M.C.; Vaiano, V. Pt–TiO2–Nb2O5 Heterojunction as Effective Photocatalyst for the Degradation of Diclofenac and Ketoprofen. *Mater. Sci. Semicond. Process.* **2020**, *107*, 104839, doi:10.1016/j.mssp.2019.104839.
68. Kumar, A.; Khan, M.; He, J.; Lo, I.M.C. Recent Developments and Challenges in Practical Application of Visible–Light–Driven TiO2–Based Heterojunctions for PPCP Degradation: A Critical Review. *Water Res.* **2020**, *170*, 115356, doi:10.1016/j.watres.2019.115356.
69. Wang, H.; Zhang, L.; Chen, Z.; Hu, J.; Li, S.; Wang, Z.; Liu, J.; Wang, X. Semiconductor Heterojunction Photocatalysts: Design, Construction, and Photocatalytic Performances. *Chem. Soc. Rev.* **2014**, *43*, 5234–5244, doi:10.1039/C4CS00126E.
70. Wang, L.; Fu, X.; Han, Y.; Chang, E.; Wu, H.; Wang, H.; Li, K.; Qi, X. Preparation, Characterization, and Photocatalytic Activity of TiO2/ZnO Nanocomposites. *J. Nanomater.* **2013**, *2013*, 321459, doi:10.1155/2013/321459.
71. Isac, L.; Andronic, L.; Visa, M.; Enesca, A. Selective Photocatalytic Degradation of Organic Pollutants by CuxS/ZnO/TiO2 Heterostructures. *Ceram. Int.* **2020**, *46*, 4265–4273, doi:10.1016/j.ceramint.2019.10.147.
72. Carp, O.; Huisman, C.L.; Reller, A. Photoinduced Reactivity of Titanium Dioxide. *Prog. Solid State Chem.* **2004**, *32*, 33–177, doi:10.1016/j.progsolidstchem.2004.08.001.
73. Cassiers, K.; Linssen, T.; Mathieu, M.; Bai, Y.Q.; Zhu, H.Y.; Cool, P.; Vansant, E.F. Surfactant-Directed Synthesis of Mesoporous Titania with Nanocrystalline Anatase Walls and Remarkable Thermal Stability. *J. Phys. Chem. B* **2004**, *108*, 3713–3721, doi:10.1021/jp036830r.
74. Preparation and Characterization of Stable Biphase TiO2 Photocatalyst with High Crystallinity, Large Surface Area, and

Enhanced Photoactivity | The Journal of Physical Chemistry C Available online: https://pubs.acs.org/doi/abs/10.1021/jp710283p (accessed on 29 March 2021).
75. Stefaniuk, M.; Oleszczuk, P.; Ok, Y.S. Review on Nano Zerovalent Iron (NZVI): From Synthesis to Environmental Applications. *Chem. Eng. J.* **2016**, *287*, 618–632, doi:10.1016/j.cej.2015.11.046.
76. Dong, H.; Ahmad, K.; Zeng, G.; Li, Z.; Chen, G.; He, Q.; Xie, Y.; Wu, Y.; Zhao, F.; Zeng, Y. Influence of Fulvic Acid on the Colloidal Stability and Reactivity of Nanoscale Zero-Valent Iron. *Environ. Pollut.* **2016**, *211*, 363–369, doi:10.1016/j.envpol.2016.01.017.
77. Shah, N.S.; Ali Khan, J.; Sayed, M.; Ul Haq Khan, Z.; Sajid Ali, H.; Murtaza, B.; Khan, H.M.; Imran, M.; Muhammad, N. Hydroxyl and Sulfate Radical Mediated Degradation of Ciprofloxacin Using Nano Zerovalent Manganese Catalyzed S2O82−. *Chem. Eng. J.* **2019**, *356*, 199–209, doi:10.1016/j.cej.2018.09.009.
78. Sohn, K.; Kang, S.W.; Ahn, S.; Woo, M.; Yang, S.-K. Fe(0) Nanoparticles for Nitrate Reduction: Stability, Reactivity, and Transformation. *Environ. Sci. Technol.* **2006**, *40*, 5514–5519, doi:10.1021/es0525758.
79. Zhang, W. Nanoscale Iron Particles for Environmental Remediation: An Overview. *J. Nanoparticle Res.* **2003**, *5*, 323–332, doi:10.1023/A:1025520116015.
80. Sacco, O.; Vaiano, V.; Navarra, W.; Daniel, C.; Pragliola, S.; Venditto, V. Catalytic System Based on Recyclable Fe0 and ZnS Semiconductor for UV-Promoted Degradation of Chlorinated Organic Compounds. *Sep. Purif. Technol.* **2021**, *270*, 118830, doi:10.1016/j.seppur.2021.118830.
81. Premanathan, M.; Karthikeyan, K.; Jeyasubramanian, K.; Manivannan, G. Selective Toxicity of ZnO Nanoparticles toward Gram-Positive Bacteria and Cancer Cells by Apoptosis through Lipid Peroxidation. *Nanomedicine Nanotechnol. Biol. Med.* **2011**, *7*, 184–192, doi:10.1016/j.nano.2010.10.001.
82. MiarAlipour, S.; Friedmann, D.; Scott, J.; Amal, R. TiO2/Porous Adsorbents: Recent Advances and Novel Applications. *J. Hazard. Mater.* **2018**, *341*, 404–423, doi:10.1016/j.jhazmat.2017.07.070.
83. White, R.J.; Luque, R.; Budarin, V.L.; Clark, J.H.; Macquarrie, D.J. Supported Metal Nanoparticles on Porous Materials. Methods and Applications. *Chem. Soc. Rev.* **2009**, *38*, 481–494, doi:10.1039/B802654H.
84. Kistler, S.S. Coherent Expanded Aerogels and Jellies. *Nature* **1931**, *127*, 741–741, doi:10.1038/127741a0.

85. Maleki, H.; Hüsing, N. Current Status, Opportunities and Challenges in Catalytic and Photocatalytic Applications of Aerogels: Environmental Protection Aspects. *Appl. Catal. B Environ.* **2018**, *221*, 530–555, doi:10.1016/j.apcatb.2017.08.012.
86. Hüsing, N.; Schubert, U. Aerogels—Airy Materials: Chemistry, Structure, and Properties. *Angew. Chem. Int. Ed.* **1998**, *37*, 22–45, doi:10.1002/(SICI)1521-3773(19980202)37:1/2<22::AID-ANIE22>3.0.CO;2-I.
87. Wan, W.; Zhang, R.; Ma, M.; Zhou, Y. Monolithic Aerogel Photocatalysts: A Review. *J. Mater. Chem. A* **2018**, *6*, 754–775, doi:10.1039/C7TA09227J.
88. Li, X.; Zhu, J.; Wei, B. Hybrid Nanostructures of Metal/Two-Dimensional Nanomaterials for Plasmon-Enhanced Applications. *Chem. Soc. Rev.* **2016**, *45*, 3145–3187, doi:10.1039/C6CS00195E.
89. Cao, S.; Yeung, K.L.; Yue, P.-L. An Investigation of Trichloroethylene Photocatalytic Oxidation on Mesoporous Titania-Silica Aerogel Catalysts. *Appl. Catal. B Environ.* **2007**, *76*, 64–72, doi:10.1016/j.apcatb.2007.05.009.
90. Cao, S.; Yeung, K.L.; Kwan, J.K.C.; To, P.M.T.; Yu, S.C.T. An Investigation of the Performance of Catalytic Aerogel Filters. *Appl. Catal. B Environ.* **2009**, *86*, 127–136, doi:10.1016/j.apcatb.2008.08.019.
91. Ahmed, M.S.; Attia, Y.A. Aerogel Materials for Photocatalytic Detoxification of Cyanide Wastes in Water. *J. Non-Cryst. Solids* **1995**, *186*, 402–407, doi:10.1016/0022-3093(95)00085-2.
92. Deng, Z.; Wang, J.; Zhang, Y.; Weng, Z.; Zhang, Z.; Zhou, B.; Shen, J.; Cheng, L. Preparation and Photocatalytic Activity of TiO2-SiO2 Binary Aerogels. *Nanostructured Mater.* **1999**, *11*, 1313–1318, doi:10.1016/S0965-9773(99)00423-7.
93. Gao, X.; Wachs, I.E. Titania–Silica as Catalysts: Molecular Structural Characteristics and Physico-Chemical Properties. *Catal. Today* **1999**, *51*, 233–254, doi:10.1016/S0920-5861(99)00048-6.
94. Zhu, J.; Xie, J.; Lü, X.; Jiang, D. Synthesis and Characterization of Superhydrophobic Silica and Silica/Titania Aerogels by Sol–Gel Method at Ambient Pressure. *Colloids Surf. Physicochem. Eng. Asp.* **2009**, *342*, 97–101, doi:10.1016/j.colsurfa.2009.04.016.
95. Fan, C.; Liu, Q.; Ma, T.; Shen, J.; Yang, Y.; Tang, H.; Wang, Y.; Yang, J. Fabrication of 3D CeVO4/Graphene Aerogels with Efficient Visible-Light Photocatalytic Activity. *Ceram. Int.* **2016**, *42*, 10487–10492, doi:10.1016/j.ceramint.2016.03.072.
96. Cai, J.; Liu, W.; Li, Z. One-Pot Self-Assembly of Cu2O/RGO Composite Aerogel for Aqueous Photocatalysis. *Appl. Surf. Sci.* **2015**, *358*, 146–151, doi:10.1016/j.apsusc.2015.08.021.
97. Liu, W.; Cai, J.; Li, Z. Self-Assembly of Semiconductor

Nanoparticles/Reduced Graphene Oxide (RGO) Composite Aerogels for Enhanced Photocatalytic Performance and Facile Recycling in Aqueous Photocatalysis. *ACS Sustain. Chem. Eng.* **2015**, *3*, 277–282, doi:10.1021/sc5006473.

98. Sacco, O.; Vaiano, V.; Daniel, C.; Navarra, W.; Venditto, V. Removal of Phenol in Aqueous Media by N-Doped TiO2 Based Photocatalytic Aerogels. *Mater. Sci. Semicond. Process.* **2018**, *80*, 104–110, doi:10.1016/j.mssp.2018.02.032.
99. Sacco, O.; Vaiano, V.; Daniel, C.; Navarra, W.; Venditto, V. Highly Robust and Selective System for Water Pollutants Removal: How to Transform a Traditional Photocatalyst into a Highly Robust and Selective System for Water Pollutants Removal. *Nanomater. Basel Switz.* **2019**, *9*, doi:10.3390/nano9111509.
100. Vaiano, V.; Sacco, O.; Sannino, D.; Ciambelli, P.; Longo, S.; Venditto, V.; Guerra, G. N-Doped TiO2/s-PS Aerogels for Photocatalytic Degradation of Organic Dyes in Wastewater under Visible Light Irradiation. *J. Chem. Technol. Biotechnol.* **2014**, *89*, 1175–1181, doi:https://doi.org/10.1002/jctb.4372.
101. Zhang, H.; Hussain, I.; Brust, M.; Butler, M.F.; Rannard, S.P.; Cooper, A.I. Aligned Two- and Three-Dimensional Structures by Directional Freezing of Polymers and Nanoparticles. *Nat. Mater.* **2005**, *4*, 787–793, doi:10.1038/nmat1487.
102. Zhang, R.; Wan, W.; Qiu, L.; Zhou, Y. Facile Synthesis Route for MoS2-Polyvinylpyrrolidone Aerogels. *Mater. Lett.* **2016**, *181*, 321–324, doi:10.1016/j.matlet.2016.06.062.
103. Ry, Z.; Wc, W.; Lj, Q.; Yh, W.; Y, Z. Preparation of hydrophobic polyvinyl alcohol aerogel via the surface modification of boron nitride for environmental remediation. *Appl. Surf. Sci.* **2017**, *419*, 342–347.
104. Jiang, W.; Liu, Y.; Wang, J.; Zhang, M.; Luo, W.; Zhu, Y. Separation-Free Polyaniline/TiO2 3D Hydrogel with High Photocatalytic Activity. *Adv. Mater. Interfaces* **2016**, *3*, 1500502, doi:https://doi.org/10.1002/admi.201500502.
105. Guerra, G.; Daniel, C.; Rizzo, P.; Tarallo, O. Advanced Materials Based on Polymer Cocrystalline Forms. *J. Polym. Sci. Part B Polym. Phys.* **2012**, *50*, 305–322, doi:https://doi.org/10.1002/polb.23035.
106. Daniel, C.; Antico, P.; Yamaguchi, H.; Kogure, M.; Guerra, G. Microporous-Crystalline Microfibers by Eco-Friendly Guests: An Efficient Tool for Sorption of Volatile Organic Pollutants. *Microporous Mesoporous Mater.* **2016**, *232*, 205–210, doi:10.1016/j.micromeso.2016.06.028.
107. Etched Fibers of Syndiotactic Polystyrene with Nanoporous-

Crystalline Phases | Macromolecules Available online: https://pubs.acs.org/doi/10.1021/acs.macromol.8b01044 (accessed on 18 March 2021).
108. Syndiotactic Polystyrene Aerogels: Adsorption in Amorphous Pores and Absorption in Crystalline Nanocavities | Chemistry of Materials Available online: https://pubs.acs.org/doi/abs/10.1021/cm702475a (accessed on 18 March 2021).
109. Manfredi, C.; Del Nobile, M.A.; Mensitieri, G.; Guerra, G.; Rapacciuolo, M. Vapor Sorption in Emptied Clathrate Samples of Syndiotactic Polystyrene. *J. Polym. Sci. Part B Polym. Phys.* **1997**, *35*, 133–140, doi:10.1002/(SICI)1099-0488(19970115)35:1<133::AID-POLB11>3.0.CO;2-E.
110. Musto, P.; Mensitieri, G.; Cotugno, S.; Guerra, G.; Venditto, V. Probing by Time-Resolved FTIR Spectroscopy Mass Transport, Molecular Interactions, and Conformational Ordering in the System Chloroform−Syndiotactic Polystyrene. *Macromolecules* **2002**, *35*, 2296–2304, doi:10.1021/ma011684d.
111. Venditto, V.; De Girolamo Del Mauro, A.; Mensitieri, G.; Milano, G.; Musto, P.; Rizzo, P.; Guerra, G. Anisotropic Guest Diffusion in the δ Crystalline Host Phase of Syndiotactic Polystyrene: Transport Kinetics in Films with Three Different Uniplanar Orientations of the Host Phase. *Chem. Mater.* **2006**, *18*, 2205–2210, doi:10.1021/cm051657s.
112. Malik, S.; Roizard, D.; Guenet, J.-M. Multiporous Material from Fibrillar Syndiotactic Polystyrene Intercalates. *Macromolecules* **2006**, *39*, 5957–5959, doi:10.1021/ma060770g.
113. Pajonk, G.M. Catalytic Aerogels. *Catal. Today* **1997**, *35*, 319–337, doi:10.1016/S0920-5861(96)00163-0.
114. Daniel, C.; Avallone, A.; Rizzo, P.; Guerra, G. Control of Crystal Size and Orientation in Polymer Films by Host−Guest Interactions. *Macromolecules* **2006**, *39*, 4820–4823, doi:10.1021/ma0604486.
115. Daniel, C.; Menelle, A.; Brulet, A.; Guenet, J.-M. Thermoreversible Gelation of Syndiotactic Polystyrene in Toluene and Chloroform. *Polymer* **1997**, *38*, 4193–4199, doi:10.1016/S0032-3861(96)01005-1.
116. Chatani, Y.; Shimane, Y.; Inagaki, T.; Ijitsu, T.; Yukinari, T.; Shikuma, H. Structural Study on Syndiotactic Polystyrene: 2. Crystal Structure of Molecular Compound with Toluene. *Polymer* **1993**, *34*, 1620–1624, doi:10.1016/0032-3861(93)90318-5.
117. Daniel, C.; Alfano, D.; Venditto, V.; Cardea, S.; Reverchon, E.; Larobina, D.; Mensitieri, G.; Guerra, G. Aerogels with a Microporous Crystalline Host Phase. *Adv. Mater.* **2005**, *17*, 1515–

1518, doi:https://doi.org/10.1002/adma.200401762.
118. Daniel, C.; Giudice, S.; Guerra, G. Syndiotatic Polystyrene Aerogels with β, γ, and ε Crystalline Phases. *Chem. Mater.* **2009**, *21*, 1028–1034, doi:10.1021/cm802537g.
119. Daniel, C.; Navarra, W.; Venditto, V.; Sacco, O.; Vaiano, V. 4 - Nanoporous polymeric aerogels–based structured photocatalysts for the removal of organic pollutant from water under visible or solar light. In *Visible Light Active Structured Photocatalysts for the Removal of Emerging Contaminants*; Sacco, O., Vaiano, V., Eds.; Elsevier, 2020; pp. 99–120 ISBN 978-0-12-818334-2.
120. Nakaoki, T.; Goto, N.; Saito, K. Selective Sorption and Desorption of Organic Solvent for δ-Syndiotactic Polystyrene. *Polym. J.* **2009**, *41*, 214–218, doi:10.1295/polymj.PJ2008208.
121. Libralato, G., 2013. Management and Control of Wastewater: An Ecotoxicological Approach. Handbook of Wastewater Treatment: Biological Methods, Technology and Environmental Impac - Cerca Con Google Available online: https://www.google.com/search?q=Libralato%2C+G.%2C+2013.+Management+and+control+of+wastewater%3A+an+ecotoxicological+approach.+Handbook+of+Wastewater+Treatment%3A+Biological+Methods%2C+Technology+and+Environmental+Impac&rlz=1C1CHBF_itIT926IT926&oq=Libralato%2C+G.%2C+2013.+Management+and+control+of+wastewater%3A+an+ecotoxicological+approach.+Handbook+of+Wastewater+Treatment%3A+Biological+Methods%2C+Technology+and+Environmental+Impac&aqs=chrome..69i57.488j0j7&sourceid=chrome&ie=UTF-8 (accessed on 17 March 2021).
122. Fernández-Alba, A.R.; Hernando, D.; Agüera, A.; Cáceres, J.; Malato, S. Toxicity Assays: A Way for Evaluating AOPs Efficiency. *Water Res.* **2002**, *36*, 4255–4262, doi:10.1016/S0043-1354(02)00165-3.
123. Pedrazzani, R.; Bertanza, G.; Brnardić, I.; Cetecioglu, Z.; Dries, J.; Dvarionienė, J.; García-Fernández, A.J.; Langenhoff, A.; Libralato, G.; Lofrano, G.; et al. Opinion Paper about Organic Trace Pollutants in Wastewater: Toxicity Assessment in a European Perspective. *Sci. Total Environ.* **2019**, *651*, 3202–3221, doi:10.1016/j.scitotenv.2018.10.027.
124. Libralato, G.; Lofrano, G.; Siciliano, A.; Gambino, E.; Boccia, G.; Federica, C.; Francesco, A.; Galdiero, E.; Gesuele, R.; Guida, M. 8 - Toxicity assessment of wastewater after advanced oxidation processes for emerging contaminants' degradation∗. In *Visible Light Active Structured Photocatalysts for the Removal of Emerging Contaminants*; Sacco, O., Vaiano, V., Eds.; Elsevier, 2020; pp. 195–211 ISBN 978-0-12-818334-2.

125. Rizzo, L. Bioassays as a Tool for Evaluating Advanced Oxidation Processes in Water and Wastewater Treatment. *Water Res.* **2011**, *45*, 4311–4340, doi:10.1016/j.watres.2011.05.035.
126. EUR-Lex - 32008L0105 - EN - EUR-Lex Available online: https://eur-lex.europa.eu/eli/dir/2008/105/oj (accessed on 17 March 2021).
127. Sass, J.B.; Colangelo, A. European Union Bans Atrazine, While the United States Negotiates Continued Use. *Int. J. Occup. Environ. Health* **2006**, *12*, 260–267, doi:10.1179/oeh.2006.12.3.260.
128. Solomon, R.D.J.; Kumar, A.; Satheeja Santhi, V. Atrazine Biodegradation Efficiency, Metabolite Detection, and TrzD Gene Expression by Enrichment Bacterial Cultures from Agricultural Soil. *J. Zhejiang Univ. Sci. B* **2013**, *14*, 1162–1172, doi:10.1631/jzus.B1300001.
129. Székács, A.; Mörtl, M.; Darvas, B. Monitoring Pesticide Residues in Surface and Ground Water in Hungary: Surveys in 1990–2015. *J. Chem.* **2015**, *2015*, 717948, doi:10.1155/2015/717948.
130. López-Muñoz, M.J.; Aguado, J.; Revilla, A. Photocatalytic Removal of S-Triazines: Evaluation of Operational Parameters. *Catal. Today* **2011**, *161*, 153–162, doi:10.1016/j.cattod.2010.10.076.
131. Products Available online: https://www.cropscience.bayer.com/who-we-are/about-us/products (accessed on 17 March 2021).
132. Elbert, A.; Haas, M.; Springer, B.; Thielert, W.; Nauen, R. Applied Aspects of Neonicotinoid Uses in Crop Protection. *Pest Manag. Sci.* **2008**, *64*, 1099–1105, doi:10.1002/ps.1616.
133. Velisek, J.; Stara, A. Effect of Thiacloprid on Early Life Stages of Common Carp (Cyprinus Carpio). *Chemosphere* **2018**, *194*, 481–487, doi:10.1016/j.chemosphere.2017.11.176.
134. Chemisch-Biologisches Monitoring Zu Pflanzenschutzmittelbelastungen Und Lebensgemeinschaften in Gräben Des Alten Landes*) - PDF Free Download Available online: https://docplayer.org/8944598-Chemisch-biologisches-monitoring-zu-pflanzenschutzmittelbelastungen-und-lebensgemeinschaften-in-graeben-des-alten-landes.html (accessed on 17 March 2021).
135. Sánchez-Bayo, F.; Hyne, R.V. Detection and Analysis of Neonicotinoids in River Waters--Development of a Passive Sampler for Three Commonly Used Insecticides. *Chemosphere* **2014**, *99*, 143–151, doi:10.1016/j.chemosphere.2013.10.051.
136. Schmuck, R. Ecotoxicological Profile of the Insecticide Thiacloprid. *PFLANZENSCHUTZ NACHRICHTEN -BAYER-*

Engl. Ed. **2001**, *54*, 161–184.
137. Zhao, Y.-J.; Dai, Y.-J.; Yu, C.-G.; Luo, J.; Xu, W.-P.; Ni, J.-P.; Yuan, S. Hydroxylation of Thiacloprid by Bacterium Stenotrophomonas Maltophilia CGMCC1.1788. *Biodegradation* **2009**, *20*, 761–768, doi:10.1007/s10532-009-9264-0.
138. Zhang, H.-J.; Zhou, Q.-W.; Zhou, G.-C.; Cao, Y.-M.; Dai, Y.-J.; Ji, W.-W.; Shang, G.-D.; Yuan, S. Biotransformation of the Neonicotinoid Insecticide Thiacloprid by the Bacterium Variovorax Boronicumulans Strain J1 and Mediation of the Major Metabolic Pathway by Nitrile Hydratase. *J. Agric. Food Chem.* **2012**, *60*, 153–159, doi:10.1021/jf203232u.
139. Hussain, S.; Hartley, C.J.; Shettigar, M.; Pandey, G. Bacterial Biodegradation of Neonicotinoid Pesticides in Soil and Water Systems. *FEMS Microbiol. Lett.* **2016**, *363*, doi:10.1093/femsle/fnw252.
140. Leung, S.W.; Watts, R.J.; Miller, G.C. Degradation of Perchloroethylene by Fenton's Reagent: Speciation and Pathway. *J. Environ. Qual.* **1992**, *21*, 377–381, doi:https://doi.org/10.2134/jeq1992.00472425002100030012x.
141. Sacco, O.; Stoller, M.; Vaiano, V.; Ciambelli, P.; Chianese, A.; Sannino, D. Photocatalytic Degradation of Organic Dyes under Visible Light on N-Doped Photocatalysts. *Int. J. Photoenergy* **2012**, *2012*, e626759, doi:10.1155/2012/626759.
142. Wu, L.; Xing, J.; Hou, Y.; Xiao, F.Y.; Li, Z.; Yang, H.G. Fabrication of Regular ZnO/TiO2 Heterojunctions with Enhanced Photocatalytic Properties. *Chem. – Eur. J.* **2013**, *19*, 8393–8396, doi:10.1002/chem.201300849.
143. Yan, J.-M.; Zhang, X.-B.; Han, S.; Shioyama, H.; Xu, Q. Iron-Nanoparticle-Catalyzed Hydrolytic Dehydrogenation of Ammonia Borane for Chemical Hydrogen Storage. *Angew. Chem.* **2008**, *120*, 2319–2321, doi:https://doi.org/10.1002/ange.200704943.
144. Bernard, P.; Stelmachowski, P.; Broś, P.; Makowski, W.; Kotarba, A. Demonstration of the Influence of Specific Surface Area on Reaction Rate in Heterogeneous Catalysis. *J. Chem. Educ.* **2021**, *98*, 935–940, doi:10.1021/acs.jchemed.0c01101.
145. Pozan, G.S.; Kambur, A. Significant Enhancement of Photocatalytic Activity over Bifunctional ZnO–TiO2 Catalysts for 4-Chlorophenol Degradation. *Chemosphere* **2014**, *105*, 152–159, doi:10.1016/j.chemosphere.2014.01.022.
146. Li, T.; Zhou, C.; Jiang, M. UV Absorption Spectra of Polystyrene. *Polym. Bull.* **1991**, *25*, 211–216, doi:10.1007/BF00310794.
147. Vinodh, R.; Abidov, A.; Peng, M.M.; Babu, C.M.; Palanichamy, M.; Cha, W.S.; Jang, H.-T. A New Strategy to Synthesize Hypercross-Linked Conjugated Polystyrene and Its Application

towards CO2 Sorption. *Fibers Polym.* **2015**, *16*, 1458–1467, doi:10.1007/s12221-015-5151-y.
148. Vindimian, REGTOX-EV6.Xls. Regtox 6.3 Software Program.Xls,.
149. Lee, K.M.; Lai, C.W.; Ngai, K.S.; Juan, J.C. Recent Developments of Zinc Oxide Based Photocatalyst in Water Treatment Technology: A Review. *Water Res.* **2016**, *88*, 428–448, doi:10.1016/j.watres.2015.09.045.
150. Mehrotra, N.; Tripathi, R.M.; Zafar, F.; Singh, M.P. Catalytic Degradation of Dichlorvos Using Biosynthesized Zero Valent Iron Nanoparticles. *IEEE Trans. NanoBioscience* **2017**, *16*, 280–286, doi:10.1109/TNB.2017.2700232.
151. Sacco, O.; Vaiano, V.; Sannino, D.; Picca, R.A.; Cioffi, N. Ag Modified ZnS for Photocatalytic Water Pollutants Degradation: Influence of Metal Loading and Preparation Method. *J. Colloid Interface Sci.* **2019**, *537*, 671–681, doi:10.1016/j.jcis.2018.11.073.
152. De Rosa, C.; Guerra, G.; Petraccone, V.; Pirozzi, B. Crystal Structure of the Emptied Clathrate Form (Δe Form) of Syndiotactic Polystyrene. *Macromolecules* **1997**, *30*, 4147–4152, doi:10.1021/ma970061q.
153. Milano, G.; Venditto, V.; Guerra, G.; Cavallo, L.; Ciambelli, P.; Sannino, D. Shape and Volume of Cavities in Thermoplastic Molecular Sieves Based on Syndiotactic Polystyrene. *Chem. Mater.* **2001**, *13*, 1506–1511, doi:10.1021/cm001089a.
154. Daniel, C.; Longo, S.; Ricciardi, R.; Reverchon, E.; Guerra, G. Monolithic Nanoporous Crystalline Aerogels. *Macromol. Rapid Commun.* **2013**, *34*, 1194–1207, doi:10.1002/marc.201300260.
155. Effect of Solar Simulated N-Doped TiO2 Photocatalysis on the Inactivation and Antibiotic Resistance of an E. Coli Strain in Biologically Treated Urban Wastewater - ScienceDirect Available online: https://www.sciencedirect.com/science/article/pii/S0926337313004529 (accessed on 16 April 2021).
156. Wahab, H.S.; Hussain, A.A. Photocatalytic Oxidation of Phenol Red onto Nanocrystalline TiO2 Particles. *J. Nanostructure Chem.* **2016**, *6*, 261–274, doi:10.1007/s40097-016-0199-9.
157. Dangwang Dikdim, J.M.; Gong, Y.; Noumi, G.B.; Sieliechi, J.M.; Zhao, X.; Ma, N.; Yang, M.; Tchatchueng, J.B. Peroxymonosulfate Improved Photocatalytic Degradation of Atrazine by Activated Carbon/Graphitic Carbon Nitride Composite under Visible Light Irradiation. *Chemosphere* **2019**, *217*, 833–842, doi:10.1016/j.chemosphere.2018.10.177.
158. Adishkumar, S.; Kanmani, S.; Banu, J.R. Solar Photocatalytic Treatment of Phenolic Wastewaters: Influence of Chlorides,

Sulphates, Aeration, Liquid Volume and Solar Light Intensity. *Desalination Water Treat.* **2014**, *52*, 7957–7963, doi:10.1080/19443994.2013.834522.
159. Feng, Z.; YuanFu, L.; LuLu, H.; YanPing, G.; Hui, Z.; DongQiang, Z.; HuiHua, T. Individual and Combined Toxicity of Atrazine, Butachlor, Halosulfuron-Methyl and Mesotrione on the Microalga Selenastrum Capricornutum. *Ecotoxicol. Environ. Saf.* **2018**, *148*, 969–975.
160. Bijlsma, L.; Pitarch, E.; Hernández, F.; Fonseca, E.; Marín, J.M.; Ibáñez, M.; Portolés, T.; Rico, A. Ecological Risk Assessment of Pesticides in the Mijares River (Eastern Spain) Impacted by Citrus Production Using Wide-Scope Screening and Target Quantitative Analysis. *J. Hazard. Mater.* **2021**, *412*, 125277, doi:10.1016/j.jhazmat.2021.125277.
161. Palma, P.; Palma, V.L.; Fernandes, R.M.; Soares, A.M.V.M.; Barbosa, I.R. Acute Toxicity of Atrazine, Endosulfan Sulphate and Chlorpyrifos to Vibrio Fischeri, Thamnocephalus Platyurus and Daphnia Magna, Relative to Their Concentrations in Surface Waters from the Alentejo Region of Portugal. *Bull. Environ. Contam. Toxicol.* **2008**, *81*, 485–489, doi:10.1007/s00128-008-9517-3.
162. Tchounwou, P.B.; Wilson, B.; Ishaque, A.; Ransome, R.; Huang, M.-J.; Leszczynski, J. Toxicity Assessment of Atrazine and Related Triazine Compounds in the Microtox Assay, and Computational Modeling for Their Structure-Activity Relationship. *Int. J. Mol. Sci.* **2000**, *1*, 63–74, doi:10.3390/ijms1040063.
163. Moreira, R.A.; Mansano, A. da S.; Silva, L.C. da; Rocha, O. A Comparative Study of the Acute Toxicity of the Herbicide Atrazine to Cladocerans Daphnia Magna, Ceriodaphnia Silvestrii and Macrothrix Flabelligera. *Acta Limnol. Bras.* **2014**.
164. Franklin, N.M.; Rogers, N.J.; Apte, S.C.; Batley, G.E.; Gadd, G.E.; Casey, P.S. Comparative Toxicity of Nanoparticulate ZnO, Bulk ZnO, and ZnCl2 to a Freshwater Microalga (Pseudokirchneriella Subcapitata): The Importance of Particle Solubility. *Environ. Sci. Technol.* **2007**, *41*, 8484–8490, doi:10.1021/es071445r.
165. Johnson, T.L.; Scherer, M.M.; Tratnyek, P.G. Kinetics of Halogenated Organic Compound Degradation by Iron Metal. *Environ. Sci. Technol.* **1996**, *30*, 2634–2640, doi:10.1021/es9600901.

Annex A

Table 17. List of organic priority substances in the field of water policy and certain other pollutants defined in the Directive 2013/39/EU.

Class	Compounds	AA-EQS (µg/L)	MAC-EQS (µg/L)	EQS biota (µg/kg ww)
Organochlorine pesticides	Cyclodiene pesticides[a] including aldrin, dieldrin, endrin and isodrin	∑: 0.005 –0.01	n.a.	–
	Endosulfan	0.000 5– 0.005	0.004–0.01	–
	Dicofol	3.2×10^{-5}– 1.3×10^{-3}	n.a.	33
	Heptachlor and heptachlor epoxide	1×10^{-8}– 2×10^{-7}	3×10^{-5}– 3×10^{-4}	6.7×10^{-3}
	Pentachlorophenol	0.4	1.0	–
	Hexachlorocyclohexane (HCH): e.g. γ-HCH or lindane	0.002 –0.02	0.02–0.04	–
	Hexachlorobenz	–	0.05	10

	ene			
	Hexachlorobutadiene	–	0.6	55
	Dichlorodiphenyltrichloroethane (DDT) total[a] and p,p′-DDT[a]	0.025 (DDT total) 0.01 (p,p′-DDT)	n.a.	–
Organophosphorus pesticides	Chlorfenvinphos	0.1	0.3	–
	Chlorpyrifos (Chlorpyrifos-ethyl)	0.03	0.1	–
	Dichlorvos	6×10^{-5}–6×10^{-4}	7×10^{-5}–7×10^{-4}	–
Triazine pesticides	Atrazine	0.6	2.0	–
	Cybutryne	0.0025	0.016	–
	Simazine	1.0	4.0	–
	Terbutryn	0.0065–0.065	0.034–0.34	–
Phenylurea pesticides	Diuron	0.2	1.8	–
	Isoproturon	0.3	1.0	–

Chloroacetanilide pesticide	Alachlor	0.3	0.7	–
Dinitroaniline pesticide	Trifluralin	0.03	n.a.	–
Pyrethroid pesticide	Cypermethrin	8×10^{-6}–8×10^{-5}	6×10^{-5}–6×10^{-4}	–
Diphenyl ethers pesticides	Aclonifen	0.012–0.12	0.012–0.12	–
	Bifenox	0.0012–0.012	0.004–0.04	–
Quinoline pesticide	Quinoxyfen	0.015–0.15	0.54–2.7	–
Organotin	Tributyltin compounds including tributyltin-cation	0.0002	0.0015	–
Brominated diphenylethers		–	0.014–0.14	0.0085
Hexabromocyclododecanes		0.0008–0.0016	0.05–0.5	167
Polyaromatic hydrocarbons	Benzo(a)pyrene	1.7×10^{-4}	0.027–0.27	5

(PAHs)[b]	Benzo(b)fluoranthene	Benzo(a)pyrene is considered as a marker for the other PAHs.	0.017	Benzo(a)pyrene is considered as a marker for the other PAHs.
	Benzo(k)fluoranthene		0.017	
	Benzo(g,h,i)-perylene		8.2×10^{-4}–8.2×10^{-3}	
	Indeno(1,2,3-cd)-pyrene		n.a.	
PAHs listed separately	Anthracene	0.1	0.1	–
	Fluoranthene	0.0063	0.12	30
	Naphthalene	2.0	130	–
Dioxins and dioxin-like compounds[b]	Polychlorinated dibenzo-p-dioxins (PCDDs)	–	n.a.	Toxic equivalents (PCDDs + PCDFs + PCB-DL): 0.0065
	Polychlorinated dibenzofurans (PCDFs)			
	Dioxin-like polychlorinated biphenyls (PCB-DL)			
Solvents	Benzene	8–10	50	–
	Trichlorobenzenes	0.4	n.a.	–

	Pentachlorobenzene	0.0007–0.007	n.a.	–
	Chloroalkanes, C10–13	0.4	1.4	–
	1,2-Dichloroethane	10	n.a.	–
	Dichloromethane	20	n.a.	–
	Trichloromethane	2.5	n.a.	–
	Carbon tetrachloride[a]	12	n.a.	–
	Tetrachloro-ethylene[a]	10	n.a.	–
	Trichloro-ethylene[a]	10	n.a.	–
Industrial compounds	Di(2-ethylhexyl)phthalate (DEHP)	1.3	n.a.	–
	Perfluorooctane sulfonic acid and its derivatives (PFOS)	1.3×10^{-4}–6.5×10^{-4}	7.2–36	9.1
	Nonylphenol including isomer	0.3	2.0	–

	4-nonylphenol			
	Octylphenol including isomer 4-(1,1′,3,3′-tetramethylbutyl)-phenol	0.01–0.1	n.a.	–